

DISSERTATION

Structural Studies by Solid State NMR on the Function of Nanoscale Materials:

Heterogeneous Re Catalysts for Olefin Metathesis and Semiconducting InGaP Nanoparticles

ausgeführt zum Zwecke der Erlangung des akademischen Grades
eines Doktors der Naturwissenschaften unter der Leitung von

o. Univ.-Prof. Dr. Ulrich Schubert

Prof. Dr. Nicola Hüsing

E 165, Institut für Materialchemie

und

Prof. Dr. Bradley Chmelka

University of California Santa Barbara

eingereicht an der Technischen Universität Wien

Fakultät für Technische Chemie

von

Christina Raab

9726099

Brigittenauerlande 22/14, 1200 Wien

Wien, am 22. Mai 2007

.....

**Diese Arbeit ist meinen Eltern,
Monika und Walter Raab,
in Liebe gewidmet.**

**“The only limit to our realization of tomorrow
will be our doubts of today.”**

F. D. Roosevelt

Acknowledgments

Mein aufrichtiger Dank geht an *Prof. Ulrich Schubert* und *Prof. Nicola Hüsing* für ihre Unterstützung und ihr Vertrauen während meiner gesamten Studienzeit. Ich bedanke mich für die Freiheit und Möglichkeit, die Forschungsarbeiten für die vorliegende Dissertation an der University of California in Santa Barbara durchzuführen.

I express my sincere thanks to *Prof. Brad Chmelka* for giving me the opportunity to join his research group, to work on fascinating and diverse projects and for his financial support throughout my time at UCSB.

I thank *Prof. Susannah Scott* for welcoming me on the metathesis project and for the experience of working in her group.

The following work would not exist as such without *Prof. Jürgen Eckert*. I give my heartfelt gratitude to him for his professional advice and encouraging support.

Many thanks for valuable collaborations and a great working environment to my colleagues in Santa Barbara: *George Athens, Pio Bättig, Mia Berrettini, Gary Braun, Swarup Chattopadhyay, Jan Epping, Heather Leifeste, Tony Moses, Jordi Nolla, Naseem Ramsahye* and *Almut Rapp*.

Special thanks to *Dr. Jerry Hu* for his help in NMR matters.

Albert Schweitzer once said: "In everyone's life, at some time, our inner fire goes out. It is then burst into flames by an encounter with another human being. We should all be thankful for those people who rekindle the inner spirit." I would like to dedicate this quote to the following people: *Paul Brombal, Lisa Dubrow, Jürgen Eckert, Elisabeth Ehart, Zafiris Gourgouliatos, Peter Matthies, Mai Nazif, Alex Rondon, Tina Salguero, Jeanine van Seenus* and *Debbie Watts*. I am deeply grateful to them for their friendship, life-changing interactions and empowering inspiration during and beyond my time in California.

Ich danke *Tina Arl, Sara Najafi, Doris Rechberger, Stefan Schmiedler, Ruth Schneider* und *Mahtab Sotoudeh* für Jahre der Freundschaft.

Mein tiefster Dank gilt meinen Eltern für ihre bedingungslose Unterstützung in jeder Hinsicht und das wunderbare Geschenk dieses Lebens.

Abstract

With the rapid rise in the importance of nanoscale materials, many standard structural characterization methods based on ordered structures have become much less useful, and need to be supplemented by innovative application of techniques such as NMR. In this work two examples in nanomaterials and interfacial chemistry are described where critical atomic level structural details, as well as information on dynamics, were obtained by the use of solid state NMR spectroscopy in conjunction with computational and related experimental approaches.

The first instance addresses the question of the activation of a grafted organometallic rhenium complex by virtue of its interaction with a particular support, namely amorphous silica-alumina. The objectives of this research are to establish the molecular origin of the catalytic activity of this supported Re complex including the structures of adsorption and reaction sites and their relationship to its activity for olefin metathesis. The chemisorption of CH_3ReO_3 on the surface of a dehydrated, amorphous silica-alumina generates a highly active catalyst for the metathesis of olefins, including functionalized olefins. Synthesis of this catalytic system is accomplished by chemical vapor deposition onto the support. The principal characterization methods were 1D and 2D solid state NMR (^1H , ^{13}C , ^{27}Al), EXAFS, IR, and computational modeling. This catalyst was found to contain two families of chemically and spectroscopically distinct sites, which react differently with olefinic reagents, depending on the grafting conditions, support modification, and/or Re loading. The active grafting site is one with a two-point interaction of the Re complex with the support, wherein one oxo ligand interacts with an Lewis acidic Al site and a support oxygen is

weakly coordinated to the Re center. A second, highly mobile CH_3ReO_3 species is primarily found at higher catalyst loadings, and was determined to be bound by hydrogen-bonding to surface silanols. Its presence furthermore decreases the catalytic activity in propylene self-metathesis reactions. This work demonstrates that the olefin metathesis activity is correlated with the presence of Lewis acid activated CH_3ReO_3 , so that a material with high (10 wt.%) Re loading with a large number of H-bonded sites is no more active than that with low (1 wt.%) Re loading and only Lewis acidic site bonded CH_3ReO_3 .

In the second part of this work the effect of rather different interfacial interactions are examined, namely those of structural changes following surface treatments on the optical properties of nanoscale Group III-V semiconductors and their ternary analogs. Recent advances in chemical synthesis protocols have made certain coated $\text{In}_{0.91}\text{Ga}_{0.09}\text{P}$ nanoparticles attractive, less-toxic alternatives to Cd-, Se-, and Te-based Group II-VI compounds for electrical, opto-electronic, or biological device applications. 1D and 2D MAS NMR experiments (^{31}P , ^{71}Ga , ^{115}In) were used to establish surface reconstruction and changes in local environments of sites linked to increased photoluminescence upon etching of 4.5 nm InGaP quantum dots. These experiments provide a picture of the atomic and molecular distribution on the surface and the interior of the nanoparticle, and show that etching with HF results in significant reorganization of the InGaP nanoparticle surfaces and removal of surface defects. This leads to the ^{71}Ga species being located in chemically and electronically more ordered molecular environments near the periphery of the nanoparticle, and hence improved photoluminescence.

Kurzfassung

Mit zunehmender Bedeutung von nanoskaligen Materialien erweisen sich viele Standard-Charakterisierungsmethoden, die auf geordneten Strukturen basieren, als weniger geeignet und müssen durch zusätzliche, innovative Techniken, wie NMR ergänzt werden. In der vorliegenden Arbeit werden zwei Beispiele aus den Bereichen Nanomaterialien und Grenzflächenchemie beschrieben. Mittels Anwendung von Festkörper-NMR-Spektroskopie in Kombination mit theoretischen Berechnungen und zusätzlichen experimentellen Methoden konnten Einblicke in atomare Strukturdetails und Systemdynamiken erlangt werden.

Im ersten System gilt es, der Frage der Aktivierung eines metallorganischen Rheniumkomplexes durch Wechselwirkung mit einem amorphen Siliziumoxid-Aluminiumoxid-Träger nachzugehen. Das Ziel ist, die molekulare Herkunft der Katalysatoraktivität des aufgebrachtten Re-Komplexes zu erforschen, sowie die Strukturen der Adsorptions- und Reaktionsstellen in Zusammenhang mit der Aktivität in Olefinmetathese-Reaktionen aufzuklären. Die Chemisorption von CH_3ReO_3 auf der Oberfläche von dehydrierten, amorphen Siliziumoxid-Aluminiumoxid resultiert in einem sehr aktiven Katalysator für die Metathese von Olefinen, einschließlich funktionalisierter Olefine. Das Katalysatorsystem wurde durch Aufdampfen (CVD) hergestellt und als Charakterisierungsmethoden 1D und 2D Festkörper-NMR (^1H , ^{13}C , ^{27}Al) kombiniert mit EXAFS, IR und theoretische Modellierungen herangezogen. Es konnte gezeigt werden, dass der Katalysator je nach Trägermodifizierung und Re-Ladung zwei Arten von chemisch und spektroskopisch verschiedenen Stellen aufweist, welche mit dem Olefin-Reagens unterschiedlich reagieren. An der aktiven Stelle findet eine

Zweipunkt-Wechselwirkung des Re-Komplexes mit dem Träger statt, in welcher ein Oxo-Ligand mit einer Lewis-sauren Al Stelle wechselwirkt und ein Trägersauerstoff schwach mit dem Re-Zentrum koordiniert ist. Eine zweite, hoch mobile CH_3ReO_3 -Spezies findet sich hauptsächlich bei höheren Katalysatorladungen und resultiert aus Wasserstoffbindungen zu Siliziumhydroxid-Gruppen an der Trägeroberfläche. Ihre Anwesenheit verringert die Katalysatoraktivität für Propylen-Selbstmetathese-Reaktionen. In dieser Arbeit wird gezeigt, dass die Olefinmetathese-Aktivität mit Lewis-sauren aktivierten CH_3ReO_3 korreliert ist, sodass ein Material mit hoher Re-Beladung (10 wt.%) und einer großen Anzahl von H-gebundenen Stellen nicht aktiver ist als ein Katalysatorsystem mit geringerer (1 wt.%) Re-Beladung, in welchem CH_3ReO_3 ausschließlich an Lewis-saure Stellen gebunden ist.

Im zweiten Teil der Dissertation werden strukturelle Veränderungen in Folge von Oberflächenbehandlungen für optische Eigenschaften in nanoskaligen Halbleitern der Gruppe III-V und ihre ternären Zusammensetzungen untersucht. In letzter Zeit haben Fortschritte in der Entwicklung von chemischen Syntheseprotokollen ligandenstabilisierte InGaP-Nanopartikel zu einer attraktiven, weniger toxischen Alternative zu Cd-, Se-, und Te- basierenden Gruppe II-VI-Materialien für elektrische, opto-elektronische und biologische Anwendungen gemacht. 1D und 2D MAS NMR Experimente (^{31}P , ^{71}Ga , ^{115}In) wurden durchgeführt um Oberflächen-Rekonstruktionen und Änderungen in der lokalen Umgebung von P, In und Ga Stellen zu beschreiben, welche durch einen Ätzvorgang der 4.5 nm großen $\text{In}_{0.91}\text{Ga}_{0.09}\text{P}$ -Nanopartikel hervorgerufen werden. Diese Experimente liefern Einblicke in die atomare und molekulare Verteilung auf der Oberfläche und im Inneren der Nanopartikel, und zeigen, dass Ätzen mit HF mit signifikanter Reorganisation der InGaP-Nanopartikel-

Oberfläche und dem Entfernen von Oberflächendefekten einher geht. Dies führt dazu, dass ^{71}Ga Spezies sich in chemisch und elektronisch geordneteren Umgebungen nahe der Peripherie des Nanopartikels befinden, und zu einer daraus resultierenden erhöhten Photolumineszenz.

Table of contents

Chapter 1. Introduction 1

1.1	Olefin metathesis	3
1.2	Olefin metathesis catalysts and supports	7
1.2.1	Homogeneous catalysts	7
1.2.2	Heterogeneous catalysts	9
1.2.3	Metal oxide supports: Silica-alumina.....	10
1.3	Heterogeneous rhenium catalysts for olefin metathesis: methyltrioxorhenium CH_3ReO_3	11
1.4	Heterogeneous catalysis and nanoscience.....	14
1.5	Description of nanocrystals and surface reconstruction	15
1.6	Semiconducting quantum dot systems (CdSe, InP, InGaP).....	18

Chapter 2. Characterization Techniques and Experimental Details 21

2.1	Solid state Nuclear Magnetic Resonance (NMR) spectroscopy	23
2.1.1	Basics of NMR spectroscopy	23
2.1.2	Nuclear spin interactions and averaging techniques	26
2.1.3	Description of NMR pulse sequences employed in this work	31
2.2	Basics of Density Functional Theory (DFT).....	36
2.3	Basics of X-Ray Absorption Spectroscopy (XAFS)	39
2.4	Experimental details.....	43
2.4.1	Catalyst materials, synthesis procedures and instrument settings.....	43
2.4.2	Nanoparticle synthesis procedures and instrument settings	53

Chapter 3. Results and Discussion.	
Heterogeneous Re Catalysts for Olefin Metathesis	57
3.1 NMR and EXAFS investigations on molecular CH_3ReO_3	59
3.2 Grafted CH_3ReO_3 on silica-alumina: low loadings.....	62
3.3 Deposition of higher loadings of CH_3ReO_3 on silica-alumina..	77
3.4 Deposition of CH_3ReO_3 on silica	91
3.5 Activity and selectivity in olefin metathesis	94
3.6 Effect of different oxide supports on the binding and catalytic activity CH_3ReO_3	97
Chapter 4. Results and Discussion.	
Semiconducting InGaP Nanoparticles	107
4.1 Surface passivation and physical properties (^{13}C MAS NMR, TEM, photoluminescence)	109
4.2 Total phosphorous site identification (^{31}P MAS NMR)	112
4.3 Surface phosphorous oxidation sites identification	115
4.4 Indium site occupation (^{115}In spin-echo MAS NMR)	125
4.5 Gallium siting and ordering (^{71}Ga spin-echo MAS NMR)	127
Chapter 5. Summary and Outlook	133
5.1 Heterogeneous Re catalyst for olefin metathesis.....	135
5.2 Semiconducting InGaP nanoparticles	141
Chapter 6. References	145
Appendix: Curriculum Vitæ	157

Abbreviations frequently used in this thesis

BABA	BAck-to-BAck pulse sequence
CP	Cross Polarization
1D, 2D	one-dimensional, two-dimensional
DFT	Density Functional Theory
DQC	Double Quantum Coherence
DQ NMR	Double Quantum NMR
EXAFS	Extended X-Ray Absorption Fine Structure
FSLG	Frequency-Switched Lee-Goldberg
fwhm	full width at half-maximum
HDA	hexadecylamine
HETCOR	HETeronuclear CORrelation
HF	hydrogen fluoride
HMDS	hexamethyldisilazane
InGaP	Indium Gallium Phosphide
InP	Indium Phosphide
IR	Infrared Spectroscopy
MAS	Magic Angle Spinning
NEXAFS	Near Edge X-ray Absorption Fine Structure
NMR	Nuclear Magnetic Resonance Spectroscopy
PL	photoluminescence
RF	radio frequency
RT	room temperature
TEM	Transmission Electron Microscopy
wt.%	weight percent
XAFS	X-ray Absorption Fine Structure
XAS	X-ray Absorption Spectroscopy
XANES	X-ray Absorption Near Edge Structure
XPS	X-ray Photoelectron Spectroscopy

List of Figures

1-1. Homogeneous olefin metathesis catalysts	8
1-2. The structure of methyltrioxorhenium.....	12
1-3. Domains of a nanocrystal	16
2-1. Basic arrangement of an NMR spectrometer.....	26
2-2. Magic angle.....	27
2-3. General pulse scheme for a single-pulse NMR experiment	31
2-4. Pulse sequence for a CPMAS experiment.....	32
2-5. Pulse sequence for a 2D HETCOR experiment	34
2-6. Spin-echo NMR pulse sequence	34
2-7. 2D DQ MAS NMR scheme with BABA pulse sequence	35
2-8. Representative generic XAS spectrum with the different energy regions	41
2-9. Interference of the photoelectron wave created by the absorption process being backscattered by the neighboring atoms	43
3-1. NMR spectra of CH_3ReO_3 : (a) ^1H MAS NMR spectrum for polycrystalline CH_3ReO_3 and ^1H NMR spectrum of CH_3ReO_3 in CDCl_3 , (b) ^{13}C CPMAS spectrum for polycrystalline CH_3ReO_3 and ^{13}C NMR spectrum of CH_3ReO_3 in CDCl_3	60
3-2. EXAFS data in (a) k^3 -weighted k -space, (b) non-phase-corrected R -space for polycrystalline CH_3ReO_3	61
3-3. Comparison of FTIR spectra obtained for polycrystalline CH_3ReO_3 and CH_3ReO_3 grafted on silica-alumina, in the $\nu(\text{CH}_3)$ region	63
3-4. (a) ^{13}C CPMAS spectrum for silica-alumina modified with $^{13}\text{CH}_3\text{ReO}_3$, (b) single-pulse ^1H MAS NMR spectra of dehydrated silica-alumina before and after modification with $^{13}\text{CH}_3\text{ReO}_3$	64
3-5. 2D $^{13}\text{C}\{^1\text{H}\}$ HETCOR MAS NMR spectrum for silica-alumina modified with $^{13}\text{CH}_3\text{ReO}_3$ (0.4 wt.% Re).....	65
3-6. Single-pulse ^1H MAS spectra for the same quantity of the dehydrated silica-alumina support before and after grafting CH_3ReO_3 (2.3 wt.% Re)	66
3-7. ^{27}Al MAS NMR spectra for hydrated silica-alumina and dehydrated silica- alumina, recorded in the presence of bulk aluminum nitride as an internal standard.....	67
3-8. EXAFS data in (a) k^3 -weighted k -space, (b) non-phase-corrected R -space for CH_3ReO_3 adsorbed on dehydrated silica-alumina (1.3 wt.% Re)	69

3-9. NMR spectra of $^{13}\text{CH}_3\text{ReO}_3$ adsorbed onto dehydrated silica-alumina, at two different loadings, 0.4 wt.% Re and 10 wt.% Re: (a) single-pulse ^1H MAS NMR spectra, (b) ^{13}C CPMAS NMR spectra	78
3-10. 2D $^{13}\text{C}\{^1\text{H}\}$ HETCOR MAS NMR spectrum for silica-alumina modified with $^{13}\text{CH}_3\text{ReO}_3$ (10 wt.% Re) recorded at room temperature with a mixing time of 3 ms and a spinning speed of 12 kHz.....	79
3-11. Single pulse ^{13}C NMR spectra for $^{13}\text{CH}_3\text{ReO}_3$ adsorbed onto dehydrated silica-alumina: (a) 6.5 wt.% Re, with the same number of scans under both MAS conditions (12 kHz, red) and static conditions (black), (b) MAS spectra (12 kHz) before (10 wt.% Re, red) and after (6 wt.% Re, black) desorption of volatiles at 80 °C for 6 h	81
3-12. ^{13}C CP NMR spectra for CH_3ReO_3 grafted onto dehydrated silica-alumina (10 wt.% Re). Both spectra were recorded at -100°C, (a) with 8 kHz MAS, (b) without spinning.....	82
3-13. 2D $^{13}\text{C}\{^1\text{H}\}$ HETCOR MAS NMR spectrum for silica-alumina modified with $^{13}\text{CH}_3\text{ReO}_3$ (10 wt.% Re), recorded at -100°C with a mixing time of 12 ms and a spinning speed of 8 kHz	82
3-14. IR spectra of dehydrated silica-alumina before and after adsorbing CH_3ReO_3 (ca. 10 wt.% Re)	88
3-15. ^{13}C CPMAS NMR spectrum for dehydrated silica-alumina modified with hexamethyldisilazane, then by $^{13}\text{CH}_3\text{ReO}_3$ (1 wt.% Re).....	90
3-16. 2D $^{13}\text{C}\{^1\text{H}\}$ HETCOR MAS NMR spectrum for dehydrated silica-alumina modified first with hexamethyldisilazane followed by $^{13}\text{CH}_3\text{ReO}_3$ (1 wt.% Re) recorded at room temperature with a mixing time of 3 ms and a spinning speed of 12 kHz.....	90
3-17. NMR spectra of $^{13}\text{CH}_3\text{ReO}_3$ adsorbed onto dehydrated silica (4 wt.% Re): (a) single-pulse ^1H MAS NMR spectrum, (b) ^{13}C CPMAS NMR spectrum....	92
3-18. 2D $^{13}\text{C}\{^1\text{H}\}$ HETCOR MAS NMR spectrum for silica modified with $^{13}\text{CH}_3\text{ReO}_3$ (4 wt.% Re), recorded at RT with a mixing time of 3 ms and a spinning speed of 12 kHz	92
3-19. ^1H MAS NMR spectra for (a) dehydrated silica, (b) CD_3ReO_3 (ca. 1 wt.% Re) on dehydrated silica, both recorded with 12 kHz MAS.....	94
3-20. Kinetics of propylene metathesis over 10 mg CH_3ReO_3 /silica-alumina containing 1 wt.% Re and 10 wt.% Re, at 0 °C.....	95
3-21. Hydrated silica-alumina with grafted $^{13}\text{CH}_3\text{ReO}_3$ (1 wt.% Re): (a) ^1H single-pulse MAS NMR, (b) ^{13}C CPMAS NMR spectrum.....	98
3-22. 2D $^{13}\text{C}\{^1\text{H}\}$ HETCOR MAS NMR spectrum for hydrated silica-alumina modified with $^{13}\text{CH}_3\text{ReO}_3$ (1 wt.% Re).....	99
3-23. ^1H single-pulse MAS NMR spectra for zeolite HY: (a) hydrated, as-received, (b) calcined, (c) $^{13}\text{CH}_3\text{ReO}_3$ -grafted (6 wt.% Re)	102

3-24. 2D $^{13}\text{C}\{^1\text{H}\}$ HETCOR MAS NMR spectrum for zeolite HY modified with $^{13}\text{CH}_3\text{ReO}_3$ (6 wt.% Re).....	104
4-1. Solid state ^{13}C single-pulse spectra of HDA-capped InGaP nanocrystals recorded under MAS at 12 kHz for the (a) unetched and (b) HF-etched sample.....	110
4-2. Optical absorbance spectra of 4.5 nm $\text{In}_{0.91}\text{Ga}_{0.09}\text{P}$ nanoparticles (a) as-synthesized and (b) after HF etching; (c) shows the emission spectrum ($\lambda_{\text{exc}} = 420 \text{ nm}$) of the same etched nanoparticles as in (b)	111
4-3. Solid state ^{31}P single-pulse spectra recorded under MAS conditions (12 kHz) for (a) unetched and (b) HF etched InGaP nanocrystals.....	112
4-4. $^{31}\text{P}\{^1\text{H}\}$ FSLG HETCOR spectra of unetched InGaP nanocrystals recorded under MAS at 12 kHz with CP contact times of (a) 2 ms, (b) 15 ms.....	116
4-5. ^{31}P CPMAS spectra of unetched InGaP nanocrystals recorded with CP contact times of (a) 2 ms, (b) 15 ms and a spinning speed of 12 kHz.....	119
4-6. Plots of the integrated ^{31}P peak intensities from ^1H - ^{31}P CPMAS measurements as a function of CP contact times for the phosphorous peaks at 24 ppm, 1 ppm, -9 ppm and -210 ppm	120
4-7. 2D DQ $^{31}\text{P}\{^{31}\text{P}\}$ NMR spectrum of unetched InGaP nanocrystals recorded under MAS at 12 kHz and an excitation time of 1.66 ms.....	122
4-8. Spin-echo ^{115}In MAS NMR spectra of InGaP nanoparticles (a) before and (b) after etching, recorded at a spinning speed of 14 kHz	126
4-9. Spin-echo ^{71}Ga MAS NMR spectra of InGaP nanoparticles (a) before and (b) after etching, recorded at a spinning speed of 14 kHz	128
4-10. Schematic diagram depicting structures and changes produced in 4.5 nm $\text{In}_{0.91}\text{Ga}_{0.09}\text{P}$ nanoparticles by HF surface etching	131
5-1. Energetically most favorable grafting site	138
5-2. ^{13}C MAS NMR spectrum and computational models of CH_3ReO_3 grafted at high loading (10 wt.% Re) onto silica-alumina	139
5-3. Structural changes upon HF-etching lead to enhanced photoluminescence in InGaP nanoparticles.....	143

List of Schemes

1-1. General olefin metathesis reaction	4
1-2. Different types of olefin metathesis reactions	5
1-3. Chauvin's mechanism for the catalyzed olefin metathesis	6
1-4. Methyl-oleate metathesis products and their uses	6
1-5. Origin of silica-alumina Lewis acidity by dehydration	11
2-1. Simplified illustration of Kohn-Sham approach to DFT	37
2-2. Simplified diagram for calculations of molecular orbitals	38
3-1. DFT-calculated reaction energies and structures for two models of the interaction between a siloxane-capped aluminosilsesquioxane monosilanol cube (representing the silica-alumina surface) and CH_3ReO_3	74
3-2. DFT-calculated structures and reaction energies for postulated mobile forms of CH_3ReO_3 interacting with an aluminosilsesquioxane cube (representing the silica-alumina surface), and an immobile CH_3ReO_3 -aluminosilsesquioxane adduct.....	84
3-3. DFT-calculated structures and reaction energies for CH_3ReO_3 interacting by H-bonding with an aluminosilsesquioxane monosilanol cube (representing the silica-alumina surface) and a silsesquioxane monosilanol cube (representing the silica surface)	85
3-4. DFT-calculated structure and reaction energy for CH_3ReO_3 interacting by H-bonding with a bridging hydroxyl formed upon reaction of a terminal silanol with the Al corner of an aluminosilsesquioxane cube (representing the silica-alumina surface)	87
3-5. DFT-calculated structures and reaction energies for CH_3ReO_3 interacting with an aluminosilsesquioxane cube (representing the silica-alumina surface) in the presence of water	101

List of Tables

1-1. Industrial productions based on olefin metathesis.....	4
2-1. NMR periodic table showing nuclei with $I = 1/2$, $I > 1/2$ and nuclei with both options	24
2-2. NMR properties of selected nuclei.....	31
3-1. Comparison of bond distances reported for CH_3ReO_3	61
3-2. Comparison of EXAFS path lengths for CH_3ReO_3 grafted onto dehydrated silica-alumina, with DFT-calculated bond distances for two models of CH_3ReO_3 grafted onto an aluminosilsesquioxane cube	70
4-1. InGaP nanocrystal ^1H - ^{31}P cross-relaxation time constants, T_{PH} , for the various ^{31}P peaks.	120
4-2. Summary of ^{31}P site assignments, positions and characterization methods for unetched and HF-etched InGaP nanocrystals	124

List of Images

2-1. Photos of (a) MeReO_3 , (b) silica-alumina, (c) MeReO_3 grafted onto uncalcined silica-alumina, (d) MeReO_3 grafted onto calcined silica-alumina	45
4-1. TEM images of (a) unetched and (b) etched 4.5 nm-sized $\text{In}_{0.91}\text{Ga}_{0.09}\text{P}$ nanocrystals	110

Chapter 1

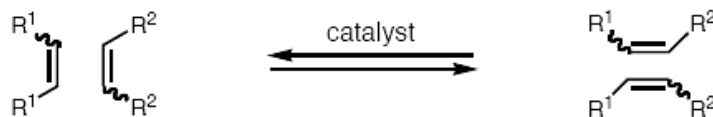
Introduction

1.1 Olefin metathesis

The Nobel Prize in Chemistry was awarded in October 2005 to Yves Chauvin, Robert H. Grubbs and Richard R. Schrock for “the development of the metathesis method in organic synthesis”.¹ The Press release from the Royal Swedish Academy of Sciences further reads: “This year's Nobel Prize Laureates in chemistry have made metathesis into one of organic chemistry's most important reactions. Fantastic opportunities have been created for producing many new molecules- pharmaceuticals, for example. Imagination will soon be the only limit to what molecules can be built!” The significance of their work is manifold, perhaps most noteworthy is that it represents a contribution to green chemistry in that the increase in chemical efficiency offered by metathesis for chemical syntheses creates new synthetic pathways of fewer reaction steps that generate less waste. New catalyst developments allow operation under milder reaction conditions, such as lower temperature, and also in the presence of stabilizers, fillers, and additives.² Some catalysts can also function in polar solvents and air, and have the ability to catalyze the metathesis of functionalized olefins. Several existing or imminent commercial operations which include olefin metathesis as a key step are summarized in Table 1-1. The catalysts used in these reactions function at low pressures and mild temperatures, which serve to maximize selectivity.³ Nevertheless, these processes often operate near the limit of economic viability because of low catalyst efficiency.

The word metathesis is assembled from the Greek words *meta* (change) and *thesis* (place) indicating a “change of place”. Applied to olefins it describes a chemical reaction in which the carbon-carbon double bonds are cleaved and reassembled on account of the catalyst such that the alkyl substituents on the C=C bond are

exchanged, Scheme 1-1.^{4, 5} The importance of the metathesis reaction lies in the fact that it changes a carbon double bond which is unreactive with many reagents to one that is.

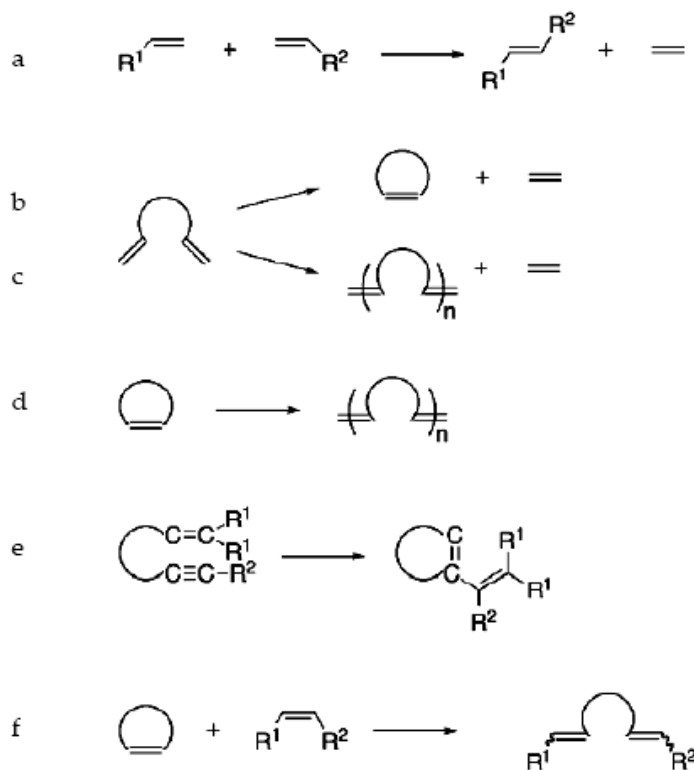


Scheme 1-1. General olefin metathesis reaction.

Table 1-1. Industrial productions based on olefin metathesis.

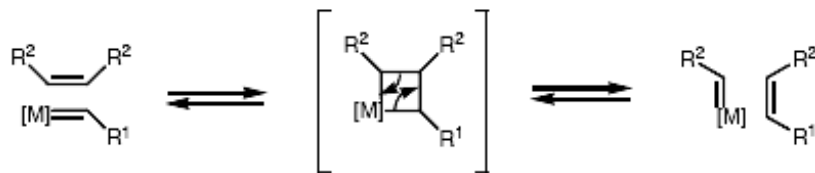
Process	Company (annual production capacity)	Reaction	Use	Catalyst (operating conditions)
SHOP (Shell Higher Olefins Process)	Shell (1,200,000 t/a)	α -olefins \rightleftharpoons linear internal alkenes (C ₁₁ -C ₁₄)	detergent alcohols, plasticizers	MoO ₃ /Al ₂ O ₃ (100-125°C, 10 bar)
Phillips neohexene process	Phillips (1400 t/a)	^t BuCH=C ^t Bu + CH ₂ CH ₂ \rightleftharpoons ^t BuCH=CH ₂ + CH ₂ =CMe ₂	intermediate in bicyclic musks	WO ₃ /SiO ₂ (370°C, 30 bar)
ROMP (Ring-Opening Metathesis Polymerization)	Hulls CdF Chemie Hercules Hitachi	Cycloalkenes \rightarrow polyalkenamers	specialty (small volume) polymers for reaction injection molding	soluble Ru catalyst
FEAST (Further Exploitation of Shell Advanced Technology)	Shell (not currently operating)	Cycloocta-1,5-diene + CH ₂ CH ₂ \rightarrow hexa-1,5-diene + deca-1,9-diene	cross-linking agents, specialty (co)monomers, aldehydes	Re ₂ O ₇ /Al ₂ O ₃ promoted with SnBu ₄ (0-20°C, 1-2 bar)
Meta-4	Axen	CH ₂ CH ₂ + MeCH=CHMe \rightleftharpoons 2 MeCH=CH ₂	monomer for polypropylene	Re ₂ O ₇ /Al ₂ O ₃ (35°C, 60 bar, liquid phase)
Phillips Triolefin Process	Phillips (not currently operating)	CH ₂ =CH ₂ + MeCH=CHMe \rightleftharpoons 2 MeCH=CH ₂	Ethylene or propylene, depending on market demand	WO ₃ /SiO ₂ , Na ⁺ -doped (350-425°C, gas phase)
Olefin Conversion Technology (OCT)	ABB Lummus	CH ₂ =CH ₂ + MeCH=CHMe \rightleftharpoons 2 MeCH=CH ₂	monomer for polypropylene	WO ₃ /SiO ₂ , Na ⁺ -doped (350-425°C, gas phase)

Examples of different types of olefin metathesis reactions are shown in Scheme 1-2. and involve (a) cross metathesis (CM), (b) ring-closing metathesis (RCM), (c) acyclic diene metathesis polymerization (ADMEP), (d) ring opening metathesis polymerization (ROMP), (e) enyne metathesis (EYM) and (f) ring opening cross metathesis (ROCM).



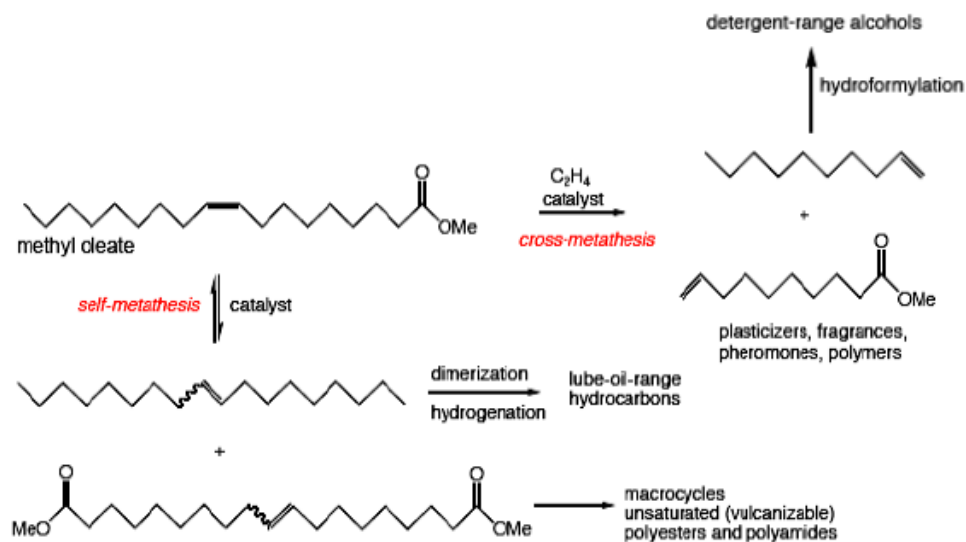
Scheme 1-2. Different types of olefin metathesis reactions.

The crucial involvement of a metal carbene species in the mechanism of olefin metathesis was first suggested by Hérisson and Chauvin (Scheme 1-3).⁶ This Chauvin mechanism involves a metal-alkylidene, the coordination of the olefin onto the metal atom of this species forming a metallocyclobutane intermediate which then cleaves to form a new olefin and new metal carbene. This new olefin contains a carbene from the catalyst and another from the starting olefin.



Scheme 1-3. Chauvin's mechanism, proposed in 1971, for the catalyzed olefin metathesis.

The application of olefin metathesis in oleochemistry will in the future be particularly important, as it is a clean catalytic reaction that will enable the development of chemical technologies based on biorenewable feedstocks, such as seed oils (e.g. olive oil, rapeseed oil, soybean oil) as sustainable alternatives to petroleum oils. Metathesis reactions increase the versatility of seed oil chemistry and can convert natural oils and fats into valuable chemical products, such as soaps, lubricants, solvents and biodiesel, directly or only in a few steps. Potential targets for platform chemicals derived from seed oil (after transesterification to fatty esters such as methyl oleate), using metathesis are shown in Scheme 1-4.⁷



Scheme 1-4. Methyl-oleate metathesis products and their uses.

1.2 Olefin metathesis catalysts and supports

1.2.1 Homogeneous catalysts

The catalysts that are the subject of the Nobel Prize awarded in 2005 are in fact employed in homogeneous catalysis. They are currently used in the production of fine and specialty chemicals, in organic syntheses and polymer chemistry.⁸ Polymerization reactions carried out with the aid of homogeneous metathesis catalysts allow for a high degree of control over polymer morphology and facilitate the design of highly specialized polymers. It can also occur in the presence of additives, which helps to reduce or eliminate subsequent blending steps. Commercial ROMP polymers include polycyclooctane, polynorbornene and polydicyclopentadien, with their applications ranging from asphalt formulations, car body components, corrosive containers and electrical equipment housing.

Some of the transition metals that have been reported to be active for the metathesis of olefins are Ti, Nb, Mo, Ru, Ta, W, Re, Os and Ir with Mo, W, Re being the most effective amongst them. It is universally agreed upon, that the key structural feature of the metathesis activity is a carbene species (shown in Scheme 1-3.) as proposed originally by Chauvin.

One of the early catalysts for olefin metathesis, discovered in the late 1970s, was pentacarbonyl(diphenyl-methylene)tungsten, Figure 1-1a. It was the first compound to catalyze the metathesis polymerization of acetylene and of enyne metathesis. It also has the ability to prevent acid-catalyzed side reactions and thereby possesses high selectivity for formation of *cis* alkenes over *trans*.⁹ The

homogeneous catalysts developed more recently have appreciably higher activity and stability. The molybdenum-based Schrock catalyst, Figure 1-1b, is efficient for the metathesis of functionalized olefins, but is less reactive than many tungsten-based catalysts.²

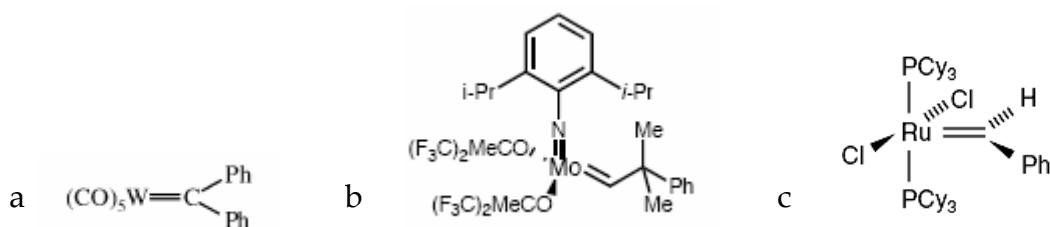


Figure 1-1. Homogeneous olefin metathesis catalysts: **(a)** pentacarbonyl(diphenyl-methylene) tungsten, **(b)** commercial Schrock molybden catalyst (i-Pr= iso-propyl, Ph= phenyl), **(c)** Grubbs 1st generation ruthenium catalyst (Ph= phenyl, Cy= cyclohexyl).

The most widely-used homogeneous catalysts are those based on isolated or in situ-generated Ru carbenes with ancillary phosphine ligands (first-generation Grubbs' catalyst), Figure 1-1c.¹⁰ Although they are functional-group-tolerant, their cost and inherent instabilities make them ill-suited for prolonged use in large scale industrial production; nevertheless some small volume specialty polymers are in fact produced in this way. Activity and stability issues have been overcome with the second-generation Grubbs' catalysts, in which one phosphine ligand is replaced by a strongly σ -donating and kinetically inert *N*-heterocyclic carbene.¹¹ Nonetheless, it are these relatively exotic ligands which make members of this catalyst family too expensive for the production of commodity chemicals, and the presence of phosphine and/or chloride ligands can also be incompatible with some processes.

1.2.2 Heterogeneous catalysts

For many industrial applications heterogeneous metathesis catalysts are much more desirable than the homogeneous Ru catalysts because of the more facile, and much less costly, catalyst separation and recycling and the ability to use gas phase reactors. Commercial processes involving olefin metathesis with heterogeneous catalysts include the Philips Triolefin process, the Philips Neohexene process, the Shell SHOP process, the Shell FEAST process, Axens' Meta-4 process, and ABB Lummus Global's OCT process, all of which use olefinic feedstocks containing no polar functionality (see Table 1-1.). A heterogeneous catalyst with a reasonable lifetime and productivity in the presence of polar functional groups and protic impurities has yet to be identified, a serious drawback which dramatically limits the commercial potential for this technology.

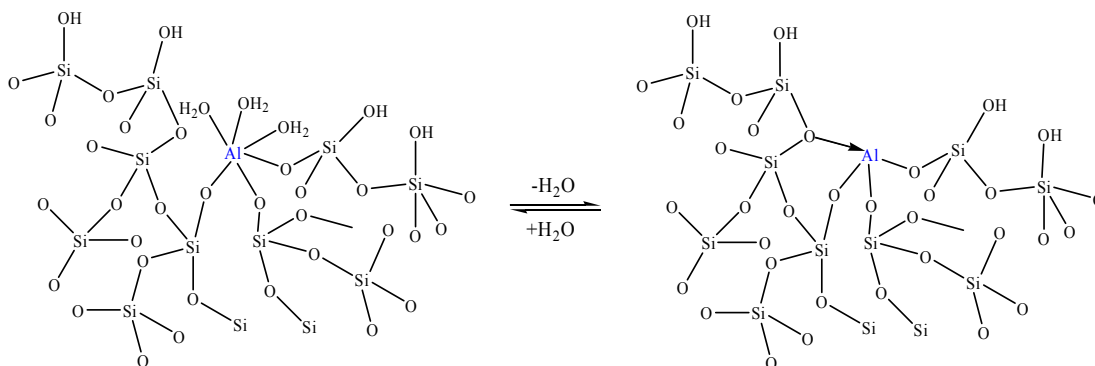
Heterogeneous metathesis catalysts are normally dispersed on and supported by solid oxide catalysts and typically used in gas-phase flow systems operating from 0-400 °C. There are several methods of dispersing the catalyst onto a solid support: dry mixing, coprecipitation, impregnation of catalyst precursor followed by calcination, and chemical vapor deposition. The most common supports for heterogeneous olefin metathesis catalysts are SiO₂ and Al₂O₃, which in many cases also play a critical role in activating the catalyst. Common heterogeneous metathesis catalysts include MoO₃ supported on alumina, WO₃ supported on silica and Re₂O₇ on alumina.

Fundamental studies of truly heterogeneous catalyst systems are among the most challenging areas of catalyst research since the nature and inherent distribution of the active sites often renders their identification ambiguous at best. The use of surface organometallic chemistry with metal complexes grafted onto oxide supports, however, generates a class of hybrid catalysts, which bridge the realms of homogeneous and heterogeneous catalysis. They differ from heterogeneous catalyst in that they retain much of their molecular identity and thereby produce active sites with a high degree of compositional uniformity. Unlike homogeneous catalysts (and their “heterogenized” derivatives, the tethered catalysts) they have important advantages given the intimate interaction with the solid support, which can result in new modes of catalyst activation. These supported organometallic catalysts have been shown to possess remarkable activity in C-H and C-C bond activation¹² and olefin polymerization¹³, and often do that under very mild reaction conditions. An additional advantage of these molecular organometallic complexes is that synthetic techniques can readily incorporate specific design elements into these supported catalysts.

1.2.3 Metal oxide supports: Silica-alumina

High surface area forms of amorphous silica-alumina are commonly used both as catalysts themselves, e.g. in the cracking of heavy oils¹⁵, and as catalyst supports. While the pure materials silica and alumina are not acidic, a dispersion of at least 10 wt.% alumina into a silica substrate results in a large increase in the acidity, especially after heat treatment. The surface of amorphous silica-alumina is composed of silanol groups, which are Brønsted acid sites, and Lewis acidic aluminum sites (Scheme 1-5). The acidic properties of the silica-alumina surface

can furthermore be varied by the pretreatment temperature. As surface bound water is liberated upon heating, octahedral Al sites become tetrahedrally coordinated, and acquire such Lewis acidic properties.¹⁶



Scheme 1-5. Origin of silica-alumina Lewis acidity by dehydration.

1.3 Heterogeneous rhenium catalysts for olefin metathesis: methyltrioxorhenium CH_3ReO_3

Heterogeneous rhenium catalysts are very attractive as olefin metathesis catalysts because they are highly active at relatively low temperatures. However, they possess rather low tolerance of polar functional groups, which effectively prevents the use of metathesis processing to biorenewable feedstocks. One notable exception are certain Re-based catalysts (e.g. $\text{Re}_2\text{O}_7/\text{Al}_2\text{O}_3$) promoted by alkyltin or alkyllead reagents, which do exhibit modest activity for metathesis of functionalized olefins.¹⁴ Once these catalysts become deactivated, however, they are not regenerable by calcination since the activator oxide formed upon calcination acts as a catalyst poison. Thus there exists an urgent need for longer-lived, highly active and selective heterogeneous catalysts which can tolerate

polar groups, and this imperative has led to the investigation of methyltrioxorhenium, CH_3ReO_3 , Figure 1-2., as a catalyst for olefin metathesis.

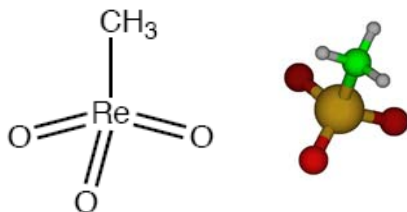


Figure 1-2. The structure of methyltrioxorhenium.

The mechanisms by which CH_3ReO_3 catalyzes the homogeneous epoxidation of olefins and the olefination of aldehydes are now fairly well-understood.¹⁵ In contrast, the origin of its reactivity in olefin metathesis remains unclear, particularly the step in which the initiating carbene is formed. Although tautomerization to $\text{CH}_2=\text{ReO}_2(\text{OH})$ occurs upon UV irradiation, this carbene is not thermally accessible,^{16, 17} and CH_3ReO_3 shows no reactivity towards olefins in solution. Metathesis activity is conferred by interaction with a Lewis acid, either soluble (e.g., $\text{R}_n\text{AlCl}_{3-n}$, AlCl_3 or $\text{AlCl}_3/\text{SnMe}_4$)^{18, 19} or solid (e.g. silica-alumina, alumina, niobia or zeolite Y).¹⁹⁻²² Interestingly, a methylene tautomer of CH_3ReO_3 was formed in the presence of SnMe_2Cl_2 by trapping with pyridine,²³ however, no reactivity for the product was reported.

Early accounts presented conflicting evidence for direct involvement of a carbene tautomer of Lewis-acid activated CH_3ReO_3 in metathesis. In a study of 1-butene homometathesis catalyzed by CD_3ReO_3 supported on silica-alumina, the deuterium label was incorporated in the olefinic products as both $\text{CD}_2=\text{CHCH}_2\text{CH}_3$ and $\text{CD}_2=\text{CH}_2$.¹⁹ Reaction of trans-2,5-dimethyl-3-hexene with $^{13}\text{CH}_3\text{ReO}_3$ supported on niobia produced 3-methyl-1-butene, the expected

product of a metathesis reaction with a carbene site $\text{Re}=\text{CH}_2$, but the olefin contained less than 5% of the ^{13}C -label.²⁴ However, the mechanisms of D and ^{13}C transfer to olefin may differ; furthermore, CH_3ReO_3 may not interact in the same way with the different oxide supports, since niobia, unlike silica-alumina, readily exhibits oxygen non-stoichiometry.²⁵

Even the structure of grafted CH_3ReO_3 remains obscure. Metathesis activity was correlated with Lewis acidity for the $^{13}\text{CH}_3\text{ReO}_3/\text{niobia}$ catalyst,²¹ although no model for the grafted site was proposed. On silica-alumina, grafting of CH_3ReO_3 via condensation with a pair of adjacent surface hydroxyl groups was assumed,¹⁹ by analogy to the homogeneous reactions of CH_3ReO_3 with diols.²⁶⁻²⁸ Computational studies showed such a condensation reaction with the molecular disilanol $\text{H}_2\text{Si}(\text{OH})\text{OSi}(\text{OH})\text{H}_2$ to be endothermic.¹⁷ Nevertheless, subsequent tautomerization of the silanolate complex was proposed, aided by relaxation of the silica surface via protolytic opening of a strained siloxane ring. Understanding the CH_3ReO_3 -support interaction is the first step towards explaining how heterogeneous rhenium-based catalysts acquire their unique metathesis activity: both CH_3ReO_3 on silica-alumina^{19, 22, 29} and alumina-supported perrhenates promoted by SnR_4^3 are capable of transforming even functionalized olefins at room temperature.

Upon deposition onto amorphous silica-alumina, CH_3ReO_3 becomes a catalyst for the metathesis of olefins.^{18, 19} The silica-alumina serves as an activator as well as a support, since solutions of CH_3ReO_3 do not catalyze homogeneous olefin metathesis. The amorphous nature of the silica-alumina is crucial, since crystalline aluminosilicates are much less effective in activating CH_3ReO_3 . It was originally suggested,¹⁸ and recently demonstrated, that CH_3ReO_3 forms upon

treatment of oxide-supported perrhenates with a SnMe_4 promoter, which simultaneously confers tolerance of olefins bearing functional groups.³⁰ Amorphous solid oxides generally possess a variety Lewis and Brønsted acidic and basic centers which can serve as adsorption sites for organometallic catalysts. Positive identification of the structures of the grafted sites and their relationship to catalyst activity is very challenging in the absence of both site uniformity and long-range order. Solid state NMR spectroscopy can be a powerful tool for investigating supported organometallic catalysts, since the chemical shift can be highly sensitive to variations in the ligand environment, while the linewidth provides information about site mobility. Furthermore, grafted organometallic complexes are readily modified by selective introduction of isotope labels.

In this work, solid state NMR experiments are combined with other spectroscopic analyses (such as IR and EXAFS) and computational calculations to explore the structures of the major sites formed by grafting CH_3ReO_3 onto amorphous silica-alumina, and their relationship to the olefin metathesis activity of these materials.

1.4 Heterogeneous catalysis and nanoscience

The majority of today's industrial catalysts consist of high surface-area solids onto which the active component is dispersed in form of small particles with dimension of 1-20 nm. The initial incentive to reduce the particle size of the active components was to maximize the surface area exposed to the reactants and thus minimize the specific cost per function. Recent advances in nanoscience

have contributed to improved characterization methods and to novel synthetic approaches for these systems.³¹⁻³³

Particles ranging in size from 1 to 50 nm exhibit physical and chemical properties that are intermediate between those of the smallest element from which they can be composed (such as a metal atom or the stoichiometric unit of a metal oxide) and those of bulk material. The catalytic activity, selectivity and physical properties of nanoparticles are strongly dependent on their size, shape and surface structure, as well as on their bulk and surface composition. It is therefore of crucial importance to characterize structure and composition of such nanoparticles to contribute to a molecular-level understanding of the structure-performance relationship.

1.5 Description of nanocrystals and surface reconstruction

Nanotechnology is one of the most prominent disciplines in science and technology today as it bridges the fields of biology, physics, chemistry and engineering, and holds enormous promise for much improved, as well as completely new technologies, in many different areas. A structure-based, molecular level understanding of the function of the nanosized materials involved does, however, require innovative approaches in the characterization methods used. Moreover, a successful development of nanomaterials requires a thorough understanding of surface chemistry, reconstruction and inorganic/organic interfaces, as these are associated with the physical properties (electronic and optical) in nanoscale particles.³⁴⁻⁴⁰ Semiconductor nanocrystals, for

example, offer a unique opportunity to observe the evolution of physical properties with size as these quantum dots are applied in a wide range of areas, including solid state lighting, light emitting diodes and biological labeling.⁴¹⁻⁵⁰

Nanocrystals are indeed crystalline, possess crystal facets, but are usually approximated by a spherical model. The structural features of a nanocrystal are shown in Figure 1-3. and comprise a core inorganic bulk structure, a reconstructed inorganic surface shell and an organic passivating layer.⁵¹⁻⁵⁵

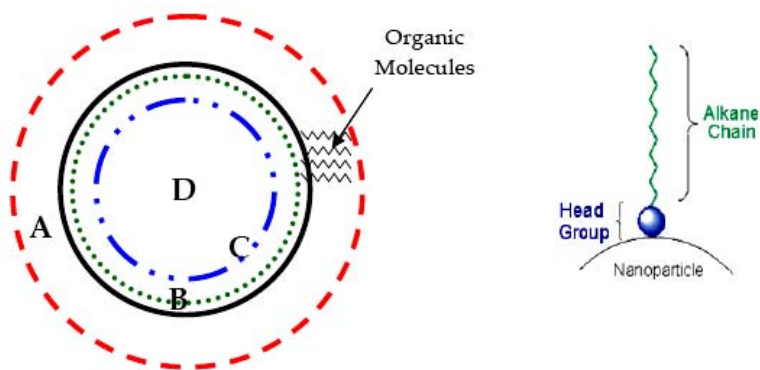


Figure 1-3. Domains of a nanocrystal: (A) passivating layer, (B) surface of particle, (C) near-surface of particle, (D) core of particle.

The passivation layer, region A, can be described as a three-dimensionally constrained, self-assembled monolayer of tightly packed organic amphiphiles which thermodynamically stabilizes the surface through a head group-surface interaction^{54, 55} and makes the particle soluble in various liquids. Molecular level interactions take place at the inorganic-organic interface, region B, between the surface atoms as well as the head group of the passivant and the outermost surface sites.^{56, 57} Region C, the near-surface sites, consists of the top layer of the particle and the crystallographic plane below and is prone to reconstruction.^{54, 58-60}

A bulky core forms region D of the nanocrystal and it is only minimally affected by surface interactions. Reconstruction may also occur in the core, but only passivant-driven surface reconstruction has recently been suggested to influence the observed optical properties of CdSe and InP nanomaterials.^{54, 58-65} The exposed atoms on the facets dictate the nature of the organic passivant interaction and can lead to surface reconstruction following passivant binding. This interaction has been shown to affect important aspects of the materials including size, shape, stability, photoluminescence and oxidation.^{58, 61, 65-70} The ability of the passivant layer to provide stability in appropriate solvents is also important for technological applications as are its terminal functionalities, which allow for selective interactions in the fabrication of nanoscale 2- and 3-dimensional architectures.^{67, 71-74} Because of the significance of the passivation layer and the corresponding inorganic/organic interface, investigations into the nature of the organic ligands on the surface of the particles are of considerable importance.

The nature of the surface interfacial region is most crucial for the understanding of the correlation between optical response and reconstruction but is also most difficult to access experimentally because of the low ratio of surface species relative to core species in nanoscale materials. Many standard spectroscopic techniques, such as photoluminescence, X-ray diffraction and transmission electron microscopy have been used to gain information on optical nature, size, facets, and crystal structure of a variety of nanomaterials. These studies however do not reveal unambiguous structural features or details because of the small number of atoms and high surface to volume ratio. Nuclear magnetic resonance spectroscopy, however, is highly sensitive to local chemical and electronic environments, is element-specific, quantitative, and can be used to selectively

probe distances with special pulse techniques. NMR therefore offers an invaluable analytical method for the observation of reconstruction in nanomaterials and for information on surface and interface arrangements in nanocrystals. ^{13}C and ^1H NMR have been employed as techniques sensitive to local environments and mobility in solution and the solid state to probe the binding sites (chemical shift) and freedom of rotation (line width) of the passivant layer in nanocrystals.^{56, 57, 67, 69, 75-79} Vital information about the nature, binding motif, ligand exchange, solubility and spatial proximities of the corresponding organic ligands can be obtained.

1.6 Semiconducting quantum dot systems (CdSe, InP, InGaP)

Semiconductor nanocrystals exhibit unique size-dependent optical and electronic properties that are strongly influenced by reconstruction of the surface and of the crystal lattice of the particles. They have therefore been widely studied by optical spectroscopies^{62, 65, 80-82} which have provided valuable information on these materials. Optical excitations are, however, delocalized and therefore respond to an average environment in the nanocrystal which limits the insight into the nature of the material surface. Solid state NMR on the other hand has been shown to selectively probe distinct regions of the nanocrystal by utilizing special pulse sequences.^{51, 75, 76, 79, 83} This ability of NMR methods represents a powerful tool for probing the surface, near surface and core species of semiconductor nanocrystals and thereby elucidate distinct size-dependent properties of the respective regions in relation to the particle as a whole.

Concerns about the toxicity of Se and Te based II-VI materials have led to an interest in developing the chemistry of III-V semiconductor nanocrystals (InP, GaP, InN, GaN) and their ternary analogs (i.e InGaP, InAlP, etc).^{60-62, 64, 65, 83-91} Extensive investigations of the widely studied CdSe have led to a model which invokes surface reconstruction events as a critical manipulator of the physical properties of these systems.^{54, 70, 75, 92-94} A number of recent investigations have addressed the details of these reconstructive processes in order to develop an atomistic picture of the nanocrystal surface, near-surface and core atoms with the use of X-ray absorption (XAS) and neutron techniques⁹⁴⁻⁹⁸, X-ray photoelectron spectroscopy (XPS)^{61, 81, 85, 89, 91, 99}, transmission electron microscopy (TEM)^{82, 100} and solid state NMR^{51, 61, 75, 76, 78, 79, 83, 101}. A lack of knowledge about the nature of the surface reconstruction, including vacancies, and the oxidation process on the surface of the particle in nanoscale materials, however, makes it difficult to systematically design these materials with the desired physical properties in the manner in which it is carried out for quantum well structures grown by molecular beam epitaxy.

The influence of surface states in InP materials has been investigated in both bulk and nanoscale materials.^{61-64, 83, 89, 91, 102-109} Chemical or thermal treatment of bulk InP materials leads to surface oxidation and reconstruction.^{102-104, 106-109} Nanocrystalline InP has been reported to have enhanced photoluminescence quantum efficiency when treated by wet-chemical etching of the nanoparticle surfaces.^{61, 63, 64, 90, 91, 110} A number of different models have been suggested for the correlation between optical properties and molecular structure in pre and post hydrogen fluoride- etched InP quantum dots. Various models for HF etching of the surface-passivated InP nanoparticles have been proposed, such as a filling of phosphorus vacancies at the surface with fluoride ions with a small amounts of

phosphorus vacancies left in the core;^{63, 64} or the removal of non-passivated phosphorus atoms from the particle surface, followed by increased surface passivation with fluorine and reduction of phosphorus dangling bonds (vacancies).⁶¹ Alivisatos *et al.* observed that a thin oxide layer in lyothermally-prepared InP nanomaterials may be important for the observation of photoluminescence.⁸⁹ These findings clearly point to changes in composition and ordering of the nanoparticle surface upon etching, but address neither the chemical nature, growth, depth or connectivity of the oxide species nor the details of the surface reconstruction following chemical treatment.

In this work 1D and 2D MAS ³¹P NMR investigations as well as ⁷¹Ga and ¹¹⁵In NMR measurements of thermally-grown, hexadecylamine-coated InGaP quantum dots before and after HF etching have been carried out to significantly expand on previous studies. Valuable information on nature and position of the gallium and indium sites, as well as on the correlation of surface reconstruction and improved PL quantum efficiency in etched semiconducting nanocrystals are thereby obtained.

Chapter 2

Characterization Techniques and

Experimental Details

This section consists of an overview of the various characterization techniques utilized in this thesis. Solid state NMR techniques were the principal analytical method used and are therefore more extensively described including the pulse sequences employed in these experiments. The basic concepts behind Density Functional Theory (DFT) calculations and Extended X-ray Absorption Fine Structure (EXAFS) measurements are then briefly introduced. For further and more detailed reading on these characterization techniques various standard textbooks, review articles and the references provided herein may be consulted. Synthesis procedures, materials used as well as the experimental settings for each technique are given separately for the respective metathesis and nanocrystal subjects.

2.1 Solid state Nuclear Magnetic Resonance (NMR) spectroscopy

2.1.1 Basics of NMR spectroscopy

Solid state NMR has emerged as a powerful and highly versatile tool for the study of molecular structures and dynamics in solids.¹¹¹ Each isotope of an element (with a natural abundance N) can be assigned a ground-state nuclear spin quantum number (I) which can be integral, half-integral or zero. Nuclei with a ground-state values of $I = 0$, e.g. ^{12}C , ^{16}O or ^{32}S , give no NMR signal and have little influence on NMR properties. The active NMR nuclei in the periodic table are shown in Table 2-1.¹¹² Nuclei with values of I up to $9/2$ can currently be studied by NMR.

Table 2-1. NMR periodic table showing nuclei with $I=1/2$ (white), $I>1/2$ (violet) and nuclei with both options (yellow).

The NMR periodic table is color-coded based on the nuclear spin quantum number I . A legend indicates:

- White: $I = 1/2$ nuclei
- Violet: $I > 1/2$ nuclei
- Yellow: $I = 1/2$ and $I > 1/2$ nuclei

 The table includes columns for element symbol, atomic number, isotope, atomic weight, spin number, and frequency (MHz). Key elements shown include H, Li, Be, Na, Mg, K, Ca, Sc, Ti, V, Cr, Mn, Fe, Co, Ni, Cu, Zn, Ga, Ge, As, Se, Br, Kr, Rb, Sr, Y, Zr, Nb, Mo, Tc, Ru, Rh, Pd, Ag, Cd, In, Sn, Sb, Te, I, Xe, Cs, Ba, La, Hf, Ta, W, Re, Os, Ir, Pt, Au, Hg, Tl, Pb, Bi, and the lanthanide/actinide series (La, Tm, Yb).

For a nonzero value of I the nucleus has a magnetic moment μ_I given by Equation 2-1.

$$\mu = \gamma \hbar [I(I + 1)]^{1/2} \quad (\text{eq.2-1.})$$

where γ_I is the magnetogyric ratio. The most common NMR experiments are performed on $I=1/2$ nuclei, e.g. ^{13}C , ^{29}Si and ^{31}P . Recent technological advancements and new pulse sequences in solid state NMR have made the ca. 73% of NMR active nuclei that are quadrupolar ($I>1/2$) accessible. Their nuclear electric quadrupole moments shorten relaxation times and broaden lines which renders NMR experiments more challenging than for $I=1/2$ nuclei. The few integer quadrupolar nuclei investigated on a regular basis include ^2H and ^{14}N . By convention nuclear spins are labeled as I for “abundant” spins (e.g. ^1H) and S for “rare” spins (e.g. ^{13}C).

Another factor which affects the ease with which NMR signals may be observed is the nucleus dependent magnetogyric ratio, γ , which governs both the frequency with which the nucleus will precess about an externally applied magnetic field and the intensity of the resonance.

When a nucleus with a non-zero value of I is placed in a strong magnetic external field B_0 (usually between 1 and 10 T) the orientation of its spin axis becomes quantized with each possible orientation having a different energy. Electromagnetic radiation is used to flip the alignment of nuclear spins from the low energy spin aligned state to the higher energy spin opposed state. The energy required for this transition depends on the strength of the applied magnetic field but is small and corresponds to the radio frequency range of the electromagnetic spectrum.

In an external magnetic field, the Zeeman interaction describes the energy of spin I based on its orientation, either parallel or antiparallel with respect to the external field, Equation 2-2.

$$E_{Zemman} = -\hbar B_0 m_I \quad (\text{eq.2-2.})$$

with m_I being the nuclear spin quantum number (which is either $+1/2$ or $-1/2$ for a spin $1/2$ nucleus).

A basic schematic of an NMR spectrometer is shown in Figure 2-1. The sample is positioned in the magnetic field and excited via the pulsed radio frequency input circuit. The realigned magnetic field induces a radio signal in the output circuit which is used to generate the output signal. Fourier analysis of the complex

output produces the actual spectrum. The pulse is repeated as many times as necessary to allow the signals to be identified relative to the background noise.

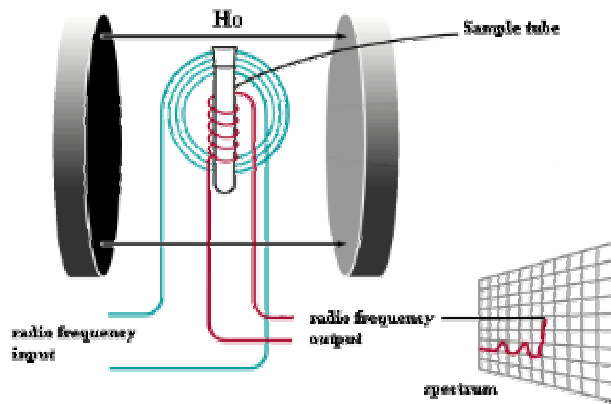


Figure 2-1. Basic arrangement of an NMR spectrometer.

2.1.2 Nuclear spin interactions and averaging techniques

An external magnetic field applied to a particular atom not only perturbs the nuclear spins of that atom, but also affects the surrounding electrons since they have magnetic moments as well. The external field induces circulating currents of electrons that in turn produce small magnetic fields (typically 10^6 times smaller than B_0) which either add to or subtract from the external field. This alters the effective magnetic field experienced by the nucleus, as thereby its resonance frequency. This so-called chemical shift is very sensitive to the chemical environment and it is anisotropic (orientation-dependence) because the atoms in molecules rarely possess spherically symmetric electron distributions.

The degree to which the electron density affects the resonance frequency of a nucleus depends on the orientation of the electron cloud with respect to B_0 . In

liquids, molecules randomly and rapidly sample the full range of orientations so that even a strongly asymmetric electron distribution will appear spherical when viewed on the NMR timescale. The chemical shift Hamiltonian H_{cs} can be divided into an isotropic and anisotropic term. For an axially symmetric shift tensor ($\delta_{11}=\delta_{22}$) the chemical shift Hamiltonian can be written as shown in Equation 2-3.

$$H_{cs} = \gamma B_0 I_z [\delta_{iso} + \frac{1}{2} \delta_{CSA} (3 \cos^2 \theta - 1)] \quad (\text{eq. 2-3.})$$

where δ_{iso} is the (isotropic) chemical shielding factor ($\delta_{iso} = 1/3(\delta_{11} + \delta_{22} + \delta_{33})$) and θ the angle between the principal axis of the chemical shift tensor and B_0 .

In solids the chemical shift anisotropy (CSA) can be averaged out when spinning the sample around a unique, well-chosen axis, so that the anisotropic term of the chemical-shift Hamiltonian is eliminated ($(3\cos^2\theta-1)=0$). This is the case when the vector between two nuclei forms an angle $\theta = 54.74^\circ$ (the magic angle) with the static magnetic field, Figure 2-2. Spinning sidebands may appear at frequencies that are integer multiples of the spinning speed, resulting from an incomplete motional averaging of the chemical shift anisotropy by the rotation (primarily at lower spinning speeds).

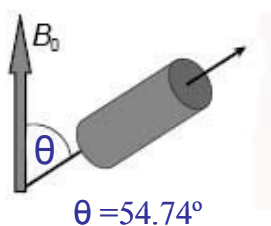


Figure 2-2. Magic angle.

Interactions between the nuclear magnetic moments of two different nuclear spins (I and S) leads to heteronuclear dipolar coupling. The magnetic field

produced by spin I will either add or subtract from the external field felt by the spin S , thereby increasing or decreasing the effective local magnetic field at the site of spin S and changing its resonance frequency. The degree to which spin I affects the magnetic field felt by spin S is represented by the heteronuclear dipolar coupling Hamiltonian in Equation 2-4.

$$H_{IS} = -d(3\cos^2\theta - 1)I_zS_z \quad (\text{eq 2-4.})$$

The parameter d is the dipolar coupling constant, Equation 2-5.

$$d = \left(\frac{\mu_0}{4\pi}\right)\left(\frac{\hbar\gamma_I\gamma_S}{r_{IS}^3}\right) \quad (\text{eq. 2-5.})$$

with r_{IS} as the internuclear distance, μ_0 then permeability of free space, I_z, S_z the z components of the nuclear spin angular momentum operators I and S , and θ the angle describing the orientation of the internuclear vector with respect to the orientation of the external magnetic field. The magnitude of the coupling between two nuclear spins depends on the internuclear distance, so that this dipolar coupling is a through-space interaction. In contrast, J-coupling requires the presence of chemical bonds. It is transferred through the electrons engaged in these bonds and thus is confined to nuclei within a molecule. Through-space dipolar coupling, however, also occurs between nuclei in different molecules.

The magnitude of the coupling is proportional to the product of the gyromagnetic ratios, inversely proportional to the cube of the internuclear distance and dependent on the orientation. The most commonly used heteronuclear dipolar decoupling techniques are Magic Angle Spinning (MAS) as well as continuous-wave spin decoupling (which also can be applied to the J-couplings).

Interactions between the magnetic fields produced by the same type of neighboring nuclear spins lead to homonuclear dipolar couplings which have perhaps the largest impact in ^1H solid state NMR spectroscopy, where the strength of this homonuclear dipolar coupling between two proton spins can routinely approach 100 kHz because of their large gyromagnetic ratio. As a result the spectra often consist of single broad peaks. Although MAS helps to reduce this linewidth it is frequently still too broad to be of general use, even at high MAS speeds (>30 kHz). Special RF pulse sequences are therefore necessary to obtain ^1H solid state NMR spectra.

In contrast to spin 1/2 nuclei, quadrupolar nuclei ($I > 1/2$) have an asymmetric distribution of nucleons which gives rise to a spheroidal (non-spherical) positive electron charge distribution described by the nuclear electric quadrupolar moment. The latter is an intrinsic property of the nucleus and therefore independent of the environment. Interactions between the electric quadrupole at the nucleus and an electric field gradient (spatial changes in electric field) caused by surrounding atoms at the site of the nucleus result in strong changes in linshapes and large linewidths.¹¹³ The first order quadrupolar interaction is characterized by the first-order quadrupolar splitting $Q(\theta, \phi)$, Equation 2-6.

$$Q(\theta, \phi) = \left(\frac{1}{2}\right)\omega_Q(3\cos^2\theta - 1 + \eta\sin^2\theta\cos^2\phi) \quad (\text{eq. 2-6.})$$

where ω_Q is the quadrupolar frequency, Equation 2-7.

$$\omega_Q = \frac{3e^2qQ}{2I(2I-1)\hbar} \quad (\text{eq. 2-7.})$$

η is the asymmetry parameter, θ and ϕ are the polar angles of the Zeeman field with the electric field gradient principal axes and e^2qQ/\hbar is the quadrupolar coupling constant. The MAS method leads to some line narrowing by removing the first order quadrupolar coupling but the secondary quadrupolar interaction is not averaged out. This secondary quadrupolar interaction becomes significant for sites where a substantial electric field gradient is present, and can broaden the signal from these nuclei to the point where it just appears as a broad hump in the baseline, which becomes “invisible” in the presence of any baseline distortion. An increasing spherical or undistorted environment of charge from the surrounding molecular environment can, on the other hand, cause the electric field gradients to cancel each other, which results in a smaller interaction and a smaller electric field gradient felt at the nucleus. The “invisible” spins then give rise to a signal that is not as broad, and then can be detected in the NMR spectra.¹¹⁴ A number of techniques, such as Multiple Quantum Magic Angle Spinning (MQMAS), have been developed to counter the effects of the second-order quadrupolar interactions to produce sharper NMR spectra of quadrupolar nuclei.¹¹⁵⁻¹¹⁸

The relaxation time for a nucleus is an additional, commonly used NMR parameter. It measures the rate at which a nucleus recovers its equilibrium properties after being disturbed and thereby gives information about dynamics of the system. There are two distinct relaxation times for a nucleus, T_1 the spin-lattice (longitudinal) relaxation time, which relates to magnetisation parallel to B_0 , and T_2 , the spin-spin (transverse) relaxation time, which refers to magnetisation perpendicular to B_0 .

The NMR properties of the nuclei measured in this work are summarized in Table 2-2.¹¹²

Table 2-2. NMR properties of selected nuclei.

Isotope	Spin	Natural abundance <i>N</i> /%	Magnetic moment μ/μ_N	Magnetogyric ratio $\gamma/10^7$ rad T ⁻¹ s ⁻¹	Quadrupole moment <i>Q</i> / 10 ⁻²⁸ m ²	Reference
¹ H	1/2	99.985	4.8371	26.7510	-	Me ₄ Si
¹³ C	1/2	1.108	1.2162	6.7263	-	Me ₄ Si
³¹ P	1/2	100	1.9581	10.829	-	85 % H ₃ PO ₄
²⁷ Al	5/2	100	4.3051	6.9706	0.149	Al(NO ₃) ₃
⁷¹ Ga	3/2	39.6	3.2984	8.1578	0.112	Ga(NO ₃) ₃
¹¹⁵ In	9/2	95.72	6.0892	5.8622	1.16	In(NO ₃) ₃

2.1.3 Description of NMR pulse sequences employed in this work

Single-Pulse MAS

A simple single-pulse NMR experiment is depicted in Figure 2-3.

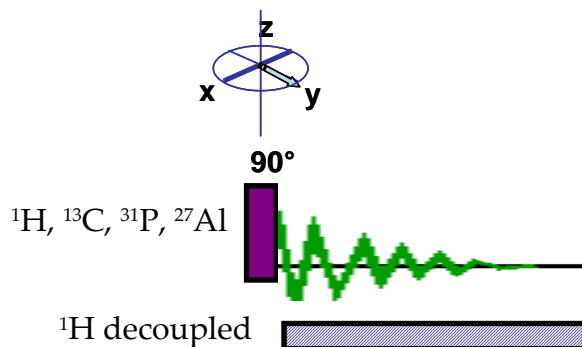


Figure 2-3. General pulse scheme for a single-pulse NMR experiment.

A 90° RF excitation pulse rotates the magnetization in the xy plane. After the termination of the pulse the nuclei relax towards equilibrium by exponential processes and yield by free induction decay (FID) the time-domain spectrum of

the sample, which upon Fourier transform provides the frequency domain spectrum.

Cross Polarization (CP) MAS

To enhance the signals from rare (dilute) nuclei such as ^{13}C , polarization is transferred from abundant nuclei (often ^1H nuclei). The process of CP occurs through the tendency of the magnetization to flow from highly polarized nuclei to nuclei with lower polarization, when the two are brought into contact. For homonuclear spins, the magnetization can be exchanged through mutual energy-conserving spin flips, while for heteronuclear pairs such as ^1H and ^{13}C , these spin flips are not energy-conserving at high magnetic fields and the exchange of magnetization must be driven externally by the application of RF fields. To create a dipolar contact between two spin systems the Hartmann-Hahn method is used in which two continuous RF fields are simultaneously applied at the respective resonance frequencies of the spin systems, Figure 2-4.

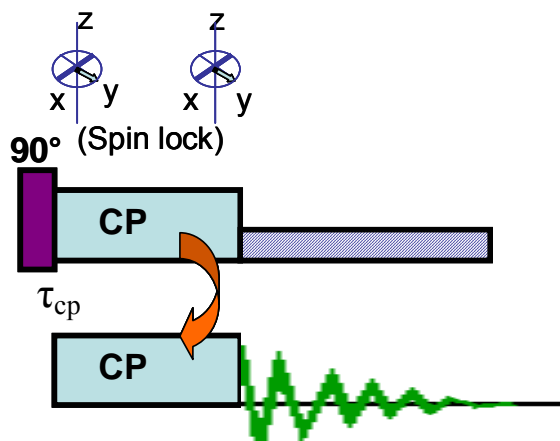


Figure 2-4. Pulse sequence for a CPMAS experiment.

The magnetization of the proton is brought into the xy plane by a $\pi/2$ pulse. RF fields are then applied to the spins for a period τ_{cp} , which causes the

magnetization to be exchanged between the spin systems. Finally, the signal from (e.g.) the ^{13}C spin system is detected while that from ^1H is decoupled. For long CP mixing times, the magnetization will be transported farther away, even to carbon atoms that are not directly bonded. Strongly coupled spins transfer polarization more rapidly than weakly coupled spins. Under CP conditions the sampling rates depend on the relaxation time of the nuclei from which the magnetization is transferred. As the protons in the solid state typically relax more rapidly than most other spin 1/2 nuclei, many more scans can be acquired in a given amount of time than in simple single-pulse experiments that detect the rare ^{13}C nucleus directly. While cross polarization for spin 1/2 nuclei is readily accomplished by matching the nutation frequencies of the two spin systems during the contact times, the spin dynamics of Hartmann-Hahn cross polarization change for quadrupolar nuclei.¹¹⁸

2D HETCOR MAS

The HETCOR experiments correlate the ^1H chemical shift with the chemical shifts of another nucleus, such as ^{13}C or ^{31}P . The ^1H magnetization is first excited by a $\pi/2$ pulse. During the t_1 period (homonuclear decoupling) the protons are decoupled from each other. Following the t_1 period the magnetization is transferred to the ^{13}C nuclei by CP and is then detected during t_2 , Figure 2-5. HETCOR relies on dipolar interactions and thus correlates spatially closely bonded and non-bonded nuclei.

In some of the experiments in the present work a frequency-switched Lee-Goldberg (FSLG) irradiation was employed during the proton evolution t_1 , to decouple the homonuclear dipolar interactions between the abundant protons.

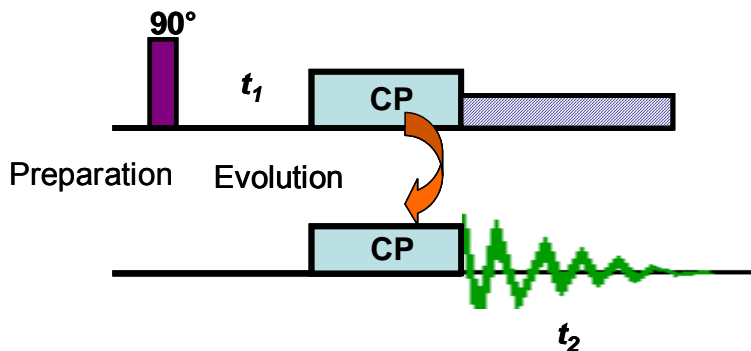


Figure 2-5. Pulse sequence for a 2D HETCOR experiment.

Spin-Echo MAS

Spin-echo experiments are a useful method to detect quadrupolar nuclei since the spin echo will refocus any time-independent variations in the resonance frequency, including field inhomogeneity, chemical shifts and heteronuclear spin couplings. The simplest RF pulse created echo is the two pulse sequence shown in Figure 2-6.

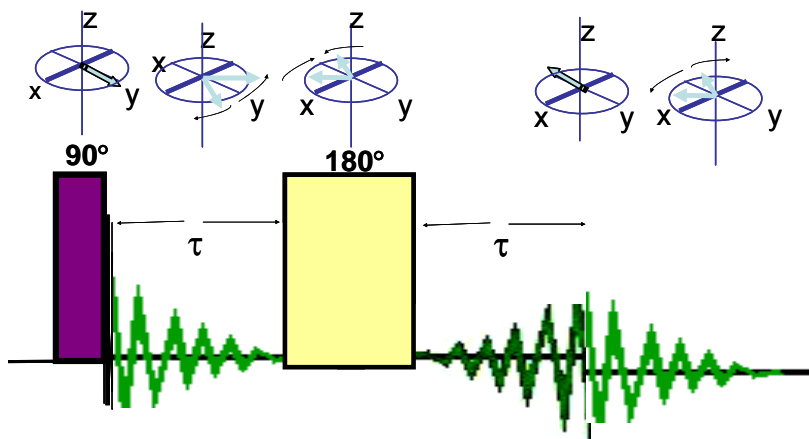


Figure 2-6. Spin-echo NMR pulse sequence.

The first 90° RF pulse rotates the magnetization from the z-axis into the transverse plane. The transverse magnetization begins to dephase and, after a

certain delay time τ , a 180° refocusing pulse is applied. This pulse rotates the magnetization by 180° about the x axis, which causes the magnetization to at least partially rephase and, after a second delay (of the same size as the first delay) a nuclear spin-echo can be detected at time 2τ .

2D Double-Quantum (DQ) MAS

Figure 2-7. presents a general scheme of 2D DQ NMR spectroscopy. During the DQ excitation period (τ_{exc}) and reconversion period rotor-synchronized pulse sequences are applied. The excitation part is phase-cycled in 90° steps to provide a double-quantum filter, while the reconversion period is 90° phase shifted from the excitation sequence but without phase cycling. The delay after the reconversion part (t_d) is included for the dephasing of spurious transverse magnetization.

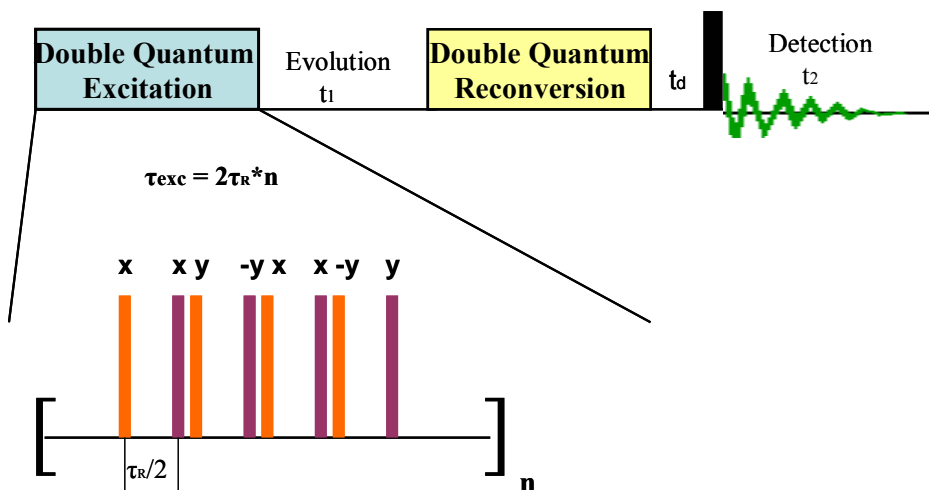


Figure 2-7. 2D DQ MAS NMR scheme with BABA pulse sequence.

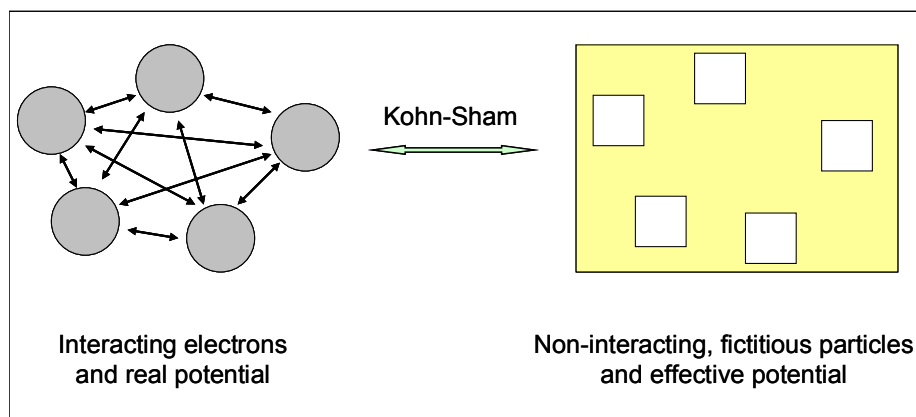
The pulse sequence used in this experiment involves back-to-back (BABA) 90° radio frequency pulse cycles acting on multiple (n) of two rotor periods ($2\tau_R$). A further improvement of the signal-to-noise ratio is achieved by sign inversion of

all pulse phases after two rotor periods for the compensation of radio frequency pulse imperfections.

2.2 Basics of Density Functional Theory (DFT)

Density functional theory has become the standard quantum mechanical method to investigate the electronic structure of many-body systems, in particular of molecules and the condensed phases. Traditional methods in electronic structure theory are based on the use of local one-particle potentials to describe the interaction of the electrons and the use of complicated many-electron wavefunction. The main objective of DFT is to replace the many-body interaction of electronic wavefunctions with an electronic density as a fictitious interaction potential. The approach of Kohn-Sham¹¹⁹ allows an exact description of the interacting many-particle systems in terms of an effective non-interacting particles system, Scheme 2-1. The effective potential in this non-interacting particle system (Kohn-Sham system) is determined by the electron density of the interacting system and therefore called a density functional.

DFT uses a functional that acts on the electronic properties of an atomic system to determine its energy. Hohenberg and Kohn¹²⁰ proved that for a non-degenerate quantum system there exists a functional that gives the ground state energy of a given configuration. If this functional is known, the ground state energies can be calculated using an iterative approach.

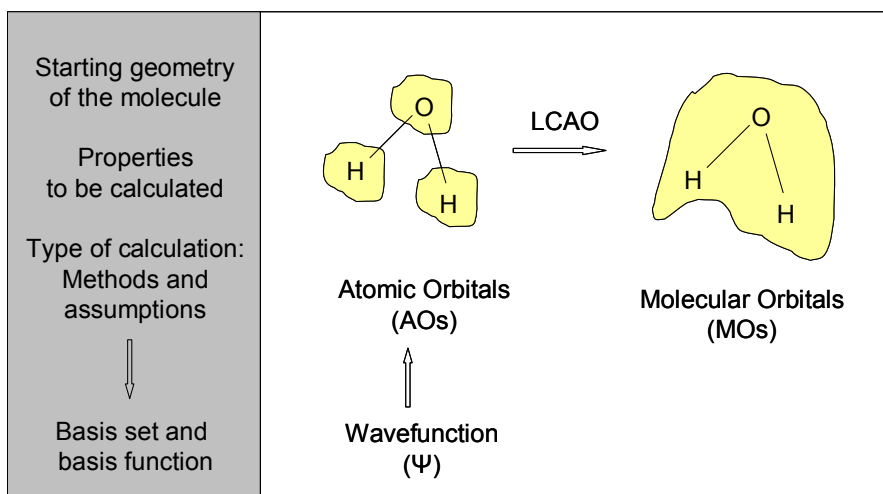


Scheme 2-1. Simplified illustration of Kohn-Sham approach to DFT.

The advantage of DFT is the fact that the electron density is a variable of only three spatial coordinates, whereas the wavefunction of an N -electron system has $3N$ variables. This results in an enormous improvement of computational speed. The theorem of Hohenberg and Kohn is a proof of the existence of such a density functional, and that the properties of a many-electron system are a functional of the density, but there is no prescription of how to derive it. It is necessary to use approximations regarding the parts of the function that deals with kinetic energy, exchange and correlation energies of the system of electrons. The energy of a conformation of the nuclei is calculated by performing a self-consistent iteration procedure of finding a density and evaluating the energy. The functional changes every step as it depends on the density itself. The new density can be found by several minimization schemes such as the method of the steepest descend. When the energy changes are below a given limit, this procedure is considered converged. The functionals used in the present work are the Becke exchange functional (B3) and the Perdew-Wang correlation functional, i.e. B3PW91.

Historically, the quantum calculations for molecules were performed as Linear Combination of Atomic Orbitals- Molecular Orbitals (LCAO MO), in which molecular orbitals are formed as a linear combination of atomic orbitals (Scheme 2-2.). Originally, Slater Type Orbitals (STO) were used as basis functions due to their similarity to atomic orbitals of the hydrogen atom. Because the necessary integrals over STOs cannot be performed very efficiently, Gaussian Type Orbitals (GTO), or primitives, were introduced to facilitate much faster calculations. They can approximate the shape of the atomic orbitals by means of a linear combination of GTOs with different exponents and coefficients.

For molecular calculations the Gaussian primitives are contracted by forming appropriate linear combinations which are then used as basis functions. Gaussian primitives and contractions are derived from Hartree-Fock calculations, and therefore may not be optimal for DFT methods where the electron density is somewhat more diffuse than in the Hartree-Fock description, particularly in the case of transition metals. A fully uncontracted basis set for the valence electrons of Re was therefore used in the present work.



Scheme 2-2. Simplified diagram for calculations of molecular orbitals.

For all atoms other than Re a 6-31G* basis set was used, as provided in the Gaussian03 software. In this nomenclature the number 6 refers to the use of 6 Gaussian functions summed to describe the inner shell orbitals, 3 being the number of Gaussian functions that comprise the first STO, and 1 refers to the number of Gaussian functions summed in the second STO. The asterisk denotes that additional d-type polarization functions are added (distorted shape of atomic orbitals caused by charge distribution) which are important for proper description of chemical bonding.

The inner (core) electrons on the transition metal are in generally not significantly affected by changes in the chemical bonding. They are therefore described by so-called Effective Core Potentials (ECP), which treat the inner shell electrons as if they were an averaged potential rather than individual particles. Relativistic effects can be easily incorporated into ECP. These arise from the fact that the effective mass of the electron increases as its speed approaches that of the speed of light, which in turn results in an effective reduction of the Bohr radius (relativistic contraction). These relativistic effects can be appreciable for heavier atoms, such as transition metals.

2.3 Basics of X-Ray Absorption Spectroscopy (XAFS)

Structural information on the active sites in catalysts as well as reactant and product complexes formed are crucial to an understanding of the origin of the catalytic activity of a particular system. In cases where the catalyst and support are not crystalline, i.e. do not possess a long-range ordered structure, only local

structural probes can be employed. Apart from NMR studies, it is the use of X-ray absorption spectroscopy that can provide the necessary information even on relatively complex systems as the one under study in this work. The manner in which this information can be extracted from this type of experiment is briefly described in the following sections.

The oscillating electric field of electromagnetic radiation, such as X-rays, will interact with the electrons bound in the atoms that compose a material struck by this radiation. As a result of this interaction the radiation will either be scattered by these electrons or absorbed. The intensity of an X-ray beam entering a material is attenuated exponentially, Equation 2-8.

$$I = I_0 e^{-\mu x} \quad (\text{eq. 2-8.})$$

where I represents the transmitted intensity, I_0 the initial intensity, x is the path length of the beam in the sample and μ the X-ray absorption co-efficient. The absorption coefficient varies with energy of the incident X-rays, i.e. μ decreases with increasing X-ray energy. If the energy of the incident photon is large enough to excite a core electron into an unoccupied higher level, or into the continuum, a sharp increase is observed in the absorption coefficient at this particular energy. The energies at which these processes occur are characteristic of the electronic structure of the electronic state of a given element. Experimental observation of the X-ray absorption spectrum (XAS) and its fine structure can therefore be used for atomic level characterization of materials that contain elements with experimentally accessible absorption spectra.

X-ray absorption spectra are produced over the range of 200 – 35,000 eV and are displayed as a graph of the absorption coefficient of a given material versus

energy. The complete XAS can be divided into four regions as shown in Figure 2-8. The pre-edge region, the X-ray absorption near edge structure (XANES), the near edge X-ray absorption fine structure (NEXAFS) in the region between 10 eV up to 50 eV above the edge, and the extended x-ray absorption fine structure (EXAFS) region which starts approximately from 50 eV to 1,000 eV above the edge.^{121 122} XANES and NEXAFS are, however, frequently taken to be synonymous.

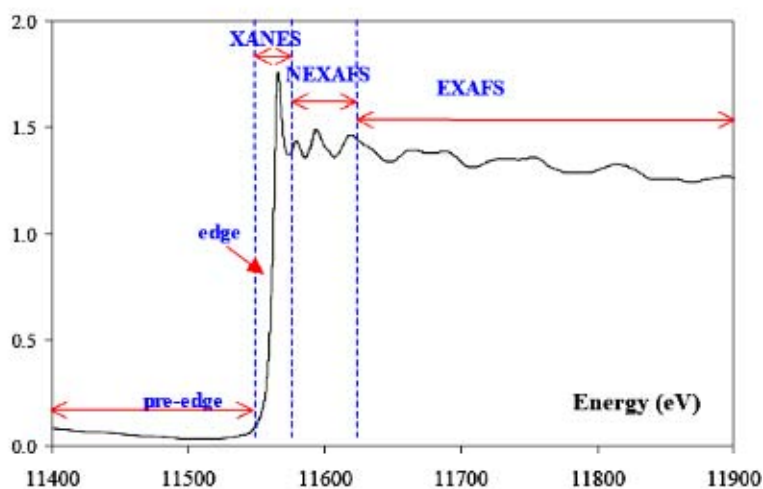


Figure 2-8. Representative generic XAS spectrum with the different energy regions.

Minor features observed in the pre-edge region usually have their origin in electron transitions from the core level to the higher unfilled or half-filled valence orbitals. The XANES region includes the actual absorption edge and consists of transitions of core electrons to vacant non-bound levels close to the Fermi energy. Because of the high probability of such transition, a strong rise in the absorption is observed. There is now enough energy provided to the electron to cause ionisation and eject a photoelectron. In NEXAFS, the ejected photoelectrons have low kinetic energy and experience strong multiple scattering by the first or even higher coordination shell. In the EXAFS region, the

photoelectrons have high kinetic energy and single scattering by the nearest neighbouring atoms usually dominates.

The dominant physical process in EXAFS is one where the absorbed photon ejects a core photoelectron from the absorbing atom, which leaves behind an excited atom with a core hole. For this to occur the energy of the incident X-rays must surpass the ionization threshold (the edge energy). Below the absorption edge, the photons cannot excite the electrons of the relevant atomic level and thus absorption is low. However, when the photon energy is just sufficient to excite the electrons, a large increase in absorption occurs (absorption edge). The energies of the absorbed radiation at these edges correspond to the binding energies of electrons in the K, L, M, etc. shells of the absorbing elements. The ejected photoelectron's energy will be equal to that of the absorbed photon minus the binding energy of the initial core state.

The ejected photoelectrons interact with and scatter from electrons in the surrounding non-excited atoms. Backscattered electron waves interfere with the forward-propagating waves and give rise to an interference pattern, which appears as a modulation of the measured absorption coefficient, i.e. the oscillations in the EXAFS spectrum, Figure 2-9. The detailed form of these oscillations contain information on the atomic number, interatomic distances and the coordination number of the atoms surrounding the element whose absorption edge is being examined, i.e., the *local* structure around the absorbing atom. The wavelength of the photoelectron is dependent on the energy and phase of the backscattered wave which exists at the central atom.

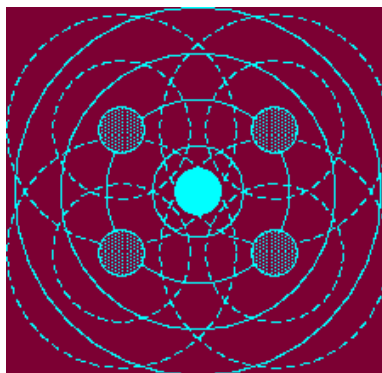


Figure 2-9. Interference of the photoelectron wave (solid lines) created by the absorption process being backscattered by the neighbouring atoms (dotted lines).

The probability of backscattering is dependent on the energy of the photoelectrons. The phase and amplitude of the backscattered wave depend on the type of atom doing the backscattering and the distance of the backscattering atom from the central atom. The dependence of the scattering on atomic species makes it possible to obtain information pertaining to the chemical and structural coordination environment of the absorbing (centrally excited) atom from analysis of these EXAFS data.

2.4 Experimental details

2.4.1 Catalyst materials, synthesis procedures and instrument settings

Silica-alumina, silica and zeolite HY. Amorphous silica-alumina, Davicat 3113 (7.6 wt.% Al, BET surface area 573 m²/g, pore volume 0.76 cm³/g), was provided by Grace-Davison (Columbia, MD). Nonporous, fumed silica Aerosil 380 (BET

surface area 340 m²/g, average particle size 7 nm) was provided by Degussa (Piscataway, NY). The zeolite HY powder CBV 400 (SiO₂/Al₂O₃ 5.1, surface area 730 m²/g, unit cell 24.5 Å) was purchased from Zeolyst International (Valley Forge, PA). Mesoporous aluminosilicates Al-MCM41 (Si/Al=7, surface area 1070 m²/g) and Al-SBA16 (Si/Al=14, surface area 555 m²/g) were prepared according to literature procedures.¹²³⁻¹²⁵

In each experiment, the appropriate amount of support was first outgassed in a Pyrex reactor for 4 h at 450 °C under dynamic vacuum ($\leq 10^{-4}$ Torr), then calcined for 12 h under 350 Torr static O₂ at the same temperature, and allowed to cool to room temperature under dynamic vacuum. The choice of 450 °C was dictated by the minimum temperature required to remove adsorbed water, hydrocarbon impurities and surface carbonates during the calcination step. The resulting material will be referred to as “dehydrated”, since spectroscopic signals characteristic of adsorbed water (IR: 1640 cm⁻¹; ¹H MAS NMR: 6.4 ppm)¹²⁶ disappear when silica-alumina is treated under vacuum at temperatures above 340 °C.¹²⁷ They were subsequently handled with strict exclusion of air at all times. Hexamethyldisilazane (HMDS, Aldrich, >99.5%) was subjected to multiple freeze-pump-thaw cycles to remove dissolved gases, then stored under vacuum over P₂O₅ in a glass reactor. For the preparation of capped silica-alumina HMDS was transferred via the vapor phase under reduced pressure onto the dehydrated support, until there was no further uptake (as judged by stabilization of the pressure). The reactor was then evacuated and the solid was heated to 350 °C for 4 h under dynamic vacuum to remove unreacted HMDS as well as ammonia produced during the silanol capping reaction.

Methyltrioxorhenium. CH_3ReO_3 , a polycrystalline, colorless solid, was purchased from Aldrich and used as received. Volatile CH_3ReO_3 was sublimed at 10^{-4} Torr and room temperature into a reactor containing dehydrated support, while the solid was shaken vigorously to promote its uniform exposure to the volatile organometallic complex and thus macroscopic sample homogeneity. At loadings higher than 1 wt.% Re, the white silica-alumina acquired a distinctly yellow-brown color that was stable under room light, but bleached rapidly upon exposure to air.



Image 2-1. Photos of (a) MeReO_3 , (b) silica-alumina, (c) MeReO_3 grafted onto uncalcined silica-alumina and (d) MeReO_3 grafted onto calcined silica-alumina.

Physisorbed material was generally recovered by subsequent desorption (ca. 12 h) to a liquid N_2 trap at room temperature under vacuum. This step was omitted for samples with low Re loadings (far below the maximum uptake by chemisorption, ca. 10 wt.% Re on Davicat 3113) and for the silica support (since CH_3ReO_3 desorbs completely from silica under these conditions). Where noted, desorption from silica-alumina was performed at 80°C , by heating the material under vacuum and collecting volatile CH_3ReO_3 in a liquid N_2 -cooled receiving flask. In order to minimize materials transfers and ensure sample integrity, a new batch of the highly air-sensitive grafted CH_3ReO_3 was made for each measurement (with the exception of sequential NMR experiments); therefore, the weight loading varied from sample to sample (typically 1-2 wt.%).

Labeled CD_3ReO_3 (>99% D) and $^{13}\text{CH}_3\text{ReO}_3$ (>99% ^{13}C) were prepared from $^{13}\text{CH}_3\text{SnBu}_3$, respectively, according to literature procedures^{17, 128} in an effort to resolve signals in ^1H solid state NMR and to enhance sensitivity in ^{13}C solid state NMR experiments.

Rhenium analysis. Re loadings were determined by quantitative extraction, followed by UV spectrophotometric analysis. Approximately 15 mg of solid material was first weighed precisely in a dry N_2 atmosphere. Re was then extracted quantitatively as perrhenate by stirring overnight in air with 5 mL 3 M NaOH. Samples were diluted to 25 mL with 3 M H_2SO_4 , filtered, and their UV spectra recorded on a Shimadzu UV2401PC spectrophotometer. The Re concentration was determined at 224 nm, using a calibration curve prepared with NH_4ReO_4 (Aldrich).

Solution NMR. All solution NMR experiments were performed at room temperature on a Bruker AVANCE 200 spectrometer with a 10-mm broadband probehead, operating at 200.1012 MHz for ^1H and 50.3202 MHz for ^{13}C . Chloroform-d (99.8% D) and benzene-d₆ (99.5% D) were purchased from Cambridge Isotopes Laboratories, Inc. (Andover, MA).

Solid state NMR. All solid state NMR experiments were performed on a Bruker AVANCE 300 NMR spectrometer with a 4-mm broadband MAS probehead operating at 300.1010 MHz for ^1H , 75.4577 MHz for ^{13}C and 78.2067 MHz for ^{27}Al . This instrument is equipped with a variable temperature unit. The highly air-sensitive samples were packed into zirconia MAS rotors with tightly fitting caps sealed with Viton R O-rings (Wilmad) under an argon atmosphere in a glovebox equipped with O_2 - and moisture-sensors. Room temperature MAS spectra were

acquired at spinning speeds of 12 or 30 kHz. Low-temperature MAS experiments were recorded while spinning at 8 kHz.

Single-pulse ^1H MAS experiments were performed with a 90° pulse length of 3.7 μs , an acquisition time of 25 ms and a recycle delay of 3 s. For quantitative ^1H MAS NMR, 60 mg dehydrated silica-alumina was weighed in an atmosphere of dry N_2 . A small piece of poly(dimethylsiloxane) (PDMS, ca. 1 mg, weighed to within ± 0.05 mg) was used as an internal standard for quantifying ^1H NMR signal intensities. PDMS was chosen because it exhibits a single signal with an isotropic ^1H chemical shift of -0.1 ppm (relative to TMS) that does not overlap with the signals of interest.¹²⁹ Spectra were deconvoluted using the program DMFIT, to obtain Gaussian fits to spectral line shapes.¹³⁰

^{13}C CP spectra were recorded using a ^{13}C 90° pulse length of 3.5 μs , a contact time of 3 ms or 12 ms, an acquisition time of 21 ms and a recycle delay of 2 s. For single-pulse ^{13}C MAS experiments, a ^{13}C 90° pulse length of 3.5 μs , an acquisition time of 25 ms and a recycle delay of 15 s were used. ^1H and ^{13}C chemical shifts were referenced to tetramethylsilane (TMS). The same experimental conditions were used in the two-dimensional $^{13}\text{C}\{^1\text{H}\}$ HETeronuclear chemical shift CORrelation (HETCOR) experiments. For each of the 256 t_1 increments, 128 data acquisitions were collected with a 2 s recycle delay. During the detection period t_2 , 1024 points were collected with a dwell time of 20 μs . The outer contour levels are drawn at 45% of the maximum intensity. No additional correlations were found using lower 2D threshold levels.

The same experimental settings were used for spectra recorded sequentially under MAS/static conditions or at room temperature/-100 $^\circ\text{C}$. However, in low

temperature experiments, dry nitrogen was used as the spin gas instead of air.

Single-pulse ^{27}Al MAS experiments were performed with a 90° pulse length of 3.8 μs , an acquisition time of 4.1 ms and a recycle delay of 15 s. Chemical shifts were referenced to an aqueous solution of $\text{Al}(\text{NO}_3)_3$ as an external standard. A small piece of dense AlN (2.3 mg, containing 0.057 mmol Al) was used as an internal “spin-counting” standard to quantify ^{27}Al MAS signal intensities. AlN was chosen because its isotropic signal at 113 ppm does not overlap with the ^{27}Al signals of interest, and a spinning speed of 14 kHz was used to avoid overlap with the ^{27}AlN spinning sidebands. A recycle delay of 15 s was used to allow for the long spin-lattice relaxation time of polycrystalline AlN .¹³¹ 16,000 scans were acquired for each ^{27}Al spectrum, which were subsequently deconvoluted with DMFIT, using Gaussian fits and including spinning sidebands for comparison of integrated ^{27}Al peak areas.¹³⁰

Infrared spectroscopy. The IR experiments were performed in a Pyrex cell equipped with KCl windows affixed with TorrSeal (Varian). Its high-vacuum ground-glass stopcock and joints were lubricated with Apiezon H grease (Varian). A self-supporting pellet of silica-alumina was prepared in air by pressing ca. 25 mg of the solid at 40 kg/cm^2 in a 16 mm stainless steel die, and was transferred to a Pyrex pellet holder. Sublimation of CH_3ReO_3 via a vacuum manifold directly onto a calcined, dehydrated silica-alumina pellet in the presence of TorrSeal led to unwanted side-reactions of the latter with the organometallic complex. Instead, the pellet was calcined and dehydrated in an all-glass Schlenk tube, exposed to CH_3ReO_3 by sublimation, then transferred to the IR cell under argon in a glovebox. IR spectra of the self-supporting pellet were recorded *in vacuo* in transmission mode on a Shimadzu PrestigeIR

spectrophotometer equipped with a DTGS detector, and purged with CO₂-free dry air from a Balston 75-52 Purge Gas Generator. Background and sample spectra were recorded by adding 64 scans together at a resolution of 4 cm⁻¹.

Kinetics and selectivity of propylene metathesis. A precisely weighed amount (10.0 mg) of each catalyst was loaded into a glass batch reactor (volume ca. 120 mL) in an Ar-filled glovebox. The reactor was removed from the glovebox and evacuated. The section of the reactor containing the catalyst was immersed in an ice bath at 0 °C in order to control the rate of the reaction on a readily-monitored timescale, as well as to maintain isothermal reaction conditions. Propylene was introduced at the desired pressure via a high vacuum manifold. Aliquots of 1.9 mL were expanded at timed intervals into an evacuated septum port that was separated from the reactor by a stopcock. 50 µL samples of the aliquot were removed with a gas-tight syringe via a septum. Gases were analyzed by FID on a Shimadzu GC 2010 equipped with a 30 m Supelco® Alumina Sulfate PLOT capillary column (0.32 mm i.d.). Quantification was achieved using the peak area of the small propane contaminant present in the propene as an internal standard.

Density functional theory calculations. Computations were performed on an Intel Xeon computer running Linux, as well as the VRANA-5 and VRANA-8 clusters at the Center for Molecular Modeling of the National Institute of Chemistry (Ljubljana, Slovenia), using the DFT implementation in the Gaussian03 code, Revision C.02.¹³² The orbitals were described by a mixed basis set. A fully uncontracted basis set from LANL2DZ was used for the valence electrons of Re,¹³³ augmented by two f functions ($\zeta = 1.14$ and 0.4) in the full optimization. Re core electrons were treated by the Hay-Wadt relativistic effective core potential (ECP) given by the standard LANL2 parameter set

(electron-electron and nucleus-electron). The 6-31G* basis set was used to describe the rest of the system. It is well-established for use with organic molecules and has also been shown to reproduce experimentally-determined aluminosilicate structures.¹³⁴ The B3PW91 density functional was used in all calculations. For reactions involving hydrogen bonds, additional calculations were performed using the larger basis set 6-31+G**, to verify binding energies and obtain improved H-bond geometries.

EXAFS analysis and curve fitting. Acquisition of XAFS spectra requires the use of a tuneable X-ray source, which is normally that of an electron or positron synchrotron. Spectra for this work were recorded at the Re L_{III} edge (10,535 eV) at the Stanford Synchrotron Radiation Laboratory on beamline 2-3 (bend), operating at 3.0 GeV with a current of 75-100 mA. X-rays were monochromatized via reflection from a pair of Si(111) crystals through a 1 mm entrance slit.

The incident beam was detuned 30% to suppress harmonics. Samples were mounted at a 45° angle to the beam in order to collect transmission and fluorescence spectra simultaneously. The intensity of the incident beam was measured with a N₂-filled ion chamber detector installed in front of the sample. Transmitted X-rays were detected in a second, N₂-filled ion chamber. Fluorescence from the sample was recorded at right angles to the beam by an Ar-filled Lytle detector installed without Soller slits.

Powder samples were packed in 35 × 5 × 2 mm slots in aluminum sample plates with windows of 12.0 μm polypropylene film (Chemplex #475) affixed with double-sided tape to each side of the plate. This sample preparation technique has been shown to prevent even highly air-sensitive samples from

decomposing.¹³⁵ To avoid spectral artifacts due to sample thickness,¹³⁶ the sample of polycrystalline CH_3ReO_3 was diluted to ca. 3 wt.% Re by mixing the solid with powdered boron nitride (Strem) in air. Highly air-sensitive CH_3ReO_3 /silica-alumina was packed, without dilution, into the sample plate under N_2 . A single data sweep (collection time ~20 min) was sufficient to obtain a good signal-to-noise ratio in the fluorescence channel. Subsequent data sweeps showed no change due to sample decomposition. Fluorescence data generally showed better signal-to-noise ratios and were used in subsequent data analyses instead of transmission data.

EXAFS data fitting can be either performed in k -space (reciprocal) or R -space (real, Fourier transformed). The Fourier transformation of χ (eq. 2-9.) gives a quantity related to the pair distribution function which describes the coordination geometry about the EXAFS atom. In this work EXAFS spectra were analyzed in k -space using WinXAS v.3.1.¹³⁷ The data were first background-corrected, then normalized by a 3rd degree polynomial fitted to the post-edge region. EXAFS spectra were k -weighted and fitted with a polynomial spline. A Kaiser-Bessel window function ($\alpha = 4$) was applied to the data range prior to Fourier transformation, to minimize spectral ringing. Only single-scattering paths in the EXAFS equation, Equation 2-9., were fitted to the k -space spectra with least-squares refinement.¹³⁸

$$\chi(k) = S_0^2 \sum_i \frac{N_i F_i(k)}{k R_i^2} \exp(-2k^2 \sigma_i^2) \exp\left(\frac{-2R_i}{\lambda(k)}\right) \sin(2kR_i + \phi_i(k)) \quad (\text{eq. 2-9.})$$

where N_i is the number of scatterers in the i^{th} shell at a distance R from the absorber. The Debye-Waller factor, σ_i^2 , is the root-mean-squared relative

displacement of the scatterer, $\lambda(k)$ is the mean-free path of the photoelectron and $\phi(k)$ and $F(k)$ are its phase shift and backscattering amplitude, respectively. The phase-shift and backscattering amplitude functions were calculated using FEFF 8.20.¹³⁹ Since curve-fitting was performed using *a priori* electronic calculations, no reference spectra were needed or used in the EXAFS analysis.

The EXAFS equation has a large number of degrees of freedom, and some of its parameters are strongly correlated. Parameters were varied sequentially during curve fitting. Since each model involves a well-defined organometallic complex as its starting point, coordination numbers were initially fixed at their corresponding integer values. Path lengths and Debye-Waller factors were then allowed to vary sequentially, while S_0^2 and ΔE_0 were held fixed, until the residual changed by <1%. The fitted values were then fixed, while S_0^2 and ΔE_0 were sequentially refined. Goodness-of-fit was evaluated via the magnitude of the residual, defined as $\Sigma(y_{\text{obs}}(i)-y_{\text{fit}}(i))/\Sigma y_{\text{obs}}(i)$ where $y_{\text{obs}}(i)$ and $y_{\text{fit}}(i)$ are the observed and calculated values of each (unweighted) data point in k -space, as well as the appropriateness of the fit parameters (path lengths, Debye-Waller factors). The total number of independent fitted parameters may not exceed N_{idp} , given by Equation 2-10.¹⁴⁰

$$N_{idp} = \frac{2\Delta k \Delta R}{\pi} \quad (\text{eq.2-10.})$$

where Δk and ΔR are the ranges over which the data are substantial (i.e., containing features distinguishable from the noise) in k -space and R -space, respectively.^{141 142}

2.4.2 Nanoparticle synthesis procedures and instrument settings

Synthesis of InGaP nanoparticles (unetched). All chemicals were purchased from Aldrich. $\text{In}_{1-x}\text{Ga}_x\text{P}$ nanoparticles with 9% Ga inclusion (as-synthesized, $x=0.09$) were prepared as described previously.^{65, 84, 90} Briefly, 0.3826 g (1.31 mmol) indium(III) acetate and 0.0481 g (0.131 mmol) gallium(III) acetylacetonate, were degassed at 120 °C in 45.5 g *n*-hexadecylamine (HDA) for approximately 30 min. $\text{P}(\text{Si}(\text{CH}_3)_3)_3$ (0.63 M, 2.17 mmol) was injected via syringe at 120 °C under an argon atmosphere, and the temperature was ramped to 280 °C over ~7 h. The reaction proceeded for ~8 h, while the size and dispersity were monitored by removing aliquots and performing UV-VIS absorbance spectroscopy in dilute solutions of toluene. The reaction was quenched by cooling to 60 °C, followed by collection of the nanoparticles via the addition of approximately 100 mL of dry methanol and centrifugation. The nanoparticles were purified by dissolution in a minimum amount of dry toluene, re-precipitation by addition of dry methanol, and centrifugation under argon (3x), and dried under a flow of argon overnight. The unetched HDA-passivated $\text{In}_{1-x}\text{Ga}_x\text{P}$ particles were spherical with mean diameters of 4.5 nm \pm 0.2 nm and x measured to be 0.09 for Ga (verified independently for In) by using Atomic Emission-Inductively Coupled Plasma (AE-ICP) spectroscopy.

HF etching of InGaP nanoparticles. $\text{In}_{1-x}\text{Ga}_x\text{P}$ nanoparticles with strong photoluminescence properties were prepared by treatment with hydrofluoric acid. 10 mg of the un-dried $\text{In}_{0.91}\text{Ga}_{0.09}\text{P}$ nanoparticles from the above reaction were first dissolved in ~35 mL of toluene under ambient conditions. The dilute conditions were necessary to ensure more uniform etching of the particles under low power (ca. 100 mW) near-UV (365 nm) irradiation. To maintain solubility

during etching, hexadecanoic acid (~200 mg) was added, and the mixture was sonicated to produce an optically clear solution. Etching was carried out in an aerated solution by the addition of ~30 μL of a 5% HF solution in methanol and excitation using a low-power 365-nm fluorescent hand lamp for ~3 min, followed by precipitation with methanol and centrifugation. The isolated, etched InGaP nanoparticles were purified by dissolution in a minimum amount of toluene, reprecipitated by addition of methanol, centrifuged under argon (3x), and the solid precipitate dried overnight under Ar. The HF-etched $\text{In}_{1-y}\text{Ga}_y\text{P}$ nanoparticles were spherical-like with a mean size of 4.0 nm and y measured to be 0.06 for Ga (verified independently for In) by AE-ICP.

Optical measurements. The expression used to determine the quantum efficiencies of the as-synthesized $\text{In}_{0.91}\text{Ga}_{0.09}\text{P}$ and HF-treated $\text{In}_{0.94}\text{Ga}_{0.06}\text{P}$ nanoparticles in toluene is given by Equation 2-11.⁹⁰

$$\phi_{em} = \phi'_{em} (I / I') (A' / A) (n / n') \quad (\text{eq. 2-11.})$$

where I (sample, InGaP nanoparticles in toluene) and I' (reference, rhodamine 6G in ethanol) are integrated emission peak areas, A (sample) and A' (reference) are the absorbances at the excitation wavelength (460 nm), n (sample) and n' (reference) are the refractive indices of the solvents, and ϕ'_{em} is the quantum efficiency of the reference. Rhodamine 6G was purchased from Exciton, Inc. (Dayton, Ohio, USA). The toluene and ethanol solvents were spectroscopic grade (UHP). The 10 x 10 mm and 10 x 4 mm quartz fluorescence cells were purchased from Starna (Atascadero, California, UCS). The solutions were prepared and studied under ambient conditions without degassing.

Transmission electron microscopy. A drop of nanoparticles in toluene was directly placed on a copper grid. Images were taken on a JEOL 2010 high resolution microscope.

Solid state NMR experiments. ^{31}P MAS NMR experiments were performed at room temperature on a Bruker 300 MHz Avance spectrometer with a 4-mm broadband MAS probe tuned to 121.5 MHz and 300 MHz for ^{31}P and ^1H , respectively. A spinning speed of 12 kHz was used in all experiments and the chemical shifts of ^{31}P and ^1H were referenced to 85% H_3PO_4 and TMS, respectively.

The ^{31}P single-pulse MAS experiments were performed with an acquisition time of 2.1 ms, a recycling delay of 30 s, and a 90° pulse of 2.75 μs . The ^{31}P CPMAS experiments were acquired using TPPM (Two Pulse Phase Modulation) ^1H decoupling, ramped cross-polarization, an acquisition time of 2.1 ms, a recycle delay of 3 s, contact time ranging from 0.1 to 20 ms, and a ^1H 90° pulse length of 5.25 μs . The 2D $^{31}\text{P}\{^1\text{H}\}$ HETCOR experiments were performed with a frequency-switched Lee-Goldberg (FSLG)¹⁴³ irradiation of 85 kHz applied to the ^1H spins during the t_1 evolution period, ramp CP during mixing, a TPPM ^1H decoupling during the data acquisition of 2.1 ms, a recycling delay of 1 s, and a ^1H 90° pulse length of 3 μs .

The 2D $^{31}\text{P}\{^{31}\text{P}\}$ double quantum MAS NMR experiments were acquired using a rotor-synchronized BABA pulse sequence¹⁴⁴ with an excitation time of 1.66 ms to reintroduce dipole-dipole couplings. The $\pi/2$ radio frequency pulses were set to a length of 4 μs . TPPM decoupling was applied during the acquisition and the dipole-dipole recoupling periods and States-TPPI (Time Proportional Phase

Incrementation) was used in t_1 for phase sensitive detection. Long T_1 relaxation times were circumvented by cross polarization of ^1H magnetization to nearby ^{31}P surface sites so that a recycle delay of 1 s was sufficient. The ^1H radio frequency field of the CP was ramped between 80 and 100% of its maximum value.

Solid state ^{71}Ga and ^{115}In MAS NMR spectroscopy experiments were performed on powder InGaP nanoparticle samples at room temperature on a Bruker 500 MHz AVANCE spectrometer operating at 152.7 MHz for ^{71}Ga and for 109.6 MHz ^{115}In . All MAS experiments were performed with a 4-mm broadband MAS probehead using a spinning rate of 14 kHz. The ^{71}Ga and ^{115}In signals were referenced to those from 1 M aqueous solutions of $\text{Ga}(\text{NO}_3)_3$ and $\text{In}(\text{NO}_3)_3$, respectively.

Spin-echo ^{71}Ga MAS NMR experiments were performed with an acquisition time of 4.2 ms, a recycle delay of 2 s, and 90° and 180° pulses of 1.6 μs and 3.2 μs , respectively. The ^{71}Ga MAS spectra of the InGaP nanoparticles before and after HF-etching were acquired with 216,100 transients from 75 mg of the as-synthesized nanoparticles and with 81,100 transients from 64 mg of the etched nanoparticles, respectively.

Spin-echo ^{115}In MAS NMR experiments were performed with an acquisition time of 1.7 ms, a recycle delay of 1 s, and 90° and 180° pulses of 0.64 μs and 1.28 μs , respectively. The ^{115}In MAS spectra of the InGaP nanoparticles before and after HF etching were acquired with 128,000 transients from 75 mg of the as-synthesized nanoparticles and with 96,640 transients from 64 mg of the etched nanoparticles, respectively. The same as-synthesized and etched samples were used for the respective ^{71}Ga and ^{115}In MAS experiments.

Chapter 3

Results and Discussion

Heterogeneous Re Catalysts for Olefin Metathesis

3.1 NMR and EXAFS investigations on molecular CH_3ReO_3

NMR spectroscopy of non-grafted CH_3ReO_3 . The dispersion of adsorbed CH_3ReO_3 on high surface area oxide supports may be characterized with reference to the spectral differences observed in the solvated and polycrystalline forms of CH_3ReO_3 . The ^1H and ^{13}C NMR chemical shifts differ widely for CH_3ReO_3 dissolved in various non-coordinating solvents, and in the polycrystalline material.^{145, 146} For example, the ^1H chemical shift of CH_3ReO_3 in polar CDCl_3 is 2.64 ppm (4.5 Hz fwhm), compared to 1.25 ppm in non-polar C_6D_6 . The ^1H MAS spectrum of the polycrystalline material shows an even greater downfield shift, to 3.7 ppm, Figure 3-1a. Its linewidth decreases from 3.8 to 2.1 kHz when the spinning speed is increased from 12 to 30 kHz, consistent with line broadening due to homonuclear dipole-dipole coupling.

The ^{13}C spectrum of CH_3ReO_3 in CDCl_3 consists of a signal at 19.6 ppm (31 Hz fwhm), compared to 18.1 ppm in C_6D_6 . The ^{13}C CPMAS spectrum of polycrystalline CH_3ReO_3 , on the other hand, has a peak with maximum at 34 ppm, Figure 3-1b, although the isotropic chemical shift is not revealed due to the complex lineshape. This lineshape may be a consequence of intermolecular interactions in the crystal lattice with multiple adjacent quadrupolar Re nuclei ($I=5/2$, $Q(^{187}\text{Re})= 2.2$ barn), which are incompletely averaged by magic angle spinning.

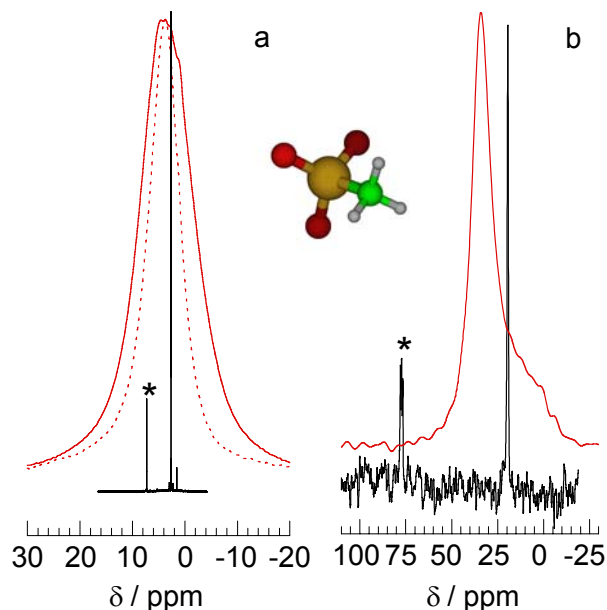


Figure 3-1. NMR spectra of CH_3ReO_3 : (a) ^1H MAS NMR spectrum for polycrystalline CH_3ReO_3 (12 kHz MAS: solid red line; 30 kHz MAS: dashed red line) and ^1H NMR spectrum of CH_3ReO_3 in CDCl_3 (black); (b) ^{13}C CPMAS NMR spectrum for polycrystalline CH_3ReO_3 (12 kHz MAS, red) and ^{13}C NMR spectrum of CH_3ReO_3 in CDCl_3 (black). * denotes solvent.

EXAFS results on solid CH_3ReO_3 . The XAS spectrum of polycrystalline CH_3ReO_3 (3 wt.% in BN) recorded at the Re L_{III} edge is shown in Figure 3-2. Structural parameters were confirmed by curve-fitting the EXAFS spectrum, using literature values for its bond distances¹⁴⁷ as the starting point for the analysis. EXAFS fit parameters for polycrystalline CH_3ReO_3 are compared to reported values for molecular CH_3ReO_3 in Table 3-1. The close agreement between structural parameters derived from electron diffraction and EXAFS curve-fitting lends confidence to the method used of EXAFS data analysis. The magnitudes of the fitted Debye-Waller factors confirm that polycrystalline CH_3ReO_3 contains a single site as far as the coordination environment of Re is concerned, and are of the same order of magnitude as those reported for other well-defined, single-site materials (ca. $1\text{-}3 \times 10^{-3} \text{ \AA}^2$) as calculated using the vibrational force constants for each single-scattering path.^{148, 149}

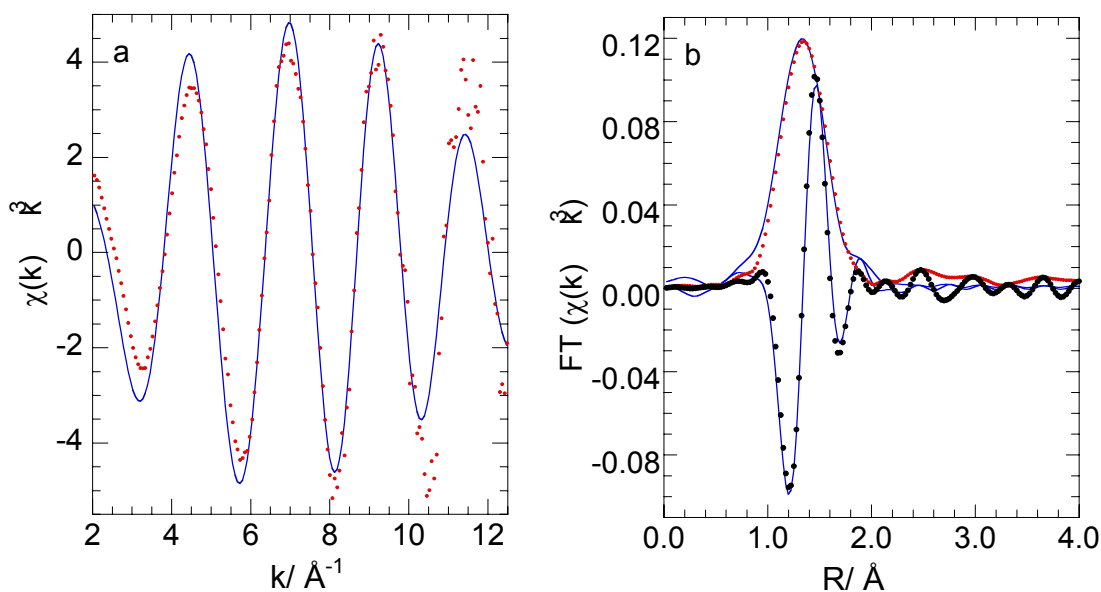


Figure 3-2. EXAFS data in (a) k^3 -weighted k -space (red points) and (b) non-phase-corrected R -space (imaginary, black points and FT magnitude, red points), for polycrystalline CH_3ReO_3 diluted in BN (3 wt.% Re). Parameters for the curve-fit (blue lines) are given in Table 3-1.

Table 3-1. Comparison of bond distances (\AA) reported for CH_3ReO_3

path	N	EXAFS curve-fit ^a	DFT calculation ^b	gas phase electron diffraction ¹⁴⁷	neutron powder diffraction ¹⁵⁰
Re=O	3	1.71 (0.0032)	1.703	1.709	1.702, 1.702, 1.709
Re-C	1	2.11 (0.0028)	2.076	2.060	2.063

^a This work, for polycrystalline CH_3ReO_3 diluted to 3 wt.% Re in BN. Coordination numbers were held fixed at integer values; Debye-Waller factors σ^2 (\AA^2) are shown in parentheses. $S_0^2 = 0.98$; $\Delta E_0 = 0.8$ eV; residual = 21.; ^b Isolated molecule (see text).

After optimization of path lengths and Debye-Waller factors, the global amplitude reduction factor S_0^2 and the inner potential energies ΔE_0 were allowed to vary from their initial values of 1.0 and 0.0, respectively. The fit returned values of 0.98 and 0.80 eV, respectively, and improved the goodness-of-fit only slightly, causing the residual to decrease from 24 to 21. Path lengths and corresponding Debye-Waller factors were unchanged.

3.2 Grafted CH_3ReO_3 on silica-alumina: low loadings

Methyltrioxorhenium can be deposited (10^{-4} Torr and room temperature) onto dehydrated amorphous silica-alumina (7.6 wt.% Al) in amounts as high as 10 wt.% Re of CH_3ReO_3 without subsequent loss of CH_3ReO_3 during prolonged evacuation at room temperature ($\leq 10^{-4}$ Torr). However, in an effort to maintain structural uniformity of the grafted sites on the amorphous silica-alumina support the loading of CH_3ReO_3 was kept much lower (≤ 2.3 wt.% Re) in the initial experiments. The grafting sites become less uniform at higher loadings and complexity arises in the NMR spectra, which will be described in section 3.3.

Infrared spectroscopy. The IR spectrum confirms that the methyl group remains intact upon grafting: $\nu_{\text{as}}(\text{CH}_3)$ and $\nu_{\text{s}}(\text{CH}_3)$ modes appear at 2993 and 2907 cm^{-1} , respectively, Figure 3-3., while $\delta_{\text{as}}(\text{CH}_3)$ appears at 1370 cm^{-1} . Both the frequencies and the relative intensities of the stretching modes differ from those observed in the spectrum of polycrystalline CH_3ReO_3 (2989 and 2900 cm^{-1}),¹⁵¹ which suggests that the symmetry at Re changes as a result of adsorption.

1D and 2D ^{13}C MAS NMR spectroscopy. The sensitivity of the NMR chemical shifts to local structure in grafted metal complexes can be utilized to obtain information on the environment of the methyl group in the adsorbed organorhenium complex. The ^{13}C CPMAS spectrum of $^{13}\text{CH}_3\text{ReO}_3$ grafted onto dehydrated silica-alumina (0.4 wt.% Re) consists of a single isotropic signal at 29 ppm (460 Hz fwhm), Figure 3-4a. This chemical shift is consistent with retention of the methyl group at Re in the grafted complex even though the electronic

structure of the grafted site is clearly different from the isolated molecule (Figure 3-1b).

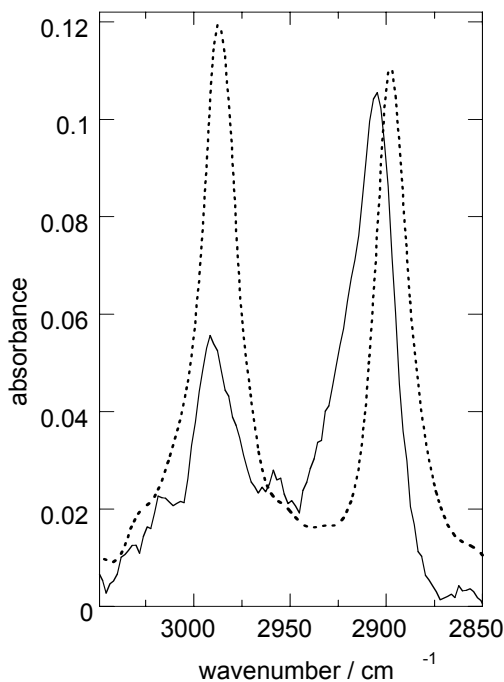


Figure 3-3. Comparison of FTIR spectra obtained for polycrystalline CH_3ReO_3 (in a KBr pellet, dashed line) and CH_3ReO_3 grafted on silica-alumina (2.3 wt.% Re, solid line), in the $\nu(\text{CH}_3)$ region.

The single-pulse ^1H MAS NMR spectrum of the unmodified, dehydrated silica-alumina is shown in Figure 3-4b. The peak at 1.6 ppm and its downfield shoulder at 2.3 ppm are attributed to isolated (non-interacting), terminal silanol groups^{127,152} with a distribution of acidities and hence chemical shifts.¹²⁶ No signals for terminal AlOH groups (ca. 1 ppm), bridging AlOHAl groups (2.5-3.6 ppm) or zeolite-like bridging hydroxyls AlO(H)Si are observed (3.8-4.4 ppm)^{126, 153, 154} in agreement with literature reports that all protons in silica-rich amorphous silica-aluminas are associated with silanol sites.^{152, 155}

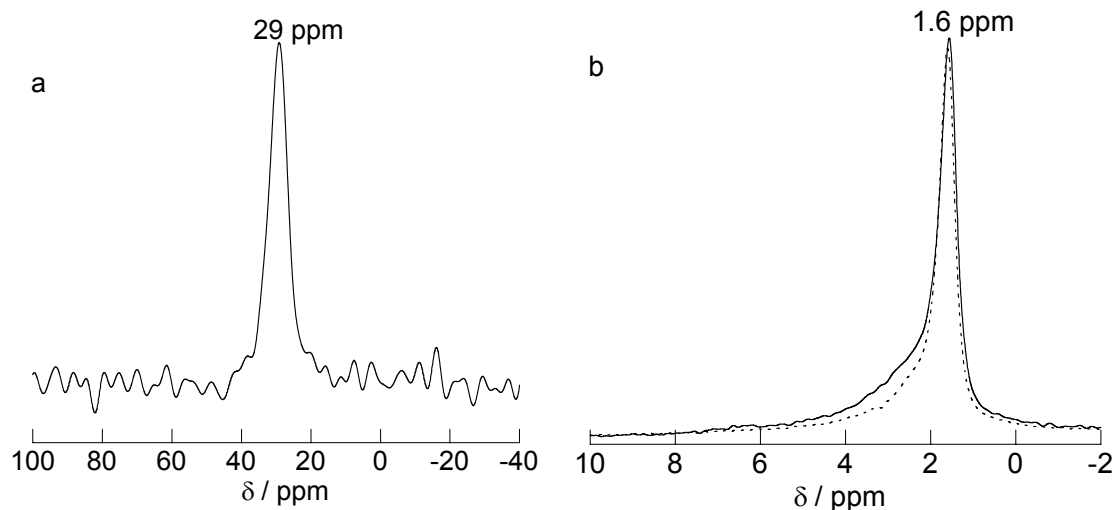


Figure 3-4. (a) ^{13}C CPMAS spectrum for silica-alumina modified with $^{13}\text{CH}_3\text{ReO}_3$ and (b) single-pulse ^1H MAS NMR spectra of dehydrated silica-alumina before (dashed line) and after (solid line) modification with $^{13}\text{CH}_3\text{ReO}_3$ (0.4 wt.% Re). Spinning rate 12 kHz.

The ^1H MAS spectrum retains the strong signals for the silanol protons with virtually unchanged chemical shifts relative to the unmodified support upon grafting of $^{13}\text{CH}_3\text{ReO}_3$ onto the dehydrated silica-alumina support at a loading of 0.4 wt.% Re. However, the downfield shoulder is slightly broader, with the presence of an additional signal at ca. 3 ppm from the methyl protons of grafted organorhenium fragments. For comparison, the ^1H spectrum of CH_3ReO_3 in CDCl_3 consists of a single peak at 2.64 ppm (Figure 3-1a).

In an effort to locate the ^1H signal from the adsorbed CH_3ReO_3 a two-dimensional $^{13}\text{C}\{^1\text{H}\}$ HETCOR MAS NMR experiment was carried out. The HETCOR contour plot, Figure 3-5., shows a strong intensity correlation between the ^{13}C and ^1H signals at 29 ppm and 2.8 ppm, respectively, which establishes that a weak ^1H signal at this position corresponds to the methyl protons of grafted CH_3ReO_3 . Moreover, the absence of any intensity correlation between the ^{13}C methyl signal and the silanol signal at 1.6 ppm demonstrates that dipole-

dipole coupling between the methyl group and these hydroxyl groups was weak during the 3 ms contact time, which in turn suggests that most of the grafted CH_3ReO_3 sites are not within molecular proximity of the silanol sites at this low Re loading. This finding is in contrast to a study of the adsorption of CH_3ReO_3 in zeolite HY, which concluded that H-bonding between an oxo ligand and an internal hydroxyl group was the main mechanism for binding of CH_3ReO_3 .^{20, 147}

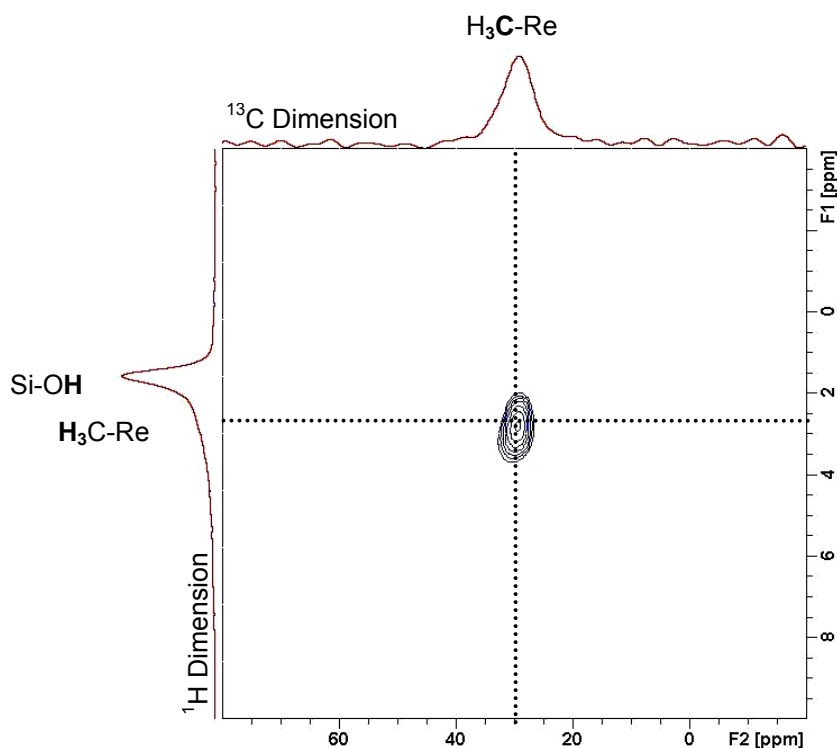


Figure 3-5. Two-dimensional $^{13}\text{C}\{^1\text{H}\}$ HETCOR MAS NMR spectrum for silica-alumina modified with $^{13}\text{CH}_3\text{ReO}_3$ (0.4 wt.% Re). The corresponding 1D ^{13}C CPMAS and single pulse ^1H MAS NMR spectra are plotted along their respective axes.

Quantitative MAS NMR spectroscopy. A possible participation of silanol groups in the grafting process was investigated in more detail by quantitative analyses of the single-pulse ^1H MAS NMR spectra of silica-alumina before and after deposition of CH_3ReO_3 . The fitted integrated ^1H peak areas were compared

to that of the well-resolved ^1H signal at -0.1 ppm of PDMS, a small (ca. 1 mg) piece of which was added as an internal intensity standard. Within the uncertainty of the NMR measurements ($\pm 5\%$), the intensity of the ^1H silanol peak remains unchanged in the presence of 2.3 wt.% Re (Figure 3-6.) which indicates that the silanols are not consumed during grafting. The quantitative ^1H MAS spectrum yields a silanol content of the dehydrated silica-alumina as 2.0 ± 0.2 OH/nm², which is consistent with a previously reported literature values.¹²⁹ The ^1H signal of grafted CH_3ReO_3 is in fact clearly observed at 2.8 ppm at a higher Re loading. These experiments indicate that grafting of CH_3ReO_3 does not involve the surface silanols of silica-alumina at low Re loadings. Instead CH_3ReO_3 appears to bind selectively at Lewis acidic Al sites.

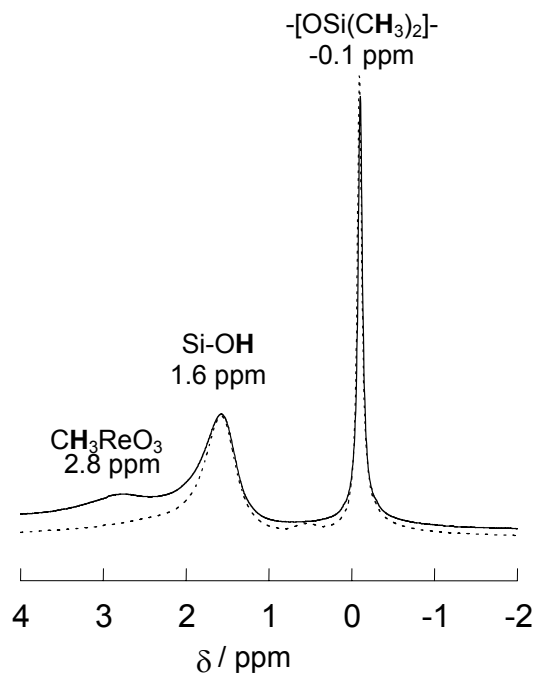


Figure 3-6. Single-pulse ^1H MAS spectra for the same quantity (60 mg) of the dehydrated silica-alumina support before (dashed line) and after (solid line) grafting CH_3ReO_3 (2.3 wt.% Re). A small piece of PDMS (-0.1 ppm) was included as an internal intensity standard.

This hypothesis was investigated with the use of quantitative ^{27}Al MAS NMR measurements, which can be accomplished by utilizing the signal at 113 ppm from a small (2.3 mg) piece of ^{27}AlN included as an internal intensity standard. The hydrated form of silica-alumina (5.7 wt.% Al) exhibits (Figure 3-7.) two ^{27}Al peaks at 55 and 2 ppm, with relative intensities of 1.5:1. These are assigned to four- and six-coordinate AlO_x sites, respectively.¹⁵⁶ After dehydration at 450 °C for 12 h, a dramatic reduction (ca. 90%) in ^{27}Al signal intensity occurred under otherwise identical conditions (same quantity of sample on a water-free basis, same NMR acquisition parameters, etc). This loss of ^{27}Al signal intensity is attributed to the presence of locally distorted Al environments, resulting in large quadrupolar coupling constants, as has been reported for dehydrated zeolite¹⁵⁷ and MCM-41-type¹²³ materials.

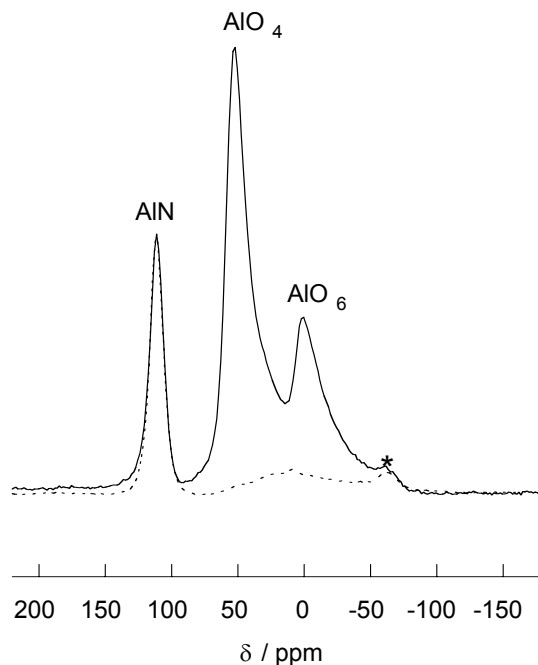


Figure 3-7. ^{27}Al MAS NMR spectra for hydrated silica-alumina (solid line) and dehydrated silica-alumina (dashed line), recorded in the presence of bulk aluminum nitride (2.3 mg) as an internal standard. The superimposed spectra were acquired with similar amounts of samples (dry basis) and identical experimental parameters and conditions (spinning speed, 14 kHz).

* denotes a spinning side-band of AlN

Rehydration of the dry silica-alumina by exposure to water vapor at room temperature only partly restored the total ^{27}Al signal intensity to about 60% of its value for the hydrated support, while the ^{27}Al peaks remain broadened and indistinct. The distortion of the ^{27}Al sites that occurs during dehydration is, therefore, not readily reversible. Grafting CH_3ReO_3 onto dehydrated silica-alumina resulted in virtually no change in the ^{27}Al MAS spectrum, relative to the spectrum of the dehydrated support before grafting. This result is consistent with associating the bound CH_3ReO_3 with the distorted, low symmetry Al sites, whose resulting coordination number is thereby not directly revealed and remains a challenging objective for further characterization. Application of high magnetic fields and high MAS spinning speeds may contribute significantly to this understand and help correlate the structures of sites containing quadrupolar nuclei with adsorption or active sites.

X-ray absorption spectroscopy. The precise details of binding of CH_3ReO_3 to silica-alumina could, however, be established by careful analysis of Re L_{III} edge EXAFS data. A striking change in this EXAFS spectrum occurs when CH_3ReO_3 is grafted onto silica-alumina (Figure 3-8.) compared to of the ungrafted CH_3ReO_3 (Figure 3-2.). Most notably, a reproducible feature in non-phase-corrected R-space appears at ca. 2.7 Å, Figure 3-8b. It is attributed to interaction of the photoelectron wave with an atom Y of the silica-alumina support. Features at this distance are typically observed only for absorbers surrounded by large, rigid ligands, or in crystal lattice sites.¹⁵⁸ They are not usually prominent in amorphous materials or in metal complexes grafted to amorphous supports.¹³⁵ The appearance of this peak therefore requires a high degree of organization and uniformity in the grafted CH_3ReO_3 sites, i.e., the presence of a well-ordered shell

in the second coordination sphere of Re. Such a shell implies a highly specific interaction between CH_3ReO_3 and the silica-alumina surface.

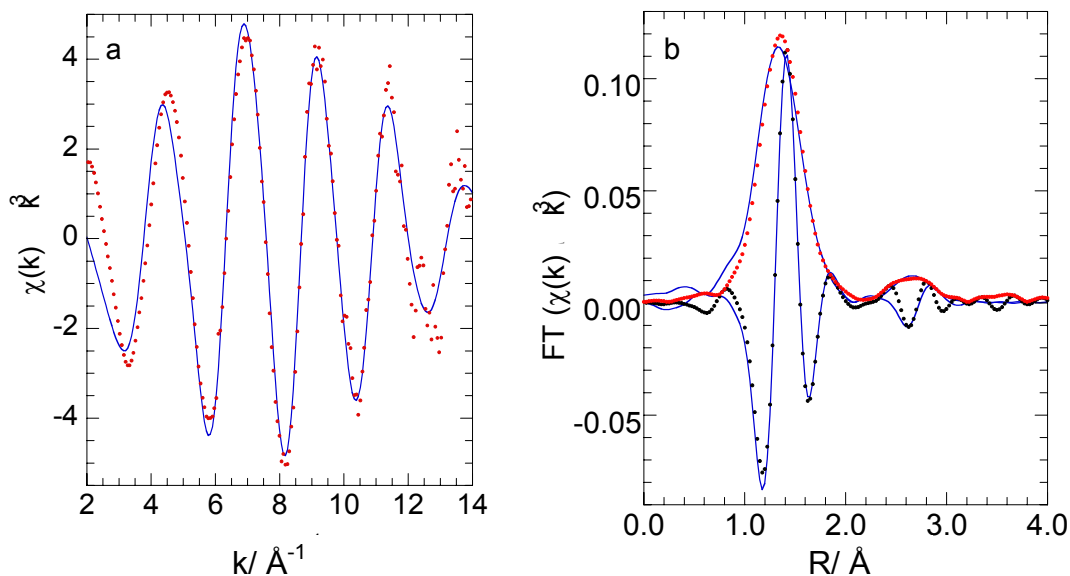


Figure 3-8. EXAFS data in (a) k^3 -weighted k -space (red points) and (b) non-phase-corrected R -space (imaginary, black points and FT magnitude, red points), for CH_3ReO_3 adsorbed on dehydrated silica-alumina (1.3 wt.% Re). Parameters for the curve-fit (blue lines) with integer coordination numbers are given in Table 3-2.

The starting point for curve-fitting the EXAFS spectrum of grafted CH_3ReO_3 was the isolated CH_3ReO_3 as a model, with an additional Re-Al path to account for the peak at 2.7 \AA in R -space. In order to minimize the number of correlated parameters, coordination numbers were fixed at their integer values. For each path, the distance (R) and Debye-Waller factor (σ^2) were refined sequentially.

The curve fit improved significantly when the symmetry of the oxygen shell was relaxed. Two Re=O paths converged to the same distance, while the third was significantly elongated. However, the fit contained unreasonably small Debye-Waller factors ($<1 \times 10^{-3} \text{\AA}^2$) for some paths.¹⁵⁹ This result suggests the presence of an additional scatterer in the first coordination sphere. Inclusion of a fourth Re-O

scattering path, presumed to involve an oxygen atom of the support, caused the Debye-Waller factors to increase to physically meaningful values, comparable in magnitude to those obtained for molecular CH_3ReO_3 . The curve-fit and its associated fit parameters are shown in Figure 3-8. and Table 3-2., respectively. The fit and the experimental data match very well in both k-space and R-space.

Table 3-2. Comparison of EXAFS path lengths (Å) for CH_3ReO_3 grafted onto dehydrated silica-alumina, with DFT-calculated bond distances for two models of CH_3ReO_3 grafted onto an aluminosilsesquioxane cube.

path	N	EXAFS curve-fit ^a		DFT calculated distances	
		R (Å)	σ^2 (Å ²)	model IV	model II
Re=O	2	1.69	0.0012	1.690	1.694,1.695
Re=O	1	1.79	0.0016	1.804	1.811
Re-C	1	2.07	0.0012	2.095	2.096
Re-O _{support}	1	2.13	0.0056	2.282	2.182
Re-Al	1	3.06	0.0054	2.988	3.067

^a The inner potential energies (ΔE_0) and global amplitude reduction factor (S_0^2) were fixed at 0.0 eV and 1.0, respectively, during the fit (see text). Coordination numbers were fixed at their integer values (N). Residual = 21.

When coordination numbers for the EXAFS fit were also allowed to vary, they produced integer values for all shells ($\pm 15\%$), well within the accepted error of the EXAFS technique.¹⁵⁹

It was further investigated whether an additional oxygen shell or a multiple scattering interaction might be responsible for the EXAFS peak at ca. 2.7 Å. Both were ruled out by poor agreement between the curve-fit and the data. The possibility was also considered that this feature is a Re-Re path, caused by association of CH_3ReO_3 on the silica-alumina surface. Direct interactions of

CH_3ReO_3 are not observed in organic solvents, nor in polycrystalline CH_3ReO_3 ,¹⁵⁰ however, spontaneous polymerization of CH_3ReO_3 occurs in aqueous solution.¹⁶⁰ Curve-fitting to a model constructed from the structure of polymeric CH_3ReO_3 resulted in a physically implausible Re=O path length and an unreasonably large Debye-Waller factor for the Re-Re path.¹⁵⁹

Computational modeling. DFT calculations were employed in an effort to probe the soundness of the EXAFS model reported in Table 3-2., which in turn, would serve to verify that the model chosen for the computational analysis was realistic. In the first instance the structure of the isolated CH_3ReO_3 molecule was minimized using DFT to optimize the combination of functional and basis set to be used in further calculations. Table 3-1. compares the calculated Re=O and Re-C distances with those obtained for polycrystalline CH_3ReO_3 by EXAFS in this work, as well as published results from gas-phase electron diffraction, and neutron powder diffraction on polycrystalline CH_3ReO_3 . The high level of overall agreement establishes the legitimacy of the computational approach.

The first step in a computational investigation of possible structures for grafted CH_3ReO_3 must be the selection of a structural model for the silica-alumina support. Since silica-aluminas are amorphous with respect to their short- and long-range order, all models are necessarily approximate. Crystalline aluminosilicate frameworks, such as the zeolites, are not appropriate models, because their structures contain charge-compensating alkali cations and/or strongly acidic, bridging hydroxyl sites that are absent in amorphous silica-aluminas.¹⁵⁵ Periodic structures for crystalline silica have been used to represent amorphous silica in calculations.¹⁶¹ However, it has been observed experimentally that CH_3ReO_3 does not adsorb strongly onto silica, nor does the

resulting physisorbed material catalyze olefin metathesis.¹⁶² Crystalline aluminas are also inappropriate models because they lack the strong acidity of silica-alumina, which appears to be necessary for high catalytic activity in olefin metathesis.

Structural information for amorphous silica-alumina is difficult to obtain, although neutron diffraction methods have recently provided insight on the distribution of Si-O-Si angles in amorphous silica.¹⁶³ Some parameters for silica-alumina have been obtained by ²⁷Al and ²⁹Si solid state NMR^{164, 165, 166} and Al XANES.¹⁶⁷ In fully dehydrated silica-aluminas with low alumina contents (≤ 32 wt.% Al₂O₃), the vast majority of Al sites are four-coordinate^{167, 168} and they do not bear hydroxyl groups, either terminal or bridging.¹⁶⁹ Reversible changes to and from six-fold coordination during chemisorption of water and ammonia have been documented by ²⁷Al NMR¹⁷⁰ and Al K-edge XANES.¹⁶⁸ A minor component (< 10 mol%) of tricoordinate Al has been identified in steamed zeolites,¹⁷¹ which likely contain an amorphous silica-alumina component.¹⁶⁸ The Lewis acidity of amorphous silica-aluminas is believed to arise from the presence of coordinatively unsaturated Al sites,¹⁷² while their Brønsted acidity is associated with terminal silanols located adjacent to these Al sites.¹⁷⁰

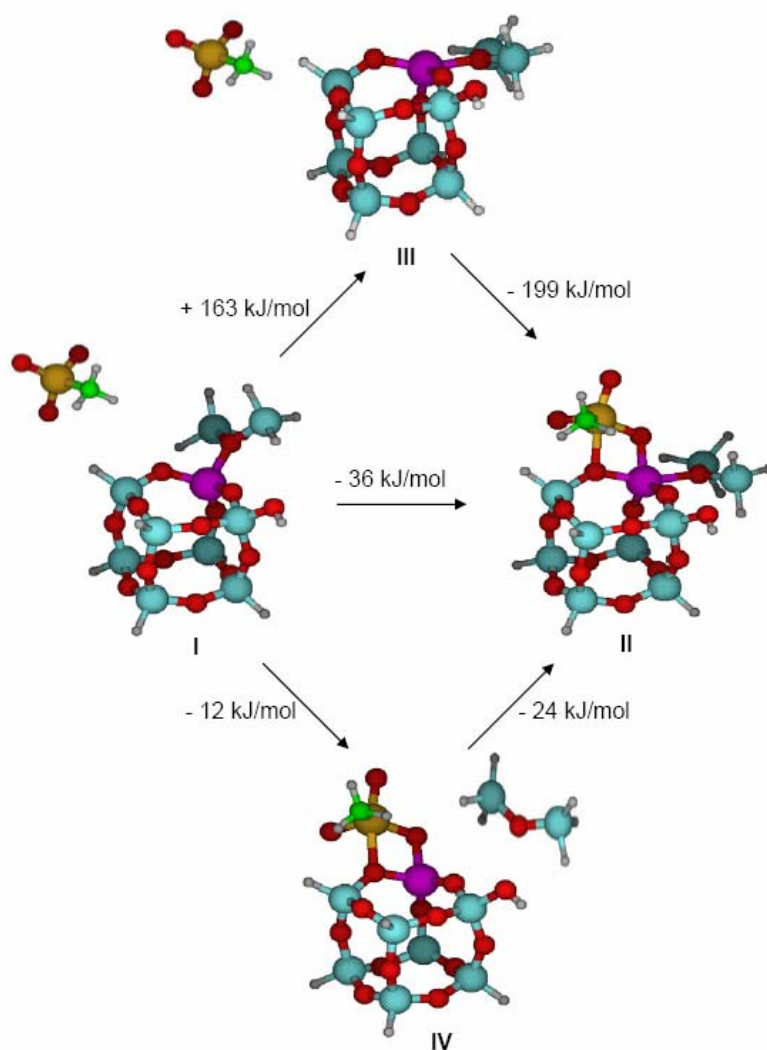
Cage-like structures, including the partially and fully condensed silsesquioxanes,¹⁷³ are better models for silica surfaces than the small clusters often used, because of their constrained Si-O-Si angles,^{174, 175} and because of their oxygen-rich nature. The analogy has been extended experimentally to aluminosilsesquioxane cubes, which were synthesized and characterized by single crystal X-ray diffraction as models for silica-alumina and aluminum-modified silica surfaces.^{176,177} Therefore an Al-substituted silsesquioxane

monosilanol was selected to model both Lewis and Brønsted acid sites on the surface of silica-alumina. The hydride-capped, all-Si version was modified by replacing one SiH corner with an Al atom, Scheme 3-1. An additional siloxane ligand ($\text{H}_3\text{SiOSiH}_3$) was included in order to impose four-fold coordination at Al (although this site is not tetrahedral, due to the constrained Si-O-Al angles of the cube, 115.6°). In the presence of a stronger Lewis base, the siloxane ligand could be displaced, modeling *latent* Lewis acidity in silica-alumina.¹⁷⁰

After minimizing the energy of the aluminosilsesquioxane cube, CH_3ReO_3 was attached to determine its optimal binding geometry. Since a suitable empirical potential for Re was not available, starting geometries could not be determined by typical docking calculations. Instead, the energies of plausible grafted forms of CH_3ReO_3 were compared.

The most energetically favorable interaction of CH_3ReO_3 with the aluminosilsesquioxane cube model involves coordination at the Al corner. The cube prefers to bind CH_3ReO_3 rather than $\text{H}_3\text{SiOSiH}_3$ at this site, shown in Scheme 3-1., as model IV, by 12 kJ/mol. Calculated bond distances are summarized in Table 3-2. One of the oxygen atoms of CH_3ReO_3 interacts with the Al corner of the cube, at an O-Al distance of 1.873 Å. Substantial lengthening of this Re=O bond upon grafting, from 1.690 to 1.788 Å, suggests a reduction in its bond order. This Lewis acid-base interaction is reinforced by a second interaction between Re and an adjacent, bridging oxygen of the cube (SiOAl). The interaction is slightly stronger with the more basic bridging oxygen on the OSi(H)OAl cube edge, at a Re-O bond distance of 2.260 Å and a Re-Si distance of 3.474 Å, compared to the OSi(OH)OAl edge. However, this is likely an artifact of H-termination in the model. There is ample experimental precedent for

coordination of Lewis bases to the electrophilic Re(VII) center in CH_3ReO_3 .^{178, 179, 180} Association of CH_3ReO_3 with a Lewis acidic Al site is expected to make Lewis base coordination even more favorable. CH_3ReO_3 also formed a stable adduct with the cube by binding to the Al corner only (i.e., without interacting with an adjacent bridging O), or by hydrogen-bonding via an oxo ligand to the silanol corner, although each of these configurations was of considerably higher energy than model IV.



Scheme 3-1. DFT-calculated reaction energies and structures for two models of the interaction between a siloxane-capped aluminosilsesquioxane monosilanol cube (representing the silica-alumina surface) and CH_3ReO_3 . Separated molecules should be interpreted as infinitely separated. Color scheme: Re (yellow), Al (purple), Si (blue), O (red), C (green), H (white).

Binding CH_3ReO_3 to the cube in the same geometry as in model **IV** but without displacing the siloxane, i.e., by expanding the coordination number at Al to five (model **II**), is even more stable, with the total energy lowered by an additional 24 kJ/mol relative to model **IV**. Similar changes in bond lengths upon grafting were predicted for model **II**. As expected, the O-Al distance involving the oxo ligand is longer (1.866 Å) in model **II** than in model **IV**, as is the Re-Al distance, at 3.044 Å. However, the approach of Re to the bridging oxygen of the cube, at 2.172 Å, is closer in model **II**. These results are consistent with a less Lewis acidic Al site in model **II**, and consequently a more basic oxygen donor in the adjacent cube bridging site.

Comparison of EXAFS and DFT-calculated structures. Fitted bond lengths from EXAFS are compared to the values calculated for both DFT models in Table 3-2. The agreement in the first three shells (i.e., the oxo and methyl ligands) is striking, especially for the highly constrained fit in which the coordination numbers, S_0^2 and ΔE_0 parameters are all held fixed. In particular, the EXAFS-derived elongation of one Re=O path by 0.10 Å relative to the other two is reproduced in the Re=O distances predicted by DFT. Curve-fitting was unable to distinguish between an Al or a Si scatterer in the second coordination sphere; both Re-Al and Re-Si paths resulted in reasonable fits. However, it would appear that Al is more likely to be responsible for the peak at 2.7 Å, because its flexible coordination number allows Al to interact directly with CH_3ReO_3 . In contrast, a Si neighbor would not be expected to expand its coordination sphere to accommodate CH_3ReO_3 , and indeed CH_3ReO_3 does not attach itself irreversibly to silica. Furthermore, the DFT models confirm that CH_3ReO_3 can engage in a highly favorable Lewis acid-base interaction with the Al site. The additional interaction of the organorhenium complex with an adjacent bridging oxygen of

the SiOAl bond creates a two-point attachment of CH_3ReO_3 to the surface, anchoring Re at a fixed distance from Al and thereby decreasing the Debye-Waller factor for this path.

The bond lengths of the shells representing interactions with the support (i.e., Re- $\text{O}_{\text{support}}$ and Re-Al paths) given by the EXAFS curve-fit show reasonable agreement with both 4- and 5-coordinate Al models. Heterogeneity of the amorphous silica-alumina surface and the approximate nature of the cube model may contribute to the small differences. Nevertheless, the agreement is better with model II which suggests that most grafting events involve the formation of five-coordinate Al sites. This is consistent with the ^{27}Al MAS NMR results, which show that the ^{27}Al signal that disappears nearly completely upon dehydration of silica-alumina is not restored upon grafting CH_3ReO_3 . Thus the low symmetry of the Al sites is preserved even after surface modification.

The spectroscopic and computational analyses therefore concur that the Lewis acidic Al sites of silica-alumina represent the most favorable chemisorption sites for CH_3ReO_3 at low loadings. The interaction of the organometallic complex with the support results in elongation of one Re=O bond and coordination to Re of an adjacent bridging oxygen from the surface. The resulting two-point attachment creates a well-defined grafted site that is electronically distinct from its molecular precursor

3.3 Deposition of higher loadings of CH_3ReO_3 on silica-alumina

While the chemisorption of CH_3ReO_3 at Lewis acid sites described in detail in section 3.2 above applies to loadings of less than 1 wt.% Re on the dehydrated Davicat 3113 silica-alumina, the maximum amount of CH_3ReO_3 that is strongly adsorbed by this support (i.e., that resists desorption during several hours of evacuation at 10^{-4} Torr and room temperature) corresponds to as much as 10 wt.% Re. Materials with Re loadings higher than that are unstable, and the excess CH_3ReO_3 desorbs rapidly upon evacuation of the reactor. These results suggest that different, but also rather specific grafting sites are responsible for the adsorption of CH_3ReO_3 at loadings between 1 and 10 wt.% Re.

1D and 2D NMR spectroscopy. Spectroscopic studies were employed to obtain information on the nature of the CH_3ReO_3 species bound to the silica alumina support at these higher loadings. First, the ^1H MAS spectrum of silica-alumina containing 10 wt.% Re as CH_3ReO_3 (Figure 3-9a) is found to be very similar to that for the material containing only 0.4 wt.% Re, although the peak for the methyl protons at 2.8 ppm is clearly resolved and is more intense relative to the signal at 1.6 ppm for the surface hydroxyl protons.

The ^{13}C CPMAS spectrum, on the other hand, is qualitatively different. Whereas at low loading (0.4 wt.% Re), only one relatively broad signal is present at 29 ppm, at higher loadings (10 wt.% Re) a much more narrow signal now appears at 20 ppm (Figure 3-9b). At least two chemically distinct environments for grafted CH_3ReO_3 must therefore be present at these higher Re loadings.

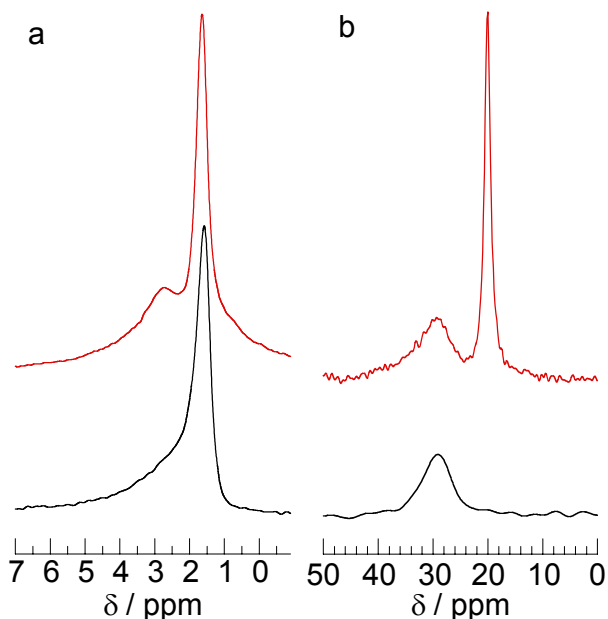


Figure 3-9. NMR spectra of $^{13}\text{CH}_3\text{ReO}_3$ adsorbed onto dehydrated silica-alumina, at two different loadings, 0.4 wt.% Re (black) and 10 wt.% Re (red): **(a)** single-pulse ^1H MAS NMR spectra; **(b)** ^{13}C CPMAS NMR spectra. Spin rate 12 kHz.

The chemical shift of the more shielded of the two groups of methyl sites (20 ppm) strongly resembles that of CH_3ReO_3 in CDCl_3 solution (19.6 ppm, 31 Hz fwhm). Furthermore, the narrow linewidth of 95 Hz fwhm suggests that the CH_3ReO_3 molecules grafted to these sites experience significantly higher mobility than the sites represented by the broad peak centered at 29 ppm (460 Hz fwhm). This narrow signal does, however, persist even after room temperature evacuation of the solid for several hours at $\leq 10^{-4}$ Torr, so that the CH_3ReO_3 molecules involved cannot be simply be weakly physisorbed. Narrow ^{13}C MAS NMR lines are unusual for supported organometallic complexes, which typically experience greatly reduced mobility when covalently bound to oxide surfaces, and thus exhibit broad solid state NMR peaks.¹⁸¹ The sites that give rise to the broad ^{13}C signal at 29 ppm, attributed to CH_3ReO_3 immobilized by two-point grafting onto Lewis acid/base sites, indeed appear to be just such low-mobility sites.

Further information on the nature and interactions of the grafted species can be derived from 2D HETCOR NMR experiments. The integrated intensities of the correlations observed in these spectra depend on the strengths and populations of dipole-dipole coupled ^1H and ^{13}C sites. The 2D $^{13}\text{C}\{^1\text{H}\}$ HETCOR spectrum shows strong intensity correlations for both ^{13}C methyl signals with the ^1H signals centered at 2.8 ppm, Figure 3-10. Only one ^1H signal was resolved, even at high loading (10 wt.% Re), presumably because of the smaller chemical shift range for ^1H compared to ^{13}C .

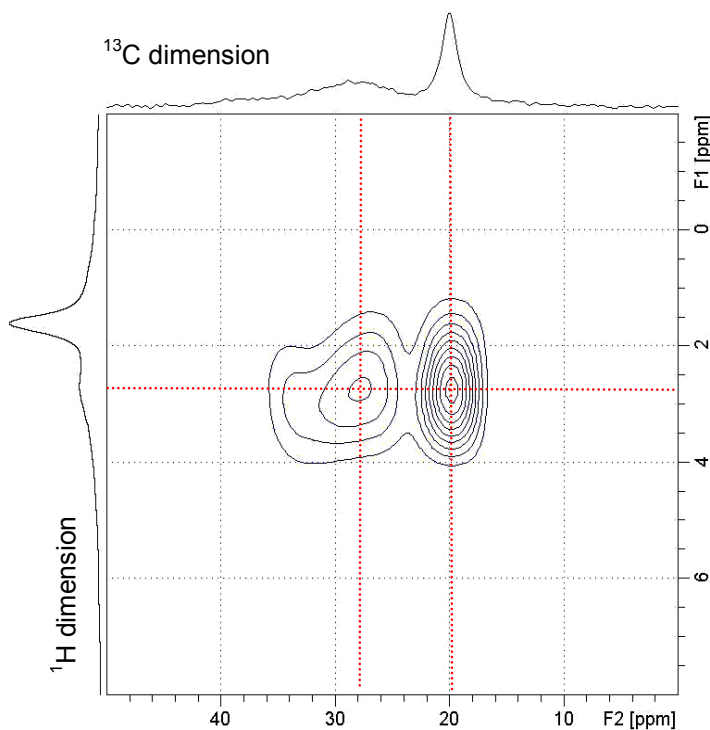


Figure 3-10. Two-dimensional $^{13}\text{C}\{^1\text{H}\}$ HETCOR MAS NMR spectrum for silica-alumina modified with $^{13}\text{CH}_3\text{ReO}_3$ (10 wt.% Re) recorded at room temperature with a mixing time of 3 ms and a spinning speed of 12 kHz. The corresponding 1D ^{13}C CPMAS and single pulse ^1H MAS NMR spectra are plotted along their respective axes.

The correlation for the ^{13}C peak at 20 ppm is surprisingly strong, considering that dipolar couplings in very mobile systems tend to average to zero. Therefore it is concluded that the narrow ^{13}C signal at 20 ppm must be comprised of

contributions from at least two different populations of adsorbed CH_3ReO_3 : (1) a relatively immobile species experiencing strong ^{13}C - ^1H heteronuclear dipole-dipole coupling such that its signal is enhanced by cross polarization and gives rise to the correlated signal intensity detected in the 2D $^{13}\text{C}\{^1\text{H}\}$ HETCOR spectrum; and (2) a highly mobile CH_3ReO_3 species that experiences weak ^{13}C - ^1H coupling, is not cross-polarized and does not contribute to the correlated HETCOR signal intensity.

The dynamics of the more mobile of the two families of grafted species were probed with static (non-MAS) solid state NMR experiments. The room temperature single-pulse ^{13}C spectra of a sample of $^{13}\text{CH}_3\text{ReO}_3$ on silica-alumina (6.5 wt.% Re), acquired consecutively under MAS and static conditions, are compared in Figure 3-11a. Whereas chemical shift anisotropy and dipole-dipole interactions are averaged by rapid molecular motion or under MAS conditions, they generally broaden spectral lines in non-MAS experiments. Consequently the ^{13}C signals for grafted organometallic species are often undetectable without MAS. The peak at ca. 29 ppm is broadened into the spectral baseline without MAS, which confirms that the species responsible for this signal possess low mobility. The linewidth of the peak at 20 ppm increases slightly to 200 Hz (from 95 Hz with 12 kHz MAS), but remains surprisingly narrow. However, its area decreases by approximately 20%, compared to that for the same sample recorded under MAS conditions. This result confirms that the peak at 20 ppm represents two, chemically similar populations of grafted CH_3ReO_3 that differ in the degree of their mobility.

Since the molecular mobility is reduced as the temperature is lowered, motional averaging of chemical shift anisotropy and dipole-dipole interactions are

diminished. This lower mobility is generally manifested in greatly increased linewidths. However, the ^{13}C signal at 20 ppm is still visible at $-100\text{ }^\circ\text{C}$ under static recording conditions, Figure 3-12., albeit broadened (1000 Hz fwhm) which shows the remarkable result that this grafted CH_3ReO_3 species retains some mobility even at such a low temperature.

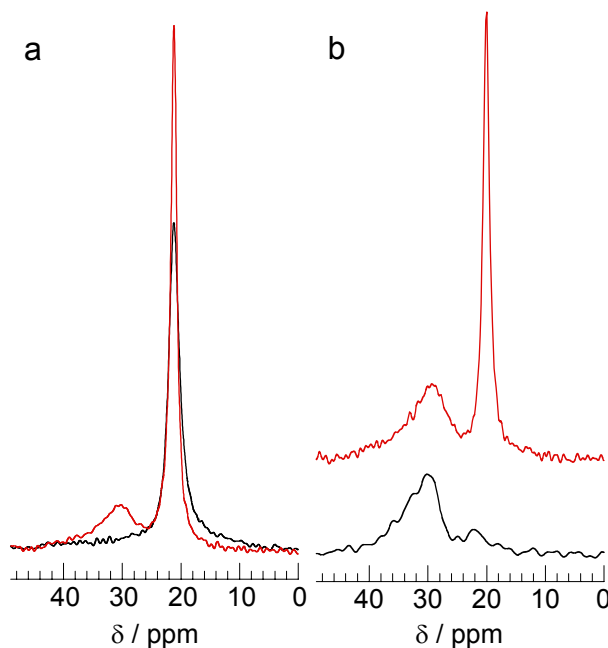


Figure 3-11. Single pulse ^{13}C NMR spectra for $^{13}\text{CH}_3\text{ReO}_3$ adsorbed onto dehydrated silica-alumina. **(a)** Spectra were acquired consecutively for the same sample (6.5 wt.% Re) with the same number of scans under both MAS conditions (12 kHz, red) and static conditions (black); **(b)** MAS spectra (12 kHz) were acquired for the same material before (10 wt.% Re, red) and after (6 wt.% Re, black) desorption of volatiles at $80\text{ }^\circ\text{C}$ for 6 h.

A 2D $^{13}\text{C}\{^1\text{H}\}$ HETCOR MAS study was therefore also carried out at $-100\text{ }^\circ\text{C}$. The results support the conclusions made from the room temperature measurements, in that strong correlations exist between the broadened ^1H signal at ca. 2.8 ppm and in both carbon signals (Figure 3-13.). No correlation was detected between either of the ^{13}C signals and the terminal, non-hydrogen-bonded silanol ^1H signal at 1.6 ppm, even when the contact time was increased from 3 to 12 ms in order to probe weaker coupling over longer intermolecular distances.

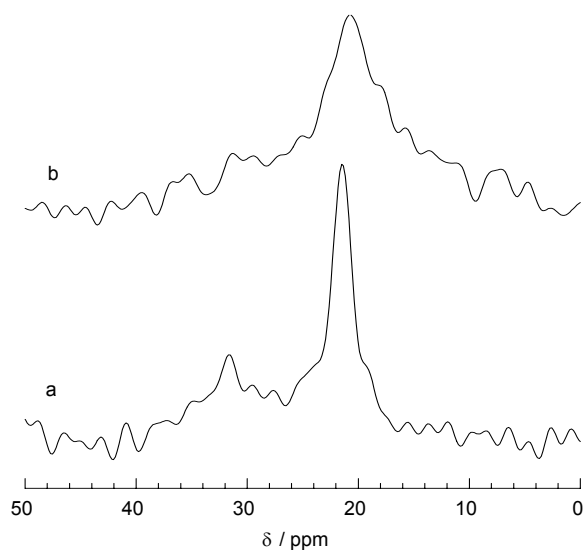


Figure 3-12. ^{13}C CP NMR spectra for CH_3ReO_3 grafted onto dehydrated silica-alumina (10 wt.% Re). Both spectra were recorded at -100°C , (a) with 8 kHz MAS; and (b) without spinning.

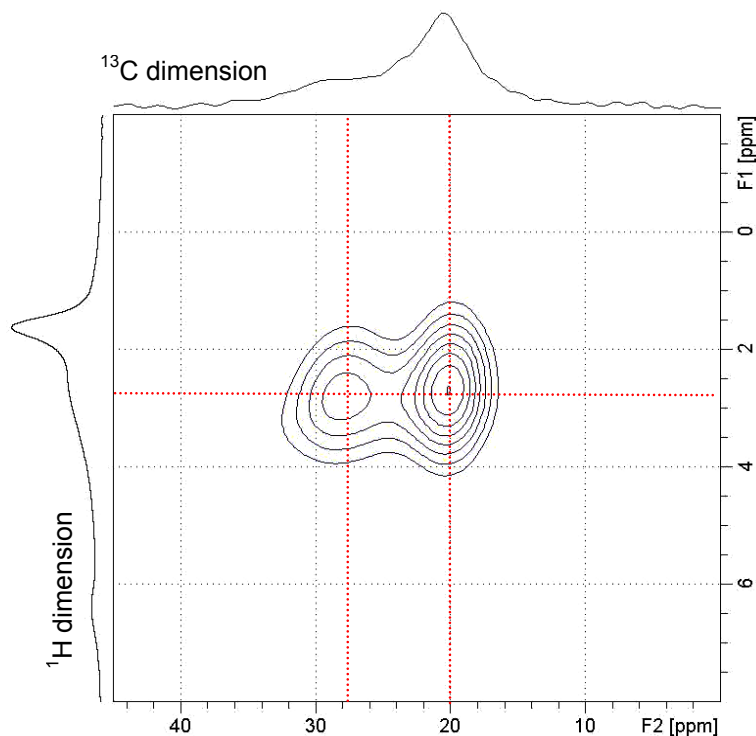
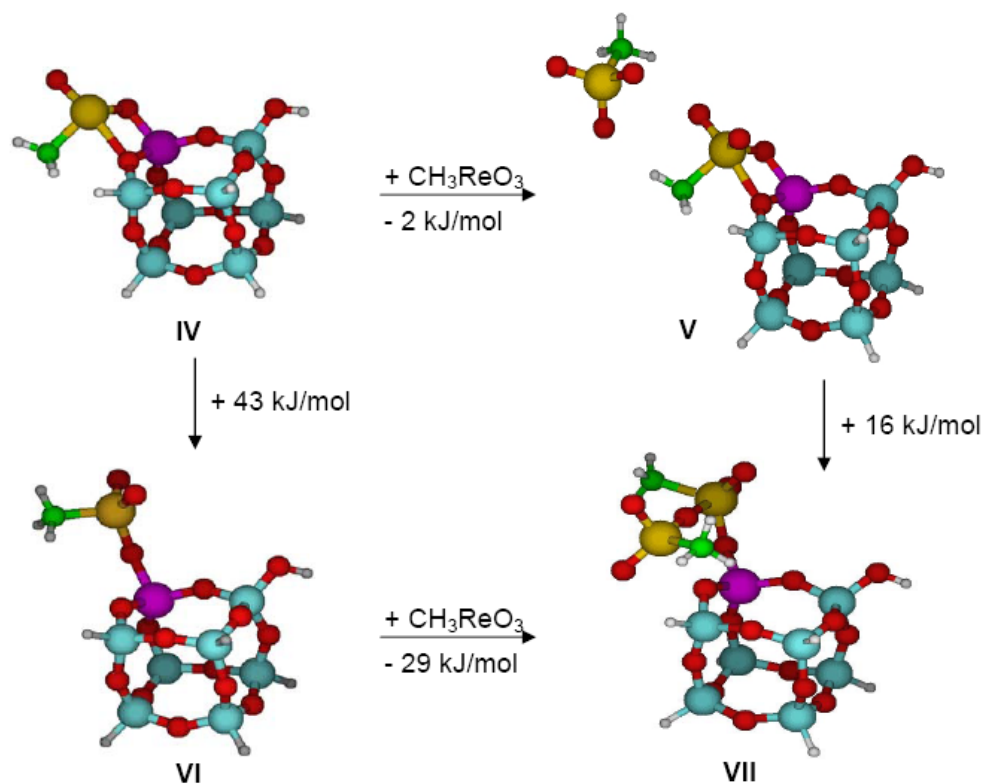


Figure 3-13. Two-dimensional $^{13}\text{C}\{^1\text{H}\}$ HETCOR MAS NMR spectrum for silica-alumina modified with $^{13}\text{CH}_3\text{ReO}_3$ (10 wt.% Re), recorded at -100°C with a mixing time of 12 ms and a spinning speed of 8 kHz. The corresponding 1D ^{13}C CPMAS and single pulse ^1H MAS NMR spectra are plotted along their respective axes.

While all of the grafted CH_3ReO_3 is stable to prolonged evacuation at room temperature, evacuation at elevated temperatures does result in partial desorption of some CH_3ReO_3 from the silica-alumina surface. Single-pulse ^{13}C MAS NMR spectra recorded before and after heating a sample initially containing 10 wt.% Re at 80 °C for 6 h are compared in Figure 3-11b. Prior to heating, the relative areas of the peaks at 29 and 20 ppm are ca. 2:1. Upon thermal treatment, the ^{13}C signal at 20 ppm disappeared, consistent with weaker binding of the more mobile grafted CH_3ReO_3 sites. At the same time, the Re content of the solid declined to 6 wt.% Re, consistent with desorption of some of the organometallic complex from the silica-alumina.

Computational study of mobile, grafted CH_3ReO_3 on silica-alumina. Highly mobile supported organic and organometallic molecules with narrow MAS NMR spectral lines have been reported where adsorption occurs via weak, electrostatic interactions, or by ion-pair formation.¹⁸²⁻¹⁸⁴ Some of these structures were used as starting points for DFT models of the highly mobile CH_3ReO_3 species that give rise to the narrow ^{13}C signals at ca. 20 ppm (Scheme 3-2.). For example, CH_3ReO_3 was found to form a weakly bound (-2 kJ/mol) van der Waals adduct **V** with the Lewis-grafted CH_3ReO_3 in structure **IV**. The non-specific nature of the attractive forces in the adduct **V** suggests that the second CH_3ReO_3 site should be highly mobile. However, the very low binding energy makes it unlikely that the van der Waals adduct **V** could resist desorption under dynamic vacuum at room temperature. Conversion of the van der Waals adduct to the Lewis acid-base adduct **VII** is unfavorable (+16 kJ/mol) because of the simultaneous loss of a Lewis acid-base interaction with the aluminosilsesquioxane cube. The possible protonation of CH_3ReO_3 to form a highly mobile cation $[\text{CH}_3\text{Re}(\text{O})_2(\text{OH})]^+$ was

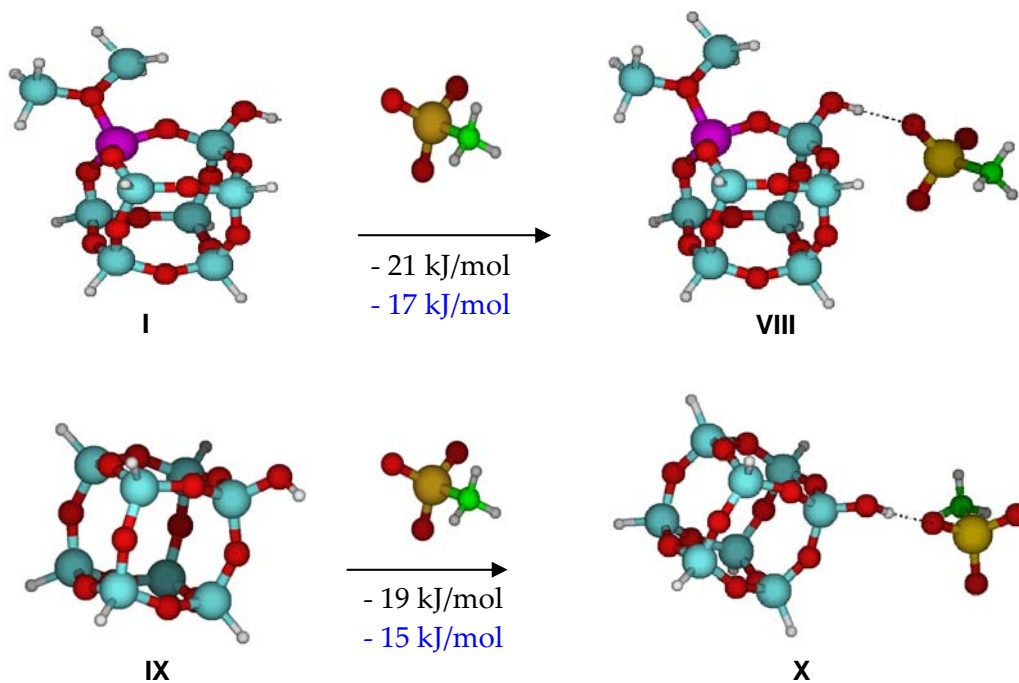
also investigated. This structure is highly energetic, and the proton moved spontaneously back to the aluminosilsesquioxane monosilanolate anion.



Scheme 3-2. DFT-calculated structures and reaction energies for postulated mobile forms of CH_3ReO_3 interacting with an aluminosilsesquioxane cube (representing the silica-alumina surface), and an immobile CH_3ReO_3 -aluminosilsesquioxane adduct.

CH_3ReO_3 has also been suggested to interact with acidic bridging hydroxyl groups in zeolites via H-bonding, on the basis of the close resemblance in the EXAFS spectra of polycrystalline CH_3ReO_3 before and after its adsorption in zeolite HY, as well as a red-shift in the frequency of a mode assigned to $\nu(\text{Re}=\text{O})$.^{20, 146} There is no spectroscopic evidence for the presence of zeolite-like bridging hydroxyls $\text{AlO}(\text{H})\text{Si}$ in dehydrated silica-alumina, either by IR¹⁸⁵ or ^1H MAS NMR,¹⁶⁶ however, it has been suggested that the terminal silanols of silica-alumina acquire strong Brønsted acidity by virtue of possessing one or more Al

neighbors.¹⁸⁵ Therefore hydrogen-bonding interactions between CH_3ReO_3 and surface hydroxyl groups were considered as a means of creating highly mobile sites. Hydrogen-bonding between CH_3ReO_3 and the terminal silanol of the aluminosilsesquioxane cube **I** is shown in structure **VIII**, Scheme 3-3. The energy of the H-bonding interaction was calculated to be 21 kJ/mol using the 6-31G* basis set, declining slightly to 17 kJ/mol with the larger 6-31+G** basis set. The energies computed for H-bonding of CH_3ReO_3 to the silanol of structure **IV** (containing CH_3ReO_3 grafted via Lewis acid-base interactions on the aluminosilsesquioxane cube) are similar (6-31G*: -17 kJ/mol; 6-31+G**: -15 kJ/mol).



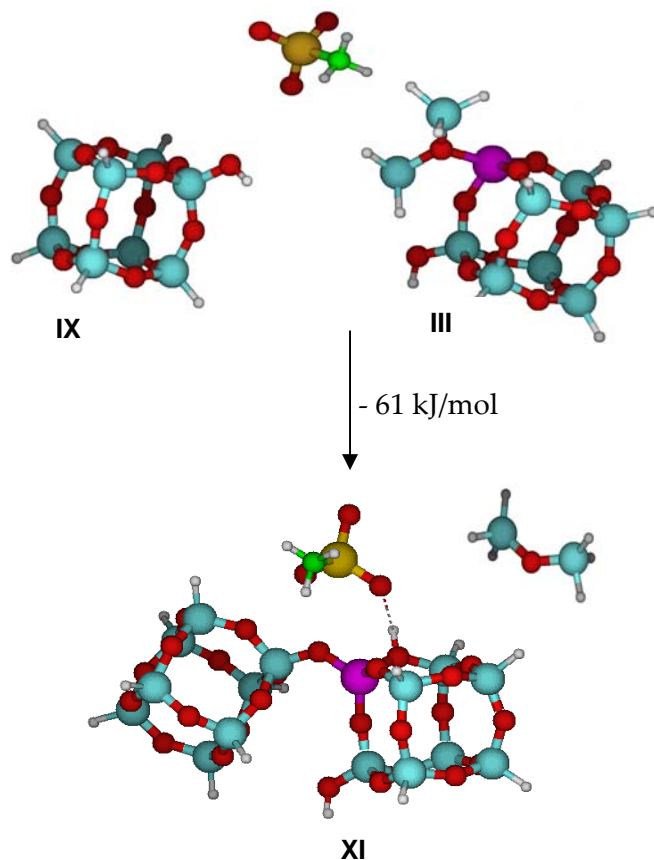
Scheme 3-3. DFT-calculated structures and reaction energies for CH_3ReO_3 interacting by H-bonding with an aluminosilsesquioxane monosilanol cube (representing the silica-alumina surface) and a silsesquioxane monosilanol cube (representing the silica surface). Binding energies shown in black and blue were calculated using 6-31G* and 6-31+G** basis sets, respectively. Color scheme: Re (yellow), Al (purple), Si (blue), O (red), C (green), H (white).

The effect of the aluminum neighbor on silanol acidity was investigated using CH_3ReO_3 hydrogen-bonded to the all-Si silsesquioxane monosilanol cube **IX**. The calculating binding energy is insignificantly different (-15 vs. -17 kJ/mol with 6-31G**) from that involving the aluminosilsesquioxane cube **I**. This result is inconsistent with the observation that CH_3ReO_3 desorbs from silica under vacuum at room temperature, while depopulation of the analogous sites on silica-alumina requires heating to 80 °C. The higher Brønsted acidity of the surface hydroxyls on silica-alumina relative to silica is thus not well reproduced in the simple silsesquioxane models. The reason for this is likely to be the presence of the siloxane ligand used to keep the Al, which replaces a H-terminated Si, four-coordinate.

A second model for the strong Brønsted acidity in silica-alumina proposes that the acidity is latent, i.e., manifested only in the presence of a suitable proton acceptor.^{170, 186} Scheme 3-4. illustrates this for CH_3ReO_3 . A terminal silanol becomes coordinated to Al as it transfers its proton to a bridging oxygen. The driving force for proton transfer is the strong hydrogen-bond created between the bridging hydroxyl and an oxo ligand of CH_3ReO_3 , structure **XI**. The calculated ^{13}C NMR chemical shifts for structures **XI** and **VIII** (25 and 17 ppm, respectively) bracket the observed chemical shift (20 ppm) for the mobile CH_3ReO_3 site on silica-alumina. This may indicate that the acidity of silica-alumina, and hence the actual strength of the hydrogen-bonding interaction, is intermediate between these two models for the acidic hydroxyls.

High mobility in any of the H-bonded CH_3ReO_3 sites could arise by rotation of the $[\text{CH}_3\text{ReO}_2]$ fragment about the Re-O-H-O axis, as well as rotation of the $[\text{CH}_3\text{ReO}_3\text{H}]$ fragment about the Si-O axis. In addition, CH_3ReO_3 may

interchange H-bonded and non-H-bonded oxo ligands via a hopping mechanism. The less mobile sites contributing to the cross polarization of the ^{13}C signal at 20 ppm may involve simultaneous hydrogen-bonding interactions between CH_3ReO_3 and more than one surface hydroxyl group, restricting its rotational motion.



Scheme 3-4. DFT-calculated structure and reaction energy for CH_3ReO_3 interacting by H-bonding with a bridging hydroxyl formed upon reaction of a terminal silanol with the Al corner of an aluminosilsesquioxane cube (representing the silica-alumina surface). Color scheme: Re (yellow), Al (purple), Si (blue), O (red), C (green), H (white).

Experimental Evidence for H-bonded CH_3ReO_3 on silica-alumina. The IR spectrum of a self-supporting pellet of dehydrated silica-alumina was recorded before and after deposition of CH_3ReO_3 . Grafting results in a decrease in intensity

of the $\nu(\text{SiO-H})$ mode at 3747 cm^{-1} , which is attributed to non-interacting surface silanols, accompanied by the appearance of a broad, red-shifted peak characteristic of $\nu(\text{SiO-H})$ for H-bonded silanols (Figure 3-14.). The changes in the $\nu(\text{SiO-H})$ region were reversed when the sample was heated to $80\text{ }^\circ\text{C}$ for 5 hours to remove the CH_3ReO_3 , i.e., the peak assigned to H-bonded silanols disappeared while the peak from the non-interacting silanols was restored to its initial intensity.

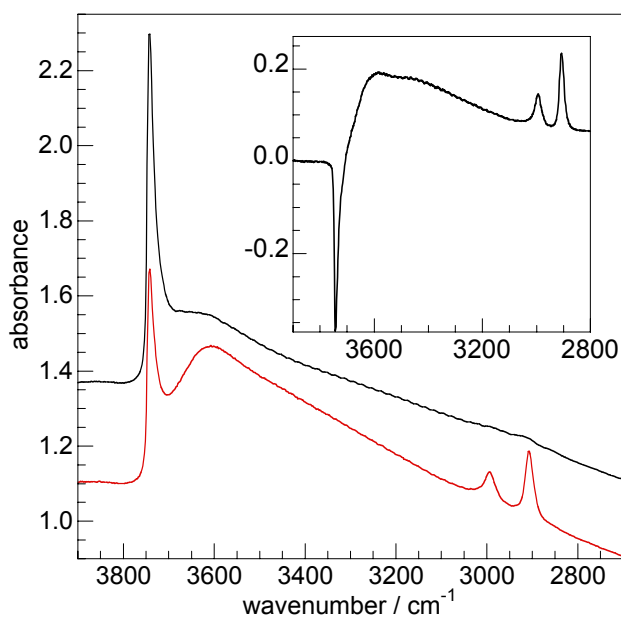
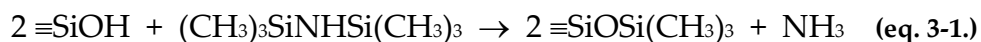


Figure 3-14. IR spectra of dehydrated silica-alumina before (black) and after (red) adsorbing CH_3ReO_3 (ca. 10 wt% Re), and the difference spectrum (inset).

Hydrogen-bonding is also expected to cause a significant downfield shift in the ^1H MAS NMR signal of the silanol protons that form the H-bond.¹³⁴ The strongly correlated signal intensity between the ^{13}C peak at 20 ppm and the ^1H signals between 2 and 3 ppm (Figure 3-10.) is in fact consistent with this interaction. Unfortunately, the signals from these H-bonded silanols overlap with those of the methyl protons of grafted CH_3ReO_3 . Furthermore, it was observed that the use of deuterium-labeling in CD_3ReO_3 to suppress the signal due to methyl

protons is precluded by rapid H/D exchange between the methyl group and the surface silanols of silica-alumina.

The presence of this hydrogen bonding interaction for the mobile grafted CH_3ReO_3 species can furthermore be indirectly verified by preventing the formation of H-bonded CH_3ReO_3 sites on silica-alumina by converting the accessible surface silanol groups to silyl ethers prior to grafting. Treatment of dehydrated silica-alumina with an excess of hexamethyldisilazane (HMDS) at room temperature effects this transformation and generates ammonia,¹⁸⁷ Equation 3-1.



After reaction, the capped silica-alumina must be heated to 350 °C under dynamic vacuum to effect complete desorption of NH_3 from the Lewis acid sites, as judged by the disappearance of the $\nu(\text{N-H})$ modes by IR. Deposition of $^{13}\text{CH}_3\text{ReO}_3$ onto capped silica-alumina produced a material with two ^{13}C NMR signals, Figure 3-15. The peak at -2 ppm is assigned to $(\text{CH}_3)_3\text{Si}$, while that at 30 ppm is assigned to CH_3ReO_3 grafted onto Lewis acid sites. No signal at 20 ppm was observed, consistent with the absence of silanols available to hydrogen-bond to CH_3ReO_3 .

The corresponding 2D $^{13}\text{C}\{^1\text{H}\}$ HETCOR MAS spectrum shows strong intensity correlations for the ^{13}C methyl signals at 30 ppm with the ^1H signals centered at 2.8 ppm, Figure 3-16., but no correlation with residual silanols (capping efficiency ~ 80%) is observed. The correlation between the carbons and protons of the capping agent hexamethyldisilazane is weakly seen with the mixing time of 3 ms.

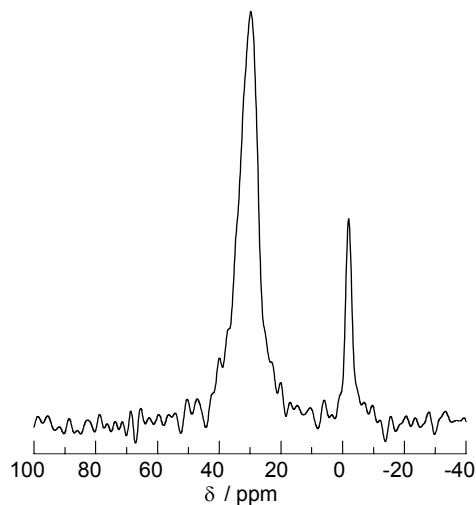


Figure 3-15. ^{13}C CPMAS NMR spectrum for dehydrated silica-alumina modified with hexamethyldisilazane, then by $^{13}\text{CH}_3\text{ReO}_3$ (1 wt.% Re). Spin rate 12 kHz.

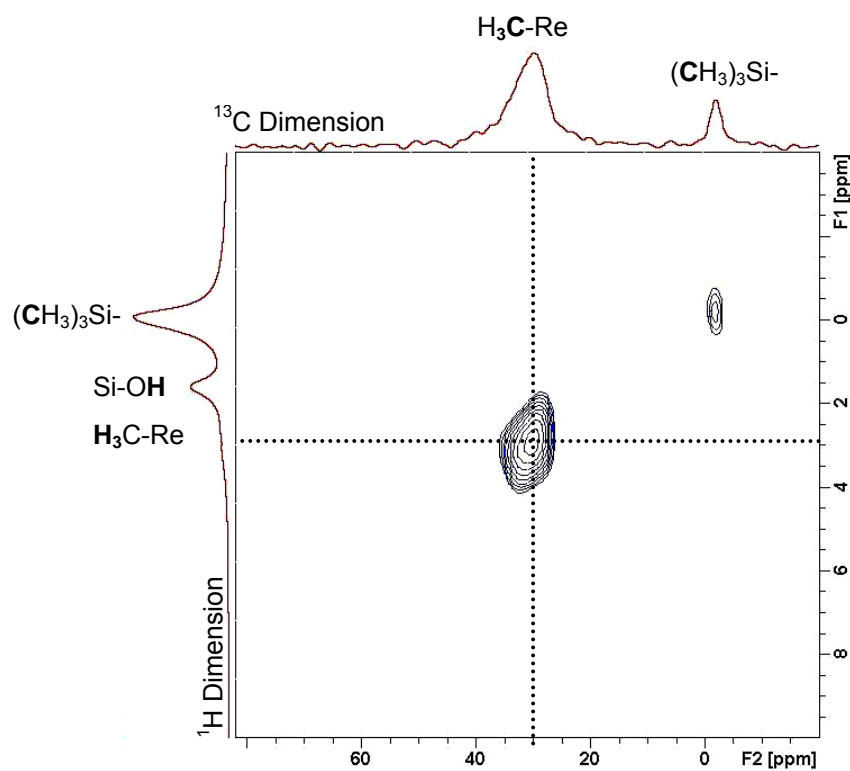


Figure 3-16. Two-dimensional $^{13}\text{C}\{^1\text{H}\}$ HETCOR MAS NMR spectrum for dehydrated silica-alumina modified first with hexamethyldisilazane followed by $^{13}\text{CH}_3\text{ReO}_3$ (1 wt.% Re) recorded at room temperature with a mixing time of 3 ms and a spinning speed of 12 kHz. The corresponding 1D ^{13}C CPMAS and single pulse ^1H MAS NMR spectra are plotted along their respective axes.

3.4 Deposition of CH_3ReO_3 on silica

In order to explore hydrogen bonding interactions between CH_3ReO_3 and surface silanols in the absence of Lewis acid sites similar NMR studies were performed on CH_3ReO_3 deposited onto amorphous silica. CH_3ReO_3 is not strongly adsorbed onto silica at room temperature and can be removed by prolonged evacuation (10^{-4} Torr). ^1H MAS and ^{13}C CPMAS NMR spectra of CH_3ReO_3 dispersed by vapor deposition onto dehydrated silica (containing 4 wt.% Re) are shown in Figure 3-17. After a brief (10 mins) exposure to dynamic vacuum, the ^1H NMR spectrum contains a doublet attributed to the methyl protons (2.6 ppm, $^1J_{\text{H-C}} = 135$ Hz) in addition to a signal at 1.7 ppm from the unperturbed silanol protons. The ^1H signals of grafted CH_3ReO_3 are presumably broader on silica-alumina than on silica, since no ^1H - ^{13}C coupling was detected on silica-alumina, even when ^{13}C -enriched samples were utilized for the ^1H MAS spectra. The coupling constant on silica, however, is the same as that measured for $^{13}\text{CH}_3\text{ReO}_3$ in CDCl_3 . The ^{13}C spectrum of CH_3ReO_3 dispersed on dehydrated silica consists of a single, sharp ^{13}C peak at 19 ppm (85 Hz fwhm).

The $^{13}\text{C}\{^1\text{H}\}$ HETCOR MAS experiment, Figure 3-18., confirmed that the ^{13}C signal correlates with the center of the ^1H doublet, whereas the non-interacting silanol signal shows no such intensity correlation.

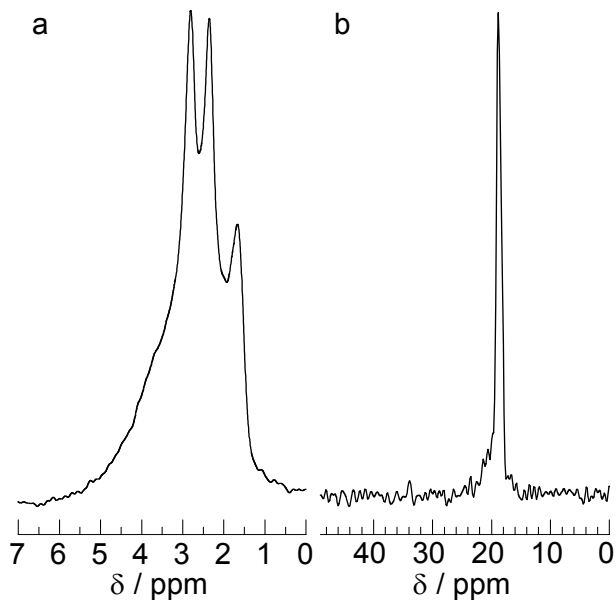


Figure 3-17. NMR spectra of $^{13}\text{CH}_3\text{ReO}_3$ adsorbed onto dehydrated silica (4 wt.% Re): **(a)** single-pulse ^1H MAS NMR spectrum; **(b)** ^{13}C CPMAS NMR spectrum. Spin rate 12 kHz.

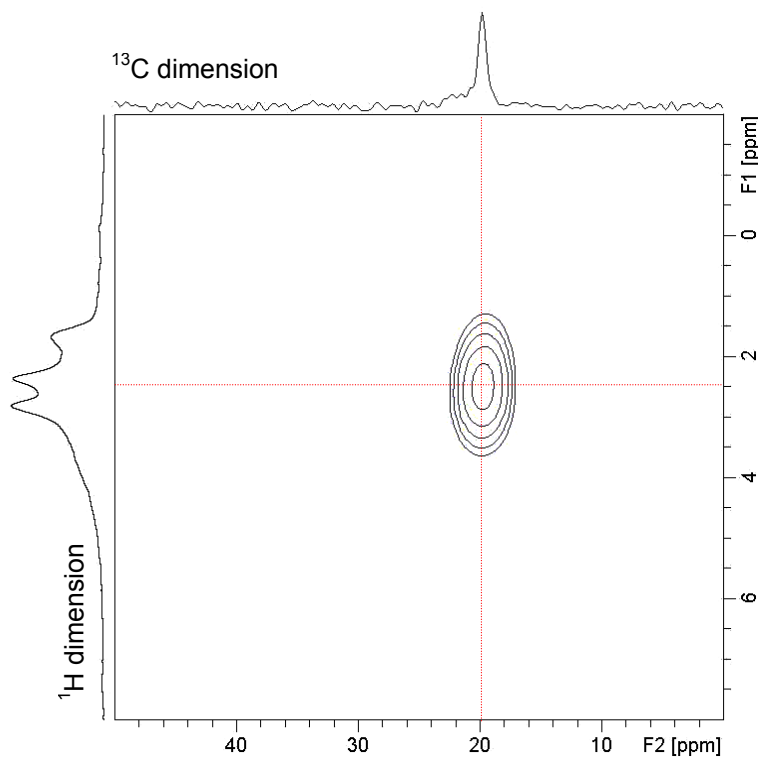


Figure 3-18. Two-dimensional $^{13}\text{C}\{^1\text{H}\}$ HETCOR MAS NMR spectrum for silica modified with $^{13}\text{CH}_3\text{ReO}_3$ (4 wt.% Re), recorded at room temperature with a mixing time of 3 ms and a spinning speed of 12 kHz. The corresponding 1D ^{13}C CPMAS and single pulse ^1H MAS NMR spectra are plotted along their respective axes.

The chemical shift and linewidth of the ^{13}C signal observed for CH_3ReO_3 on silica are thus shown to be remarkably similar to those of the mobile CH_3ReO_3 species present at high Re loading on dehydrated silica-alumina. Moreover, the ^{13}C signal for CH_3ReO_3 on silica is still visible without MAS and decreases in intensity by just 12% under static recording conditions. Since silica possesses no Lewis acidity and only weak Brønsted acidity, these results strongly support the assignment of the ^{13}C signal at 20 ppm for CH_3ReO_3 on silica-alumina to a mobile species that is hydrogen-bonded to surface silanol groups.

Finally, the silanol protons themselves are expected to show broadened, downfield-shifted signals in ^1H MAS NMR¹⁸⁸ upon formation of a hydrogen bond. The strength of the hydrogen bond is reflected in the magnitude of the change in chemical shift. For example, the ^1H signal at 1.7 ppm attributed to isolated silanols in a mesoporous silica was observed to shift to 5.5 ppm in the presence of adsorbed water.¹⁸⁹ Similar changes in proton chemical shift are expected for silica silanols perturbed by H-bonding to adsorbed CH_3ReO_3 . Indeed, the ^1H MAS NMR spectra of silica before and after adsorption of CD_3ReO_3 show the appearance of a very broad signal in the range 2-5 ppm, in addition to the expected peak for non-interacting silanols at 1.7 ppm and a small signal for incompletely deuterated methyl groups at 2.5 ppm, Figure 3-19. The broad signal may thereby be attributed to silanols perturbed by hydrogen bonding to CD_3ReO_3 .

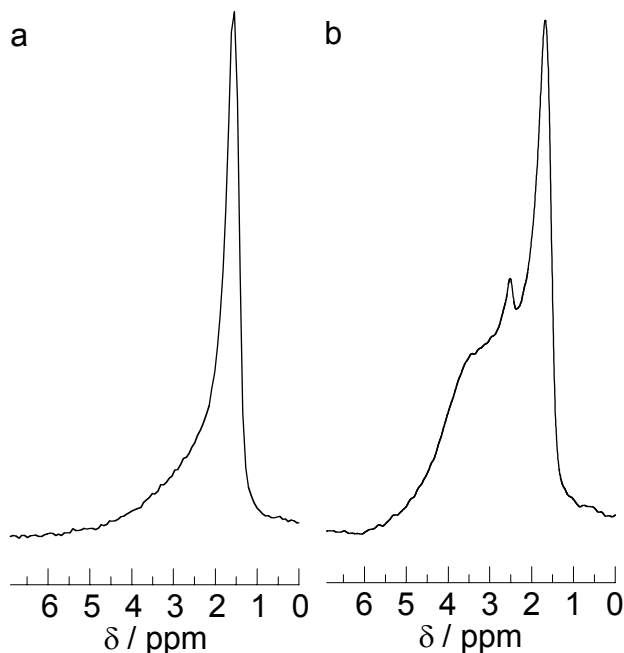


Figure 3-19. ^1H MAS NMR spectra for (a) dehydrated silica, and (b) CD_3ReO_3 (ca. 1 wt.% Re) on dehydrated silica, both recorded with 12 kHz MAS.

3.5 Activity and selectivity in olefin metathesis

Information obtained on the different CH_3ReO_3 species found on silica-alumina by the extensive spectroscopic, structural and computational studies described above, will now be related to the activity and selectivity for olefin metathesis of this catalyst. Silica-alumina is known to catalyze the self-metathesis of propylene over a wide range of CH_3ReO_3 loadings (0.1-10 wt.% Re). First, the activities of two samples with different loadings were compared, i.e. one containing 10 wt.% Re (two ^{13}C CPMAS NMR signals, at 29 and 20 ppm) and the other one with 1.0 wt.% Re (only one ^{13}C CPMAS NMR signal, at 29 ppm). Under identical reaction conditions (0 °C, 46 Torr C_3H_6 , 10.0 mg catalyst), the material containing 10 wt.% Re is in fact slightly *less* active ($k_{\text{obs}} = 0.11 \text{ min}^{-1}$) than the material with *ten times*

less CH_3ReO_3 ($k_{\text{obs}} = 0.18 \text{ s}^{-1}$). The corresponding kinetic profiles are compared in Figure 3-20. A catalyst prepared with capped silica-alumina, i.e. without any Brønsted acid sites, behaved similarly in this reaction (0.5 wt.% Re, $k_{\text{obs}} = 0.13 \text{ s}^{-1}$).

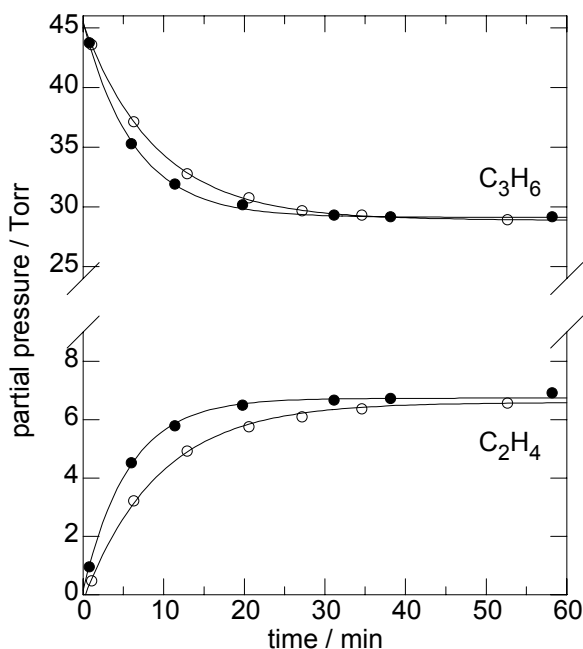


Figure 3-20. Kinetics of propylene metathesis (top: disappearance of C_3H_6 ; bottom: appearance of C_2H_4) over 10 mg CH_3ReO_3 /silica-alumina containing 1 wt.% Re (solid circles) and 10 wt.% Re (open circles), at 0 °C. Solid lines are non-linear least-squares curve fits to the integrated first-order rate equation.

As far as the selectivity is concerned, the catalyst containing 10 wt.% Re on silica-alumina yielded no olefins other than the expected metathesis products (ethylene, *trans*- and *cis*-2-butene) as found by GC/FID after equilibrium was attained, in ca. 1 h. The catalyst containing only 1 wt.% Re on silica-alumina, however, did produce detectable amounts of side-products in the same reaction time, including 1-butene and other higher olefins. These products are typical of the olefin isomerization and oligomerization reactions that are catalyzed by the acidic hydroxyl groups of silica-alumina.¹⁹⁰ At longer reaction times their formation eventually perturbs the equilibrium distribution of olefins arising from

propylene homometathesis. The absence of such side-reactions with the catalyst having higher Re loading therefore demonstrates the effect of blocking of the acidic hydroxyl sites by adsorption of CH_3ReO_3 on the metathesis-inactive sites, as modeled by structures **VIII** and **XI**.

Another sample of CH_3ReO_3 on amorphous silica with 4 wt.% Re, which exhibited only one ^{13}C NMR signal at 19 ppm (Figure 3-17.) showed no activity towards propylene under the same reaction conditions. It is therefore inferred that metathesis activity is associated with the ^{13}C NMR signal at 29 ppm, i.e., CH_3ReO_3 bound at Lewis acid sites. Conversely, CH_3ReO_3 which is hydrogen-bonded to hydroxyl groups on either silica or silica-alumina (and is responsible for the ^{13}C signals at 19-20 ppm) is shown to be inactive for olefin metathesis. A correlation between metathesis activity and Lewis acidity was previously noted for a related niobia supported CH_3ReO_3 catalyst, but no structural model for the grafted sites was proposed. From this study, it is clear that the use of this catalyst with high CH_3ReO_3 loadings is an inefficient use of Re, despite the improvement in selectivity. Furthermore, the weakness of the hydrogen-bonding interaction on the catalytically inactive CH_3ReO_3 sites is a likely cause of the leaching that has been observed to contaminate metathesis products.²²

3.6 Effect of different oxide supports on the binding and catalytic activity of CH_3ReO_3

The precise function of the support in heterogeneous Re-based olefin metathesis catalysts is rather complex, as it serves to activate the otherwise inactive molecular CH_3ReO_3 in providing binding sites for the catalyst. A number of oxides including silica-alumina¹⁹, niobia^{191, 192} alumina^{22, 193} and zeolites^{20, 146} have been investigated as supports for CH_3ReO_3 . Most of these reports on the catalytic activities of these systems are, however, essentially of rather qualitative nature, and do therefore not allow for a consistent, quantitative comparison of the effect of the different supports. The following discussion attempts to elucidate the importance of the interactions of CH_3ReO_3 with the support and the resulting mechanism for the activation of CH_3ReO_3 .

The unique properties of *dehydrated*, amorphous silica-alumina as the activating support were described in some detail in section 3.3 above. This material is derived from its hydrated form by calcination, which is accompanied by a weight loss of 15 wt.% as shown by thermogravimetric analysis. Discussion of the effect of different supports should therefore begin with hydrated silica-alumina, whereby the effect of the presence of water on the support on the activity of CH_3ReO_3 may be assessed.

Hydrated silica-alumina support. The ^1H MAS NMR spectrum of hydrated, silica-alumina treated with CH_3ReO_3 (1 wt.% Re) exhibits a very broad signal in the range from 0 to 10 ppm with sharper peaks at 6.7 ppm and 1.6 ppm. The signals can be attributed to physisorbed water molecules (6.7 ppm) and isolated

silanol moieties (1.6 ppm).^{127, 152} Furthermore bridging hydroxyls (4 ppm), silanol groups with hydrogen-bonded water^{188, 189} and water clusters are also expected to be present on the hydrated material and contribute to the wide range of site distributions.^{126, 153, 154} Additional ^1H peaks at 2 ppm and 3.8 ppm may be attributed to interactions of CH_3ReO_3 with acidic centers of the support, Figure 3-21a.

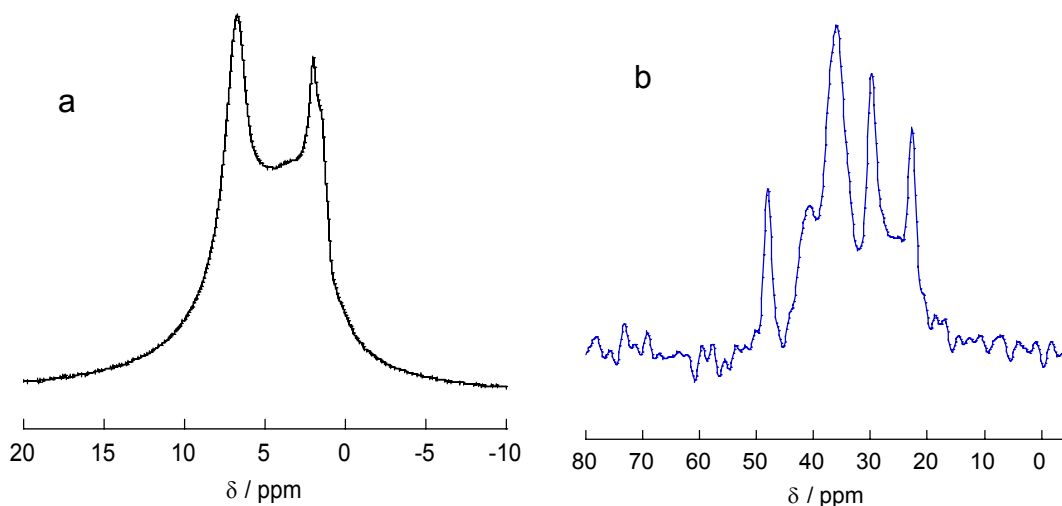


Figure 3-21. Hydrated silica-alumina with grafted $^{13}\text{CH}_3\text{ReO}_3$ (1 wt.% Re): (a) ^1H single-pulse MAS NMR and (b) ^{13}C CPMAS NMR spectrum (RT, 12kHz).

The ^{13}C MAS NMR spectrum of this system reveals a multitude of sites with chemical shifts spanning the range from 20 to 50 ppm including distinct peaks at 22, 30, 35, 40 and 48 ppm (Figure 3-21b). Two of these peaks may be assigned based on the above discussion of CH_3ReO_3 grafted onto dehydrated silica-alumina. In that case the interaction of CH_3ReO_3 with the Lewis acidic Al sites of the support results in a ^{13}C chemical shift of 29 ppm, whereas CH_3ReO_3 H-bonded to silanols has a ^{13}C chemical shift of 20 ppm. Similar ^{13}C peaks chemical shifts (22 and 30 ppm) in the hydrated material, along with peaks between 2 and 3 ppm in the ^1H spectrum, suggest that these interactions also occur on this

support. Similar sites with water present and the associated H-bonding interactions may alter the electronic environments around the Lewis acidic Al centers sufficiently to give rise to a related set of peaks between 30 and 40 ppm. Finally, impurities in the support, which would otherwise have been removed in the calcination process, may give additional NMR signals, as would the formation of species such as methoxytrioxorhenium species (48 ppm).^{194 195}

The two-dimensional $^{13}\text{C}\{^1\text{H}\}$ HETCOR experiment indeed (Figure 3-22.) shows that all these ^{13}C signals between 20 and 50 ppm are correlated to ^1H signals between 2 and 3 ppm, which in turn are associated with the organometallic species.

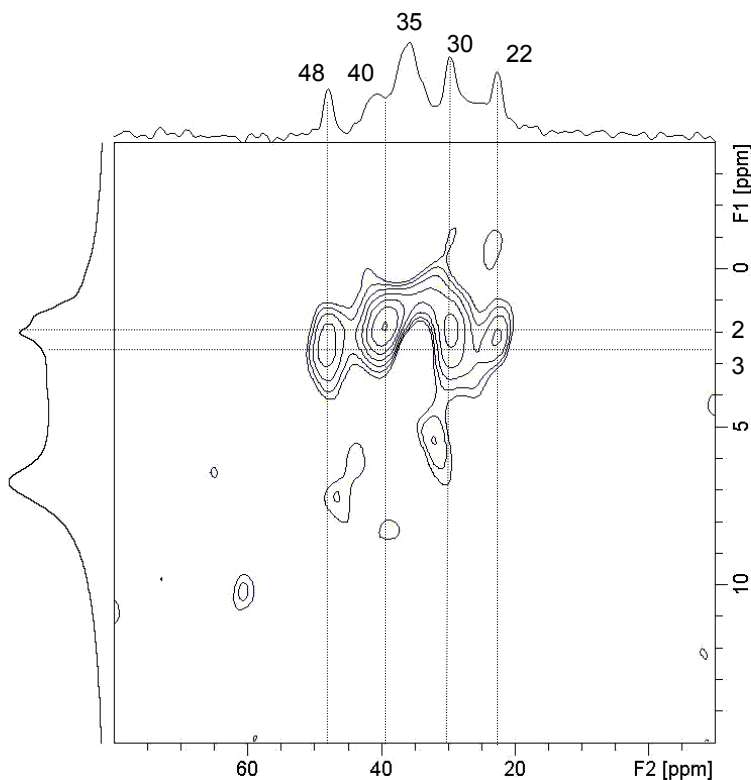
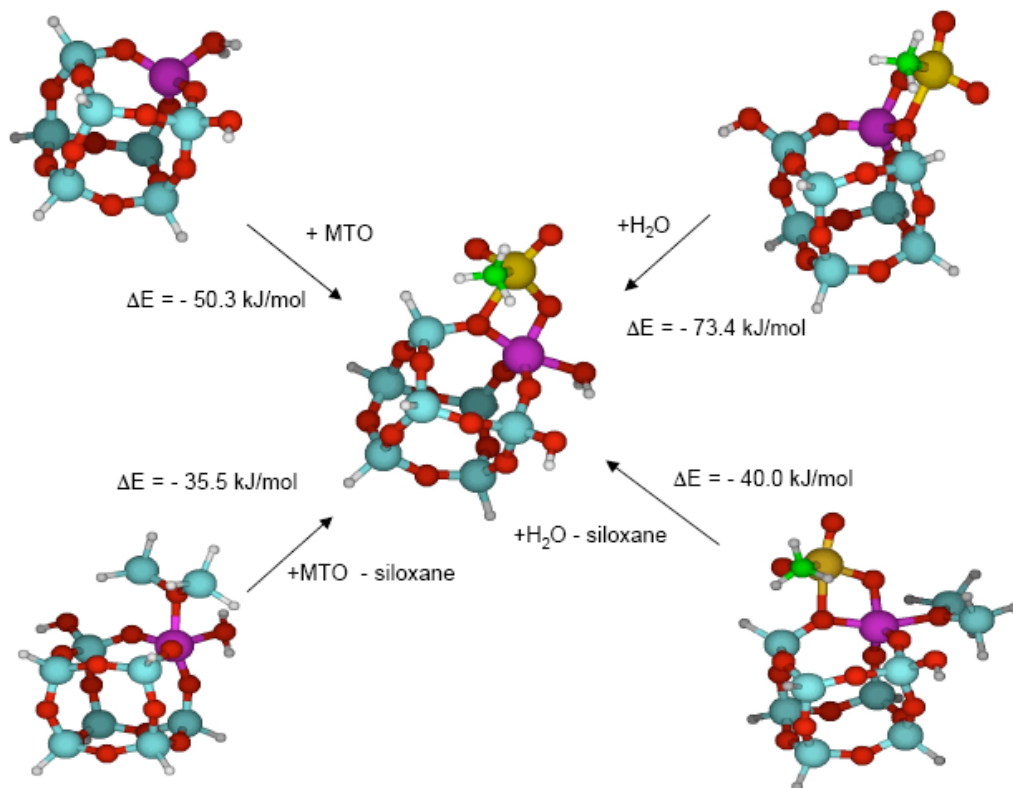


Figure 3-22. Two-dimensional $^{13}\text{C}\{^1\text{H}\}$ HETCOR MAS NMR spectrum for hydrated silica-alumina modified with $^{13}\text{CH}_3\text{ReO}_3$ (1 wt.% Re) (RT, mixing time 3 ms, spinning speed 12 kHz). The corresponding 1D ^{13}C CPMAS and single pulse ^1H MAS NMR spectra are plotted along their respective axes.

Hydrogen bonding of CH_3ReO_3 to a silanol was shown in section 3.4 to allow a high degree of mobility as indicated by a ^{13}C signal at 20 ppm, which persists under static solid state NMR conditions. These types of interaction are, of course, also expected to occur at low loadings on the hydrated support. For the hydrated sample with grafted CH_3ReO_3 , however, it is observed that all ^{13}C NMR signals are broadened almost completely into the baseline under non-spinning conditions. This more limited mobility may be attributed to steric hindrance caused by surrounding water molecules/clusters, or the possibility that these will result in multiple hydrogen-bonding interactions with the CH_3ReO_3 .

The activity for homometathesis of propylene of CH_3ReO_3 grafted to the hydrated support is rather low. While there is evidence that small traces of water on the otherwise dehydrated silica alumina support can be advantageous for the catalytic activity,¹⁹⁶ the large amount of water (ca 15 wt.%) present on the hydrated support is clearly detrimental to the reaction kinetics. The active site was shown above to arise from interactions of CH_3ReO_3 with the Lewis acid Al sites of the support. DFT calculations show that both water and CH_3ReO_3 may bind at the Lewis acid site in preference to the siloxane, but also the detrimental effect of water in that water binds at the Lewis Acid site in preference to CH_3ReO_3 when the Al is 4-coordinate, Scheme 3-5. Larger amounts of water may, however, block Lewis acidic sites, perhaps by formation of clusters and make them effectively inaccessible to CH_3ReO_3 , which would inhibit the formation of the active site. This is also in agreement with the DFT calculations which show that the Lewis acid site in fact prefers a second water molecule over CH_3ReO_3 along with one water molecule. H-bonding interactions may also be more numerous in the hydrated support which would result in inactive metathesis sites.



Scheme 3-5. DFT-calculated structures and reaction energies for CH_3ReO_3 interacting with an aluminosilsesquioxane cube (representing the silica-alumina surface) in the presence of water. Color scheme: Re (yellow), Al (purple), Si (blue), O (red), C (green), H (white).

Zeolite HY as support. The H-forms of crystalline, microporous silica-aluminas, such as zeolite HY, possess a large number of Brønsted acid sites inside their pore structures, which include bridging OH groups (SiOHAl), unlike the case of amorphous silica alumina, as well as silanols and external surface Si-OH groups, along with exchangeable cations. Several reports in the literature^{20, 146} have examined the encapsulation of CH_3ReO_3 in the supercage of zeolite Y. These authors conclude, based primarily on EXAFS studies, that the favored mode of binding for CH_3ReO_3 in the zeolite arises from the interaction of an oxorhenium with an extra-framework cation or a proton site. This interaction is confirmed by the NMR results presented below and the formation of this site is also linked to the metathesis activity.

The ^1H MAS NMR spectrum of the acidic form of zeolite Y (HY) for the as-received (hydrated) sample is shown in Figure 3-23a. It consists of a single peak at 4.5 ppm which is assigned to Brønsted acid sites (bridging hydroxyls) and contributions from physisorbed water, water bound to Lewis acidic site, and H-bonded to terminal silanol groups.¹⁵⁴ Upon calcination (at 450 °C, 12 h in oxygen) the ^1H NMR spectrum (Figure 3-23b) is dominated by a peak at 1.6 ppm which represents the non-acidic, terminal (external and internal) Si-OH groups, as well as small peaks between 4 and 5 ppm for the bridging hydroxyl groups and extra-framework AlOH at around 2.5 ppm.¹⁹⁷

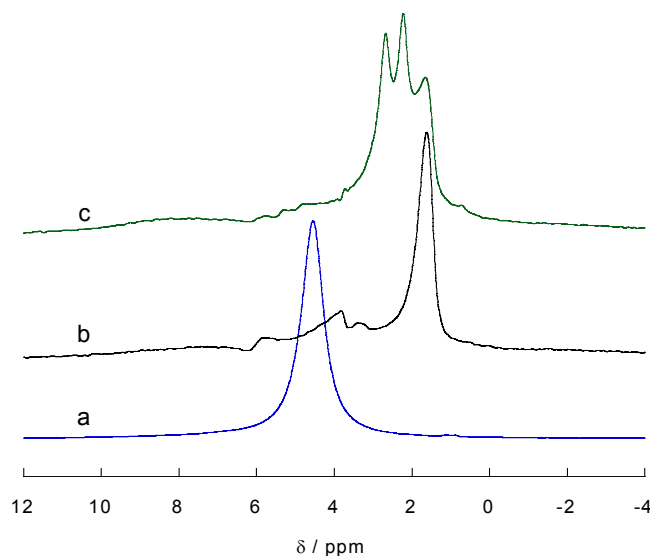


Figure 3-23. ^1H single-pulse MAS NMR spectra for zeolite HY: (a) hydrated, as-received, (b) calcined and (c) $^{13}\text{CH}_3\text{ReO}_3$ -grafted (6 wt.% Re) (RT, 12 kHz).

When CH_3ReO_3 (6 wt.% Re) is adsorbed in the calcined zeolite two additional ^1H signals appear at 2.2 ppm and 2.7 ppm. This doublet may then be assigned to H-bonded protons of terminal silanols with $\text{SiOH-O}_3\text{ReCH}_3$ interactions, similar to the grafting sites on silica (section 3-4). The ^{13}C MAS NMR spectrum of zeolite HY with adsorbed CH_3ReO_3 , on the other hand, surprisingly resembles that for CH_3ReO_3 grafted onto amorphous silica-alumina, and shows similar

characteristics. For example, both peaks at 18 ppm and 33 ppm remain upon evacuation (> 24h) at room temperature. Under static conditions the signal at 33 ppm is broadened into the baseline whereas the peak at 18 ppm persists and therefore indicates a highly mobile species.

The 2D $^{13}\text{C}\{^1\text{H}\}$ HETCOR spectrum in Figure 3-24. shows strong intensity correlation between the ^{13}C signal at 18 ppm and the average of the ^1H signals at 2.2 and 2.7 ppm, which unambiguously confirms the assignment of the signal at 18 ppm to CH_3ReO_3 hydrogen-bonded to Brønsted acid sites. DFT calculations support this assignment scheme despite the fact that binding of CH_3ReO_3 to the bridging silanols is appreciably stronger ($\Delta E = -44$ kJ/mol) than binding to the terminal silanols. The carbons at 33 ppm show very weak correlation to protons at ca. 3 ppm with the chemical shifts resembling CH_3ReO_3 in its bulk form (Chapter 3-1., ^1H MAS: 3.7 ppm, ^{13}C MAS: 34 ppm).

Investigations of the reaction kinetics show very low propylene conversion for CH_3ReO_3 in zeolite Y which is in agreement with the presence of a very small number of available Lewis acidic sites previously shown to be necessary for the formation of the active site. The majority of the ^{13}C peak at 33 ppm is therefore assigned to the agglomeration of CH_3ReO_3 trapped inside the channels of zeolite HY to form small clusters of bulk CH_3ReO_3 . These crystallites would be able to sustain prolonged vacuum desorption and do not contribute to the catalytic activity.

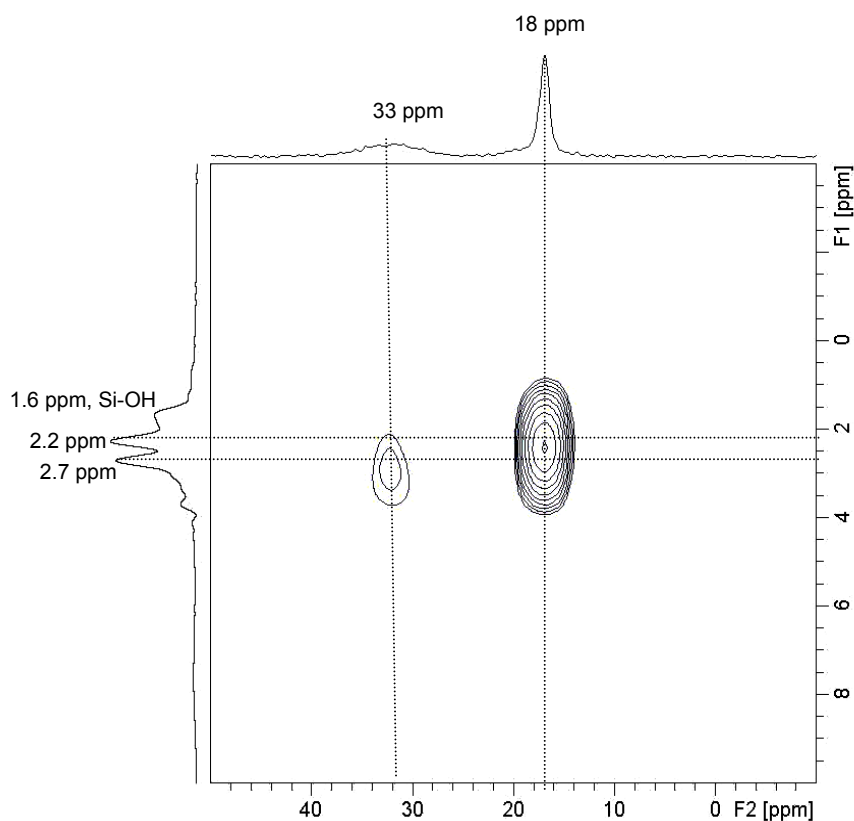


Figure 3-24. Two-dimensional $^{13}\text{C}\{^1\text{H}\}$ HETCOR MAS NMR spectrum for zeolite HY modified with $^{13}\text{CH}_3\text{ReO}_3$ (6 wt.% Re). (RT, mixing time 3 ms, spinning speed 12 kHz). The corresponding 1D ^{13}C CPMAS and single pulse ^1H MAS NMR spectra are plotted along their respective axes.

Al-MCM41 and Al-SBA16 supports. Mesoporous aluminosilicates possess very high surface areas, a narrow pore size distribution and an ordered arrangement of the mesopores, which is hexagonal for Al-MCM41 and cubic for Al-SBA16, but unlike zeolites their walls are amorphous. They can possess both Brønsted and Lewis acid sites whose numbers are dependent on the Si/Al ratio and the method of synthesis.¹⁹⁸ In preliminary studies the reaction kinetics for propylene conversion were carried out for Al-MCM41 and Al-SBA16 (Si/Al=10) loaded with 1 wt.% CH_3ReO_3 . Neither of these materials show appreciable propylene metathesis activity which again must be attributed to a lack of Lewis acidity.

The above results may be summarized with the unambiguous conclusion that amorphous silica-alumina does not only act as catalyst support in this case, but is in fact the activator of CH_3ReO_3 , which otherwise cannot catalyze olefin metathesis. Indeed, many of the unique properties of silica-alumina as a catalyst support arise because it is neither an admixture of silica and alumina nor a poorly ordered aluminosilicate, but a solid solution that possesses both strong Lewis acidity (unlike silica) and strong Brønsted acidity (unlike alumina) without charge-compensating/exchangeable cations.

Silica-alumina is the support for CH_3ReO_3 which gives by far the highest activity for propylene homometathesis compared with that of other oxides, such as alumina and niobia. The latter show only low conversion in preliminary kinetic studies, which can be attributed to the absence of strong acidity compared with silica-alumina. The somewhat more regular structure of mesoporous silica-aluminas did not turn out to be an asset for higher propylene metathesis activity. Crystalline silica-aluminas such as zeolite HY, which contains very strong Brønsted acid sites, but much less Lewis acidity, also show low activity compared with amorphous silica-alumina.

Chapter 4

Results and Discussion

Semiconducting InGaP Nanoparticles

4.1 Surface passivation and physical properties (^{13}C MAS NMR, TEM, photoluminescence)

Extensive series of NMR and related measurements were carried out to investigate the complex structural relationships of photoluminescence (PL) of InGaP nanocrystals with its surface layers, and the effect of etching treatments of the crystals. ^{13}C MAS NMR measurements confirm that hexadecylamine (HDA, $\text{H}_2\text{N}-\text{C}_{16}\text{H}_{33}$) is the passivant layer before as well as after etching. The α -, β - and γ -carbon signals in free HDA appear at chemical shifts of 42.5, 34.4 and 27.0 ppm, respectively.⁷⁵ The solid state ^{13}C NMR spectrum in Figure 4-1. shows these carbon resonances to be broadened and poorly resolved because of overlapping peaks from the methylene carbons between 29 and 32 ppm. The broadening of the α -, β - and γ -carbons signals in the nanocrystals samples is consistent with the presence of hindered rotation combined with a chemical shift distribution from binding to the surface of the particle. The rate of rotation in the HDA chain increases when moving down the chain towards the methyl group. This effect is evidenced by two narrow signals at 25 and 16 ppm which represent carbon number 15 and the methyl carbon, respectively.

The size of the nanoparticles is confirmed by TEM images and size-dependent absorbance spectra. Image 4-1. shows the TEM images of 4.5 nm InGaP nanocrystals that are (a) unetched and (b) etched in HF. The HF treatment of the unetched particles may cause a slight decrease in the number of surface atoms and size of the particle, but no significant change in size is observed with TEM.

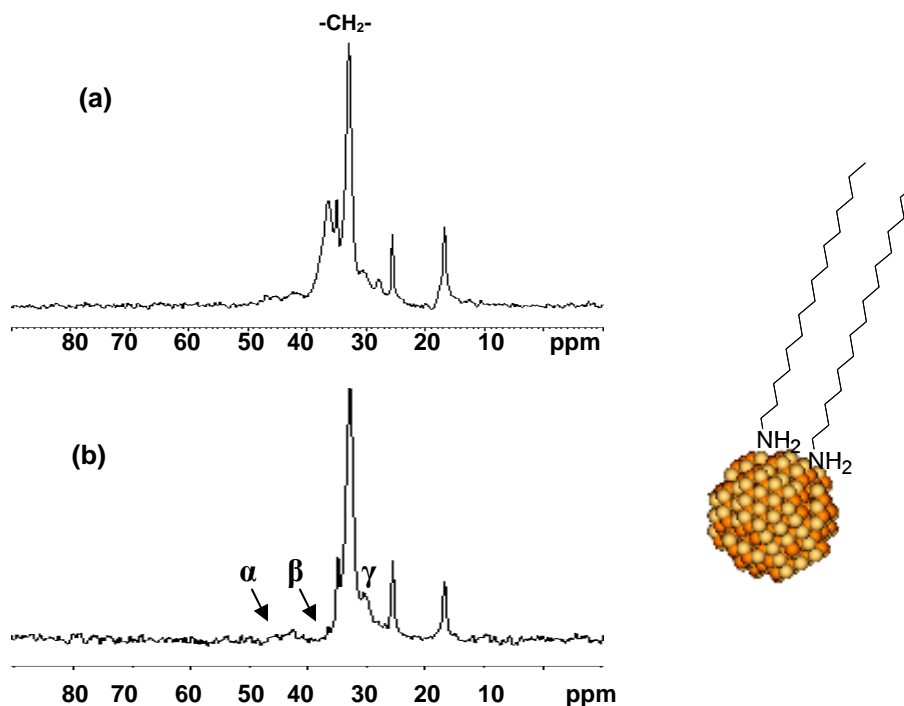


Figure 4-1. Solid state ^{13}C single-pulse spectra of HDA-capped InGaP nanocrystals recorded under MAS at 12 kHz for the (a) unetched and (b) HF-etched sample.

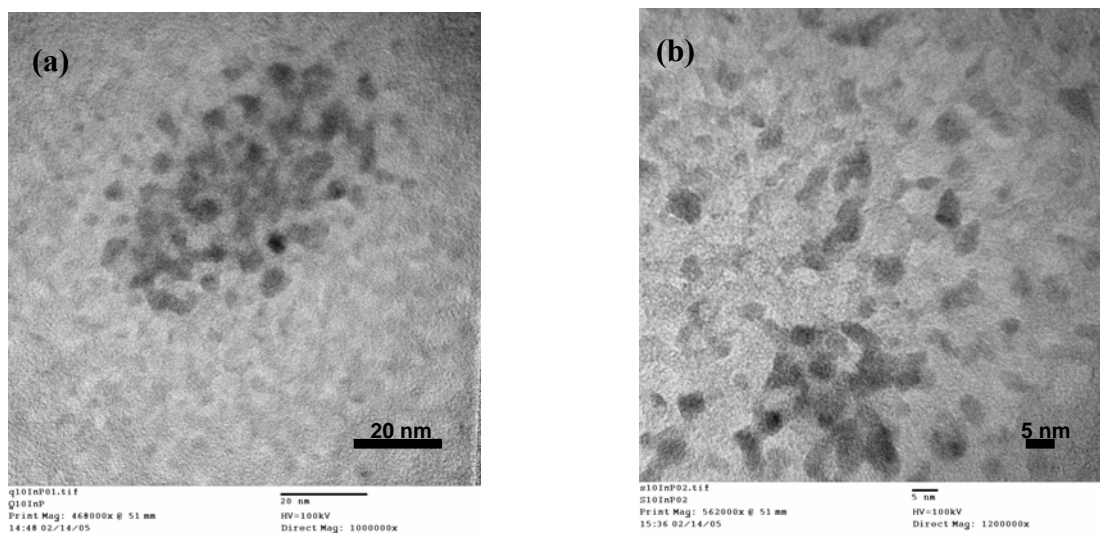


Image 4-1. TEM images of (a) unetched and (b) etched 4.5 nm-sized InGaP nanocrystals. Beam damage and sample aggregation cause the decreased quality of the images.

The PL quantum yields of as-synthesized ternary InGaP nanoparticles are modest, but can be significantly enhanced by treating the particles with HF in methanol. Figure 4-2. shows an overview of the optical properties of the 4.5 nm-sized InGaP nanoparticles before and after the etching treatment. The optical absorbance spectrum of the etched nanoparticles exhibits a small blue-shift and broadening in comparison to the unetched particles. More striking, however, is the increase in photoluminescence quantum efficiency after the HF treatment. While the unetched particles exhibit no detectable PL in toluene, the etched particles show an emission peak at ca. 570 nm with a PL quantum efficiency of 50% upon excitation at 420 nm. After HF-treatment, the PL quantum yields of ternary $\text{In}_{0.91}\text{Ga}_{0.09}\text{P}$ nanoparticles approach those sought for optoelectronic device applications, for which quantum efficiencies above 50% are often required for commercial cost-effectiveness.

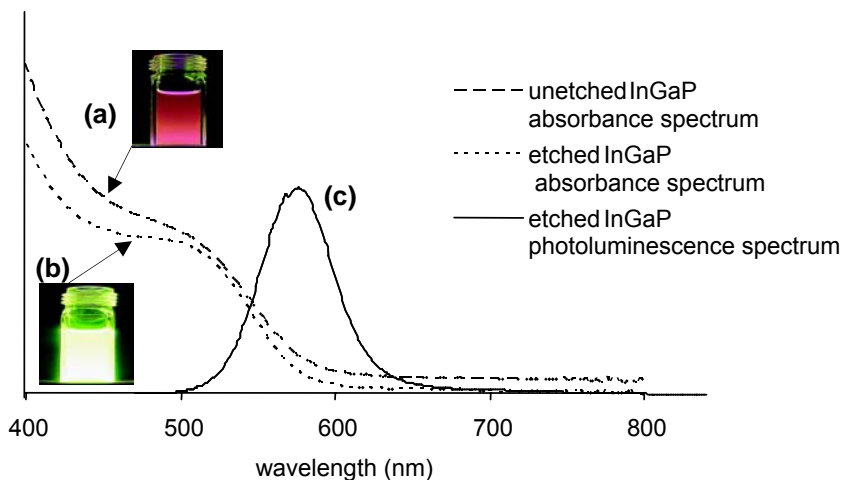


Figure 4-2. Optical absorbance spectra of 4.5 nm $\text{In}_{0.91}\text{Ga}_{0.09}\text{P}$ nanoparticles (a) as-synthesized and (b) after HF etching. Optical images of the nanoparticles in toluene accompany the respective spectra. (c) shows the emission spectrum ($\lambda_{\text{exc}} = 420$ nm) of the same etched sample as in (b).

4.2 Total phosphorous site identification (^{31}P MAS NMR)

The identity of the phosphorous sites in the material were determined by means of ^{31}P MAS single-pulse NMR spectra of the unetched and etched InGaP nanocrystals, as shown in Figure 4-3. The spectra for the two materials are very similar with ^{31}P NMR peaks at 24, 1, -9 (shoulder) and -210 ppm.

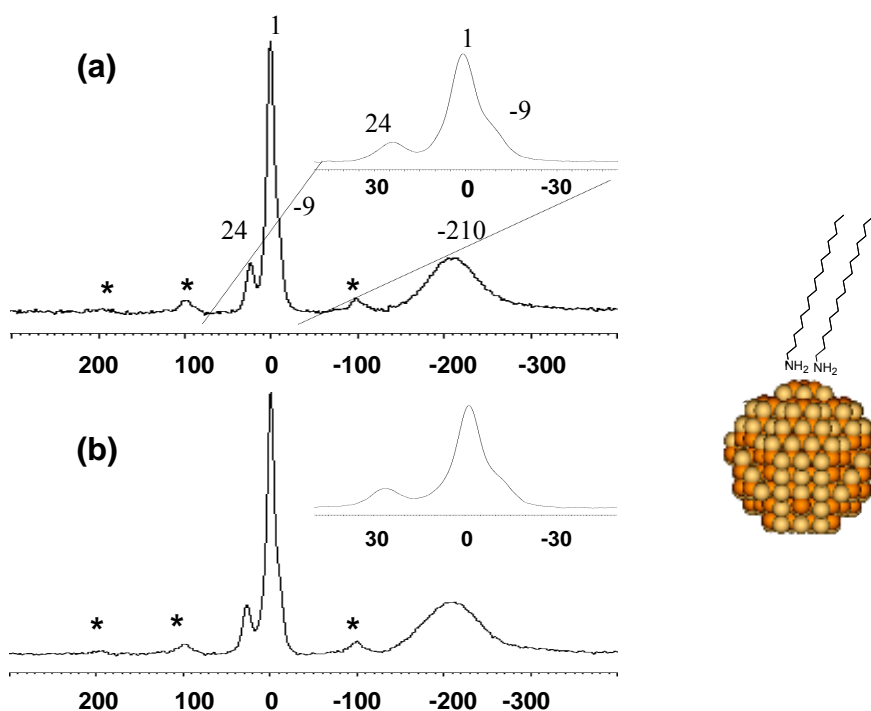


Figure 4-3. Solid state ^{31}P single-pulse spectra recorded under MAS conditions (12 kHz) for (a) unetched and (b) HF-etched InGaP nanocrystals. The insets show the magnified peak at 1ppm with the shoulder at -9 ppm. The spinning sidebands are marked with *.

The ^{31}P peak at -210 ppm can be assigned to core (interior) ^{31}P sites occupying a tetrahedral lattice site bound to either In or Ga in the zincblende lattice of the InGaP quantum dots on account of its chemical shift and line width, as those for bulk InP and GaP have been observed at -147 and -142 ppm, respectively.^{199, 200}

The upfield shift for the tetrahedral ^{31}P sites in the nanocrystal relative to that in the bulk material can be correlated with the size of the nanoparticles, which exhibit an increasing upfield shift with decreasing dot size.^{83, 201} The broad linewidth of the -210 ppm peak (fwhm 60 ppm) is likely to arise from a distribution of chemical shifts from different sites as well as exchange interactions with the nearby quadrupolar indium and/or gallium nuclei, which have also been reported for bulk InP and in InP nanocrystals.^{83, 200}

The three downfield ^{31}P resonances at 24 ppm, 1 ppm and -9 ppm can be attributed to oxidized phosphorus sites located mostly on or near the surface. This assignment is based upon previously reported chemical shifts, the observation that these lines grow in intensity with time when exposed to air, along with the well known presence of a relatively thick native oxide in bulk, nanocrystalline and micron-sized InP.^{61, 83, 89, 91, 102-109} The formation of oxides is further supported by the appearance of spinning side bands for those three ^{31}P resonances. They result from an asymmetrical electron density around the phosphorus sites which is caused by breaking of the tetrahedral symmetry following oxidation.

The differences in the oxide population for unetched and etched InGaP samples and the changes in oxidation over time were investigated by comparing the integrated peak intensities of the three phosphorus sites combined (24, 1, and -9 ppm and corresponding spinning sidebands) and of the peak at -210 ppm. For the initial ^{31}P MAS experiment the materials were used directly after drying, ground to a fine powder (for stable MAS spinning) and packed into a rotor in air. For the time-dependent oxidation studies the samples were stored under argon and only briefly exposed to air during the sample packing. The freshly prepared

materials exhibit a relative population of oxidized to tetrahedral phosphorous sites of 1:1.15 and 1:1.11 (± 0.05) for the unetched and etched particles, respectively. After two months the integration of the signals from the oxidized to internal phosphorus sites had changed to 1:0.79 and 1:0.82 for the unetched and etched samples, respectively. No changes in peak position for the four sites were observed over this time period. The air-stable samples were exposed to air only for a brief period, and oxidation occurred slowly. The lack of controlled O₂ concentration, however, does not allow the kinetics of the process to be analyzed. These experiments were repeated on various samples, and in all cases a larger number of oxidized phosphorous sites was observed following wet-chemical etching in air as well as a time-dependent increase in oxidized phosphorous sites. It is interesting to note that no significant change of size was observed in the TEM spectra, or of the absorption properties, or the size-dependent chemical shift of the -210 ppm phosphorous peak. These findings suggest that the oxidation is primarily occurring on the surface of the particle and that the oxide layer lies within only the top few monolayers. This observation adds to the support of the assignment of the tetrahedral phosphorous sites (peak at -210 ppm) to the core of the nanoparticle and that of the oxidized phosphorous sites to the outermost layers of the nanocrystals.

The nature of the oxidation process on a nanomaterial therefore appears to differ from that of the bulk, where the native oxidation thickness is nearly equivalent to the radius of the nanoparticle, namely ~ 2 nm. Based on this comparison one would predict complete oxidation of the particle with a loss of optical properties with time.²⁰² The lack of a native oxidation thickness in the nanocrystal compared to bulk may arise from the presence of strain on the surface or differences in the nature of the oxide at the surface.

4.3 Surface phosphorous oxidation sites identification

2D $^{31}\text{P}\{^1\text{H}\}$ HETCOR MAS NMR. Further information on the nature of the oxides at the surface, as well as the identity of the species represented by the various ^{31}P resonances in the InGaP nanocrystals, was obtained by the use of 2-dimensional $^{31}\text{P}\{^1\text{H}\}$ frequency-switched-Lee-Goldberg (FSLG) HETCOR NMR. The dependence of the cross polarization on interatomic distance was used in the pulse sequence to carry out depth profiling of the material. The $^{31}\text{P}\{^1\text{H}\}$ FSLG HETCOR NMR spectra of unetched InGaP, with CP contact times of 2 and 15 ms are shown in Figure 4-4a and b. The HETCOR spectra of the unetched and etched InGaP nanocrystals are nearly identical and therefore only the spectrum for the unetched sample is presented here.

The ^1H NMR peaks between ~0 and 3 ppm on the vertical axis in Figure 4-4. correspond to the protons of the HDA passivating layer. Strong correlations between the ^{31}P resonances at 24 ppm and 1 ppm with the protons of the HDA chain centered at 1.6 ppm are evident in Fig. 4-4a. At this mixing time (2 ms) no correlation between the HDA protons and the phosphorous sites at -210 ppm are observed. This suggests that the oxidized phosphorous sites at 24 and 1 ppm are in close spatial proximity to the protons on the passivating ligands. It is not apparent, however, if there is a correlation between the HDA protons and the peak at -9 ppm because of the overlap with the peak at 1 ppm. From the observed correlations it can be concluded that the passivating layer is interacting strongly with at least two of the sites corresponding to the oxide ^{31}P peaks, which confirms that these are surface oxides, rather than core-oxidation or impurities in the sample.

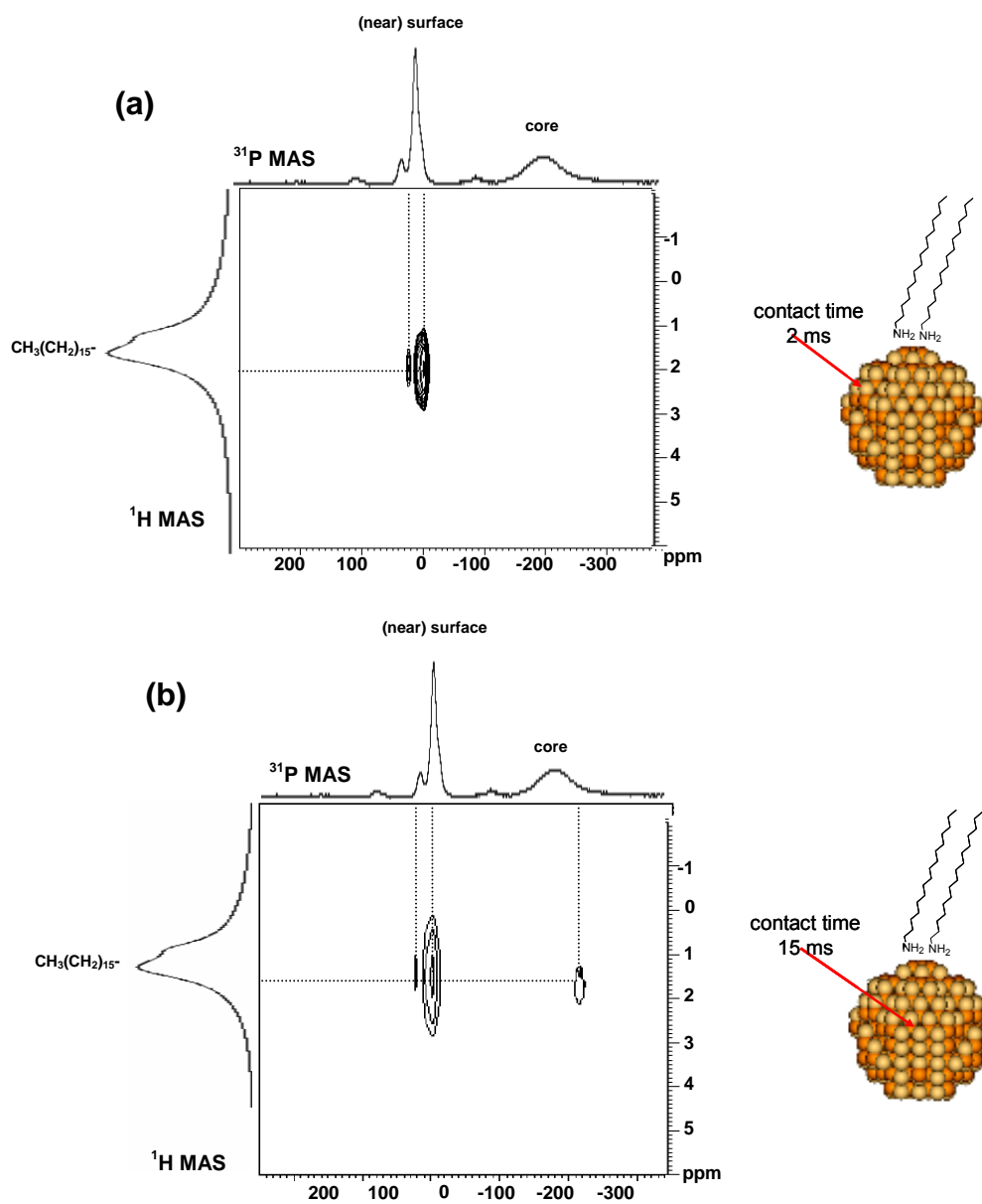


Figure 4-4. $^{31}\text{P}\{^1\text{H}\}$ FSLG HETCOR spectra of unetched InGaP nanocrystals recorded under MAS at 12 kHz with CP contact times of (a) 2ms and (b) 15ms. The respective single pulse ^{31}P MAS and ^1H MAS spectra are plotted along the horizontal and vertical axes.

Weaker dipole-dipole couplings and thus longer distances between two nuclei can be observed with longer contact times. An increase in contact time to 15 ms (Figure 4-4b) results in the transfer of magnetization of the protons to more

distant (interior) ^{31}P sites and thereby gives rise to a correlation with the core peak at -210 ppm, which reflects the depth profile of the material.

^{31}P CPMAS NMR. The HETCOR NMR data in combination with the ^{31}P resonance positions clearly establish the formation of an oxide layer at the surface of the nanoparticle. No significant change in the intensity between the oxidized and unoxidized phosphorous sites in either the ^{31}P MAS or HETCOR data was detected, which leads to the conclusion that the thickness of the oxidation layer and identity of the sites are the same. An extensive review of the chemical shifts reported in the literature as well as measurements of the ^1H - ^{31}P cross-relaxation time constants provide further insights on the nature of the phosphorus sites. Many studies to date have utilized XPS to characterize the oxidation species of bulk InP, where the oxidation species on the surface of the InP crystals have been identified as InPO_4 and InPO_3 as well as In_2O_3 .^{102, 104-109} Wilmsen *et al.*¹⁰⁹ summarize the oxidation of bulk III-V semiconductors and identify the thermal oxidation species of GaP to be predominately GaPO_x with the possibility that Ga_2O_3 occurs primarily at high temperatures. These XPS studies on bulk materials suggest a likely assignment of the phosphorus species at 24 ppm to be PO_3 . A study by Bujoli-Doeuff *et al.*²⁰³ strongly supports this conclusion with a measured ^{31}P chemical shift of 25.6 ppm for $\text{Ga}(\text{OH})(\text{O}_3\text{PCH}_2\text{C}_6\text{H}_5)$. The resonances at 1 and -9 ppm are then most likely due to PO_4 resonances. Recently, Kulshreshtha *et al.*²⁰⁴ have measured the ^{31}P NMR chemical shift of bulk GaPO_4 at -8.5 ppm, while Tomaselli *et al.*⁸³ have found a surface $^{31}\text{PO}_4$ resonance at 5 ppm for InP quantum dots passivated by trioctylphosphine oxide. These results suggest that the phosphorous sites for the 1 ppm and -9 ppm signals arise from PO_4 species. The slight differences in chemical shift from those in the literature can readily be attributed to ligand

effects and the mixed metal (gallium and indium) $^{31}\text{PO}_4$ species in the ternary InGaP particles.

Further analysis of the nature and depth of oxidation of the phosphorus sites can be gained from measurements of the ^1H - ^{31}P cross-relaxation time constants, T_{PH} . The values of the ^1H - ^{31}P cross-relaxation time constants have a dependence on the interatomic distance R of $1/R^6$ and can thus be used to compare distances between ^1H and ^{31}P nuclei.²⁰⁵ A closer spatial proximity of the ligand protons to the phosphorus sites will give stronger dipole-dipole couplings so that the maximum integrated peak intensity for CPMAS will be reached at a shorter contact time and yield lower values of T_{PH} . The cross-relaxation time constant was calculated by ^1H - ^{31}P cross polarization magic angle spinning measurements with varying contact times between 0.1 and 20 ms.

^{31}P CPMAS spectra of unetched InGaP nanocrystals with mixing times of 2 and 15 ms (Figure 4-5.) demonstrate representative changes in signal intensity with differences in the distance-dependent ^1H - ^{31}P contact times. As in the HETCOR section above only the spectra for the unetched InGaP nanocrystals are shown because of the similarity of the data for the etched samples.

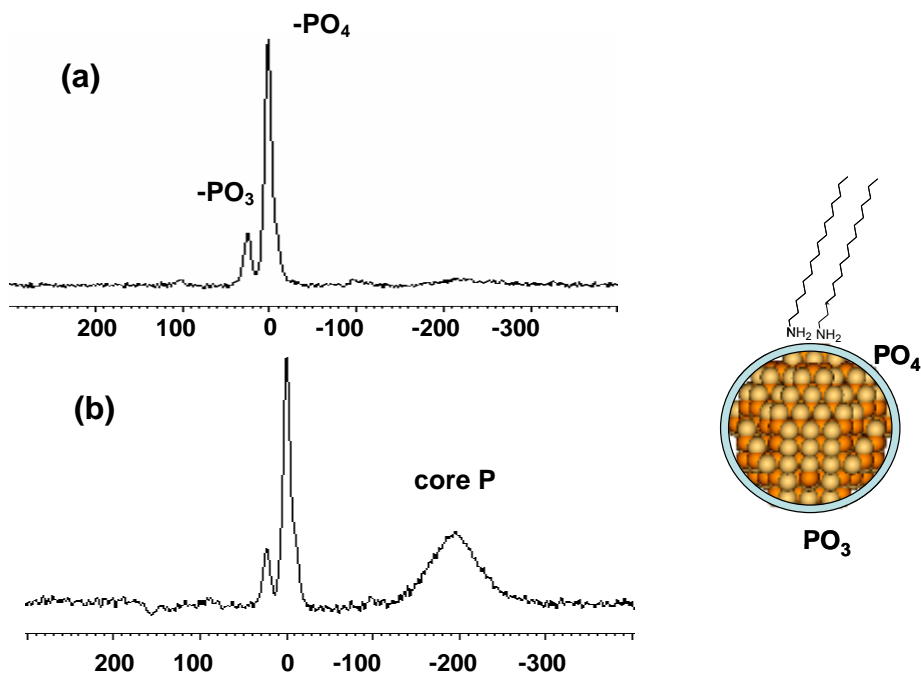


Figure 4-5. ^{31}P CPMAS spectra of unetched InGaP nanocrystals recorded with CP contact times of (a) 2 ms and (b) 15 ms and a spinning speed of 12 kHz.

The integrated ^{31}P peak intensities from ^1H - ^{31}P CPMAS spectra were plotted as a function of the various contact times τ and show that the signal intensity, $M(\tau)$, passes through a maximum and then falls off exponentially with increasing τ . The value of T_{PH} is common to all ^{31}P atoms and was determined by fitting, $M(\tau)$ to Equation 4-1. using a nonlinear least-squares analysis.²⁰⁶

$$M(\tau) = M_0(\exp(-\tau/T_{1\rho\text{H}}) - \exp(-\tau/T_{\text{PH}}))/(1 - T_{\text{PH}}/T_{1\rho\text{H}}) \quad (\text{eq 4-1.})$$

The proton spin-lattice time constant, $T_{1\rho}$, was determined following a procedure from Voelkel.²⁰⁷ The resulting plots and fitted values are shown in Figure 4-6. and Table 4-1., respectively.

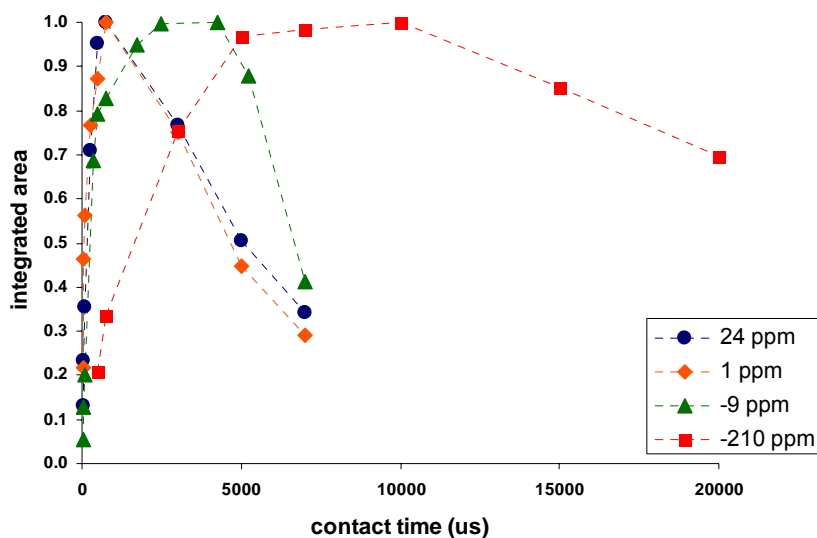


Figure 4-6. Plots of the integrated ^{31}P peak intensities from ^1H - ^{31}P CPMAS measurements as a function of CP contact times for the phosphorous peaks at 24 ppm, 1 ppm, -9 ppm and -210 ppm. The connecting lines are drawn to help the eye.

Table 4-1. InGaP nanocrystal ^1H - ^{31}P cross-relaxation time constants, T_{PH} , for the various ^{31}P peaks determined from a least-square analysis of the data in Figure 4-6.

^{31}P peak (ppm)	T_{PH} (ms) \pm 0.5
24	1.5
1	1.5
-9	3.8
-210	12

The PO_3 and PO_4 sites at 24 and 1 ppm have identical CPMAS build-up curves and the lowest T_{PH} values (1.5 ms) of all the phosphorus sites. This supports the assumption that these phosphorous sites are on the surface of the particle and at approximately the same distance from the protons of the HDA chain. The CPMAS curve for the PO_4 species at -9 ppm, on the other hand, exhibits a slower build-up and has a higher T_{PH} value of 3.8 ms. The slower build-up for the same

nuclear species indicates that the corresponding phosphorous site is at a lower depth relative to the protons of the HDA chain which in turn suggests that some oxidation also occurs within the particle. The much longer build up time (12 ms) for the peak at -210 ppm would then lead to the conclusion that no oxidation is occurring in the core of the particle and that the oxide formation on the particle surface terminates at some finite depth. The differences in chemical shifts of the $^{31}\text{PO}_4$ sites corresponding to the 1 ppm and -9 ppm signals may then be inferred to stem from sites at different depths relative to the HDA passivant (with the -9 ppm site occurring deeper) rather than segregated InPO_4 and GaPO_4 species on the surface.

Given the characterization of the oxidation sites as PO_4 and PO_3 an integration of the resonances for these ^{31}P species can then be used to determine the relative amounts of phosphorus in these sites, as well as their rate of growth. It is of interest to note that the rate of growth of PO_3 is faster than PO_4 both in the unetched and etched samples, where the etched sample originally had a slightly higher amount of PO_4 . Approximately three months after synthesis, however, the ratio of PO_3 to PO_4 for the unetched and etched samples was very close, namely 1:6.5 and 1:6.0, respectively.

Spatial proximity of PO_4 and PO_3 on the surface (2D DQ $^{31}\text{P}\{^{31}\text{P}\}$ MAS NMR).

More detailed information on the positions of the PO_4 and PO_3 sites on the surface of the InGaP nanomaterials can be obtained from 2D dipole-dipole mediated solid state double quantum (DQ) ^{31}P NMR. Since the creation of a double quantum coherence (DQC) between two ^{31}P nuclei relies on a sufficiently strong dipole-dipole coupling between them, it provides information about through-space ^{31}P - ^{31}P connectivities. If two phosphorus sites are in close

proximity in the material, they will share the same double-quantum frequency, which is the sum of the single quantum frequencies of the two nuclei involved. Thus, DQC signals between the same phosphorus sites appear as so-called auto peaks on the diagonal of the DQ spectrum, while those of different phosphorous sites appear as so-called cross peaks. The spectrum of the unetched sample is shown in Figure 4-7.

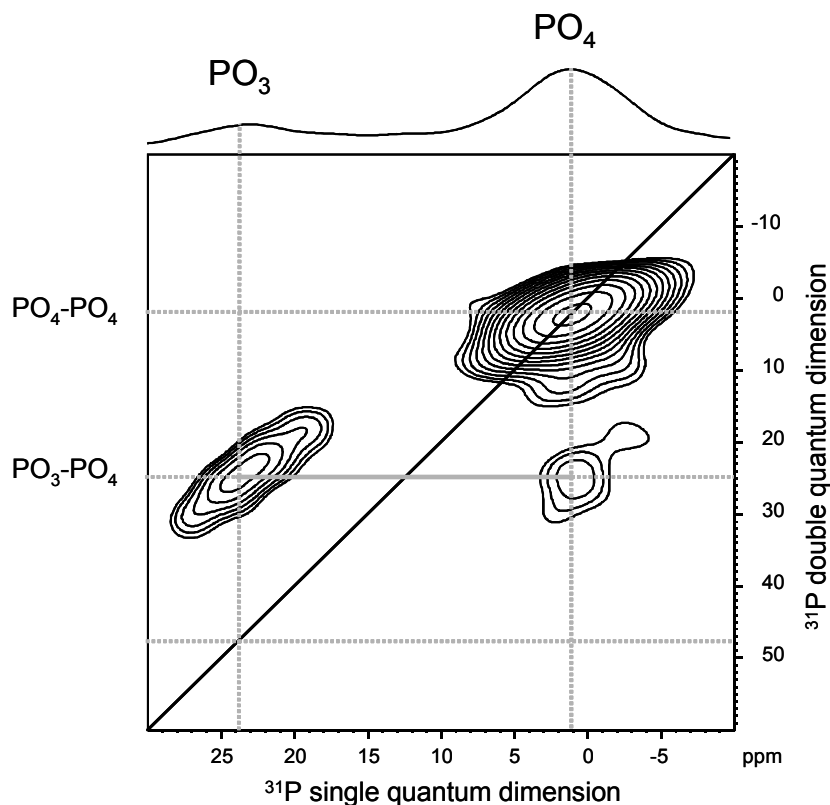


Figure 4-7. 2D Double Quantum ^{31}P $\{^{31}\text{P}\}$ NMR spectrum of unetched InGaP nanocrystals recorded under MAS at 12 kHz and an excitation time of 1.66 ms. The one-dimensional spectrum plotted at the top is the sum projection of the single quantum dimension.

The sum-projection of the single quantum dimension is shown at the top of the spectrum. Since the BABA pulse sequence must be acquired with rotor-synchronization, the spectral width in the indirect dimension is limited by the spinning speed.¹⁴⁴ Even at 30 kHz MAS the spectral width would be too small to cover the entire ^{31}P spectrum. Only the surface ^{31}P sites were therefore

investigated, while the bulk ^{31}P resonance at -210 ppm was eliminated by employing cross polarization with a contact time of 2 ms. In this manner possible fold-over effects of the bulk ^{31}P resonance can be prevented, while the cross polarization circumvents long ^{31}P T_1 relaxation times and allows for a much shorter recycle delay.

The close proximity of PO_4 and PO_3 species is revealed in the DQ spectrum shown Figure 4-7. by the cross peaks at a double quantum frequency of 25 ppm, marked with a solid grey connecting line. Also present is an auto peak at a DQ frequency of 2 ppm which indicates a close spatial proximity of PO_4 with other PO_4 sites. The shoulder at -9 ppm, as observed in the single-pulse experiments (Figure 4-3.), is not well enough resolved in the DQ spectrum so that no conclusions can be drawn about other possible spatial proximities to other ^{31}P sites. If PO_3 sites were in close proximity to each other, an auto peak at a double quantum frequency of 48 ppm would be expected, which is not observed. The 2D solid state double quantum ^{31}P NMR analysis therefore indicates that PO_4 sites are in close proximity to PO_3 as well as other PO_4 sites, but not PO_3 to other PO_3 sites. These observations lead to the conclusion that the PO_3 sites must be surrounded by PO_4 sites. The PO_4 species must therefore be the predominant oxidation species seen in the MAS spectra. More importantly, the PO_3 sites in turn cannot be occupying a specific face, step-edge, or exist as a phase segregated domain. The PO_3 site is therefore most likely a partial oxidation site on the surface, or possibly on a vertex on the nanocrystal, while PO_4 species are present on the surface, as well as within the quantum dot.

In conclusion, Table 4-2. summarizes the assignments of the ^{31}P peaks. Solid state NMR experiments provide vital information on the nature of the structure and

surface oxidation of InGaP nanocrystals. Analysis of the NMR experiments indicate that oxidation is primarily a surface process and is constrained to the outermost layers in both unetched and HF-etched nanoparticles.

Table 4-2. Summary of ^{31}P site assignments, positions and characterization methods for unetched and HF-etched InGaP nanocrystals.

^{31}P chemical shift	Species assignment	Position	Characterization methods
24 ppm	PO_3	surface	^{31}P MAS integration in time, bulk InP and GaP oxidation products, chemical shift correlation with Ga phosphonate materials, HETCOR, shortest (same as 1 ppm) T_{pH} value from CPMAS data
1 ppm	PO_4	surface	^{31}P MAS integration in time, bulk InP and GaP oxidation products chemical shift correlation with GaPO_4 and $^{31}\text{PO}_4$ on InP nanocrystals, HETCOR, shortest (same as 24 ppm) T_{pH} from CPMAS data
-9 ppm	PO_4	near surface	^{31}P MAS integration in time, bulk InP and GaP oxidation products chemical shift correlation with GaPO_4 and $^{31}\text{PO}_4$ on InP nanocrystals, HETCOR, shortest (same as 24 ppm) T_{pH} from CPMAS data
-210 ppm	$\text{P}_{\text{tetrahedral}}$	internal	^{31}P MAS chemical shift correlation with InP and GaP, HETCOR, longest T_{pH} from CPMAS data, optical data

The observation of identical surface oxidized species present in both the etched and unetched samples appears to be surprising in light of similar work on bulk InP. Kikuchi *et al.*¹⁰⁶ have shown by means of XPS that chemical cleaning of InP(100) surfaces in aqueous HF solutions removes the native oxide layer and leaves behind a surface terminated by fluorine. For freshly etched nanoparticles, however, ^{19}F MAS NMR suggests only the presence of a very small amount of transient fluoride species with weak NMR signals, while no ^{19}F species could be detected after approximately one month. This suggests that the improved photoluminescent behavior following etching is not the result of fluorine ions at the surface or removal of the oxide layer. The fluoride ion appears to be labile,

with re-oxidation of the particle occurring after exposure to air and the formation of a reconstructed surface, which would indicate this to be the critical process for enhanced photoluminescence.

On the basis of this conclusion the similarity of NMR signals from the unetched and etched oxidized phosphorus sites would point to a tendency of InGaP nanocrystals to oxidize to a specific structure. A further investigation of the gallium and indium sites is therefore necessary for a full understanding of the correlation of structure and quantum efficiency in HF etched and unetched InGaP nanocrystals.

4.4 Indium site occupation (^{115}In spin-echo MAS NMR)

The nature of the indium sites in the InGaP nanocrystals was investigated by means of ^{115}In spin-echo MAS NMR measurements of both the unetched and HF-etched samples (Figure 4-8.).

The spectra extend over a large range of chemical shifts (~ -250 ppm to 1100 ppm) and exhibit a resonance centered at 780 ppm, which is close to the chemical shift (787 ppm) for polycrystalline ^{115}InP powder (bulk InP). This peak at 780 ppm in both spectra can therefore readily be assigned to tetrahedral ^{115}In species coordinated to four phosphorous atoms in the core of the nanoparticles. The downfield shoulder at ~ 890 ppm in both spectra could then possibly be a reconstructed indium site near the oxide layer/core interface. The magnitude of this shift would still suggest tetrahedral coordination to phosphorus for this In

site. Both spectra exhibit broad upfield shoulders ranging from approximately 610 ppm to 250 ppm, which most likely correspond to ^{115}In species in the more distorted environments closer to the surface of the nanoparticle. The upfield signal intensity reflects a distribution of ^{115}In sites that points to partial replacement of phosphorus atoms by oxygen atoms, consistent with upfield ^{115}In . Wilmsen *et al.* report the thermal oxidation species of bulk InP as predominately InPO_x and In_2O_3 ¹⁰⁹ and it is likely that both of these can be found in the present system.

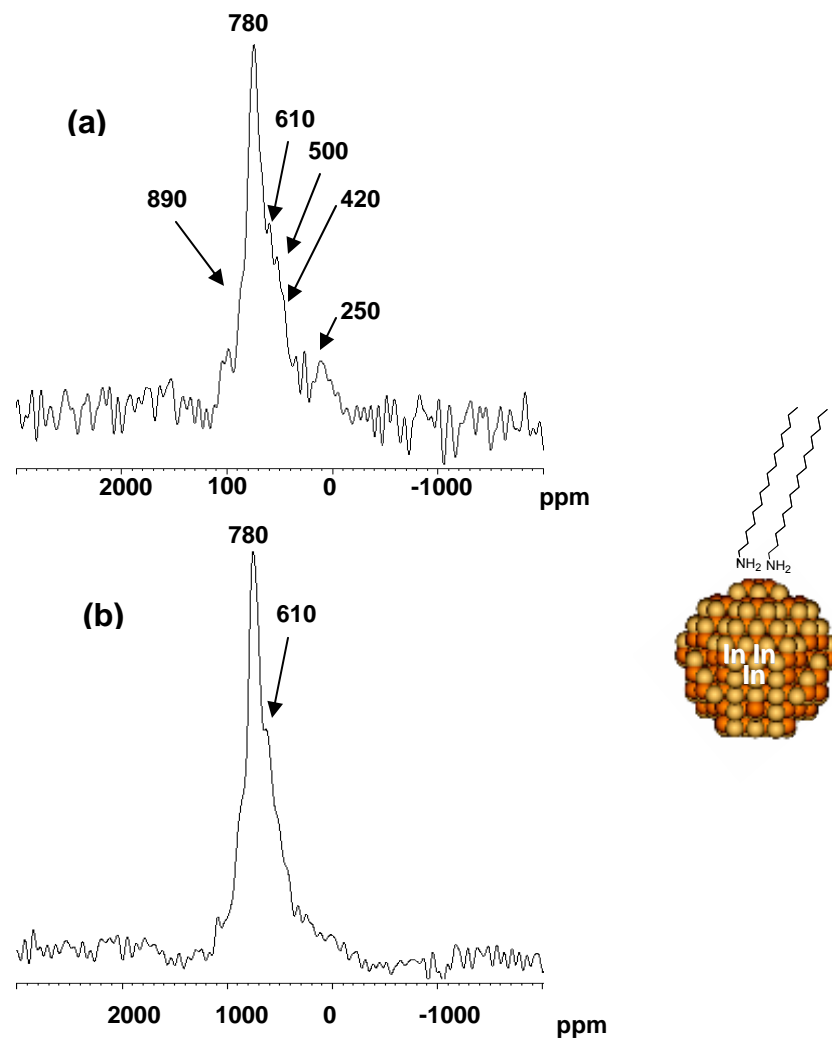


Figure 4-8. Spin-echo ^{115}In MAS NMR spectra of InGaP nanoparticles (a) before and (b) after etching, recorded at a spinning speed of 14 kHz.

It is of interest to note that the ^{115}In spectra are barely influenced by the etching process, which suggests that most ^{115}In species in the particles are closer to the core and farther away from the surface reconstructions that occur upon etching. The ^{115}In MAS NMR spectrum of the etched particles, however, shows a significantly higher sensitivity: fewer scans were necessary in acquiring the spectra despite the smaller amount of material, i.e., unetched: 128,000 scans, 75 mg; HF etched: 96,640 scans, 64 mg. This observation suggests that after the etching process some ^{115}In nuclei can be detected which were “NMR-invisible” prior to etching because of their large second-order quadrupole couplings caused by the distorted environments on the surface. The quadrupolar interactions therefore decrease in response to the more ordered environment created by the etching process and accompanying surface reconstruction. The presence of some indium in these regions is thereby indicated.

4.5 Gallium siting and ordering (^{71}Ga spin-echo MAS NMR)

Very clear changes as a result of the etching procedure are visible in the solid state ^{71}Ga MAS NMR spectra in contrast to the ^{115}In MAS NMR spectra. The ^{71}Ga spin-echo MAS NMR spectrum prior to etching exhibits a strong resonance centered at 300 ppm with a full width at half-maximum of 170 ppm (Figure 4-9.). This resonance corresponds closely to the chemical shift in polycrystalline GaP powder, namely 302 ppm (fwhm 3 ppm). The 300 ppm peak can therefore be assigned to gallium coordinated to four phosphorus away from the nanoparticle surface. A second peak is centered at 25 ppm and extends to a small shoulder at -200 ppm. In view of the fact that the nanoparticles have an oxide layer on the

surface these upfield resonances are most likely to be attributed to ^{71}Ga species in oxide environments near the surface.

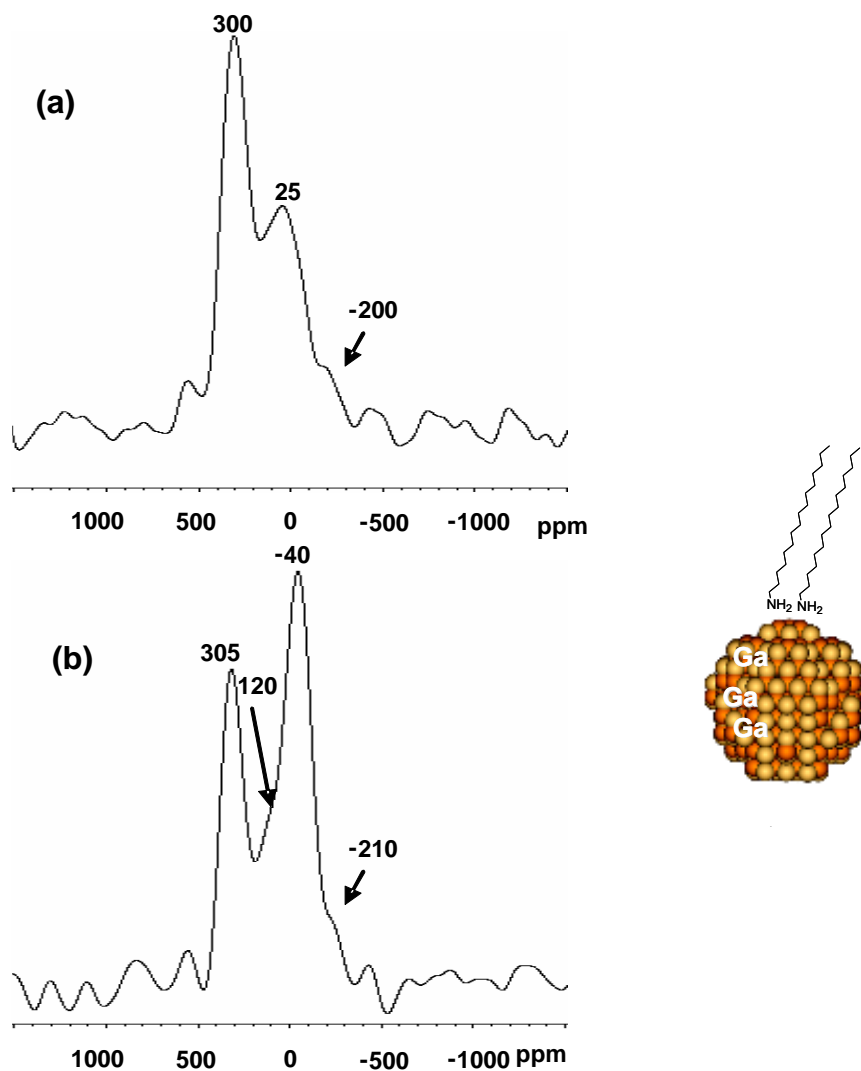


Figure 4-9. Spin-echo ^{71}Ga MAS NMR spectra of InGaP nanoparticles (a) before and (b) after etching, recorded at a spinning speed of 14 kHz.

GaPO_x moieties and to a lesser extent Ga_2O_3 have been found to be the main oxidation products in bulk GaP.¹⁰⁹ Bujoli *et al.*²⁰³ reported chemical shifts of gallium based phosphonate hybrid materials for $\text{Ga}(\text{OH})(\text{O}_3\text{PCH}_3)$ and $\text{Ga}(\text{OH})(\text{O}_3\text{PCH}_2\text{C}_6\text{H}_5)$ of $-13 \text{ ppm} \pm 10 \text{ ppm}$ and $10 \text{ ppm} \pm 10 \text{ ppm}$, respectively.

Tetrahedral and octahedral sites in β -Ga₂O₃ were associated with ⁷¹Ga NMR chemical shifts of 40 ppm and 200 ppm.²⁰⁸ The ⁷¹Ga signal centered at 25 ppm in the InGaP nanocrystals may well contain overlapping peaks of both of these gallium oxidation species, and would therefore be consistent with the NMR results. The peak with a large upfield shift at -200 ppm could conceivably be assigned to some type of reconstructed gallium site which is also bound to an oxidized phosphorus species, such as gallium in a vertex or edge site on the surface.

Significant changes after etching are evident in the spin-echo ⁷¹Ga MAS spectrum (Figure 4-9b). The resonance attributed to gallium coordinated to four phosphorous atoms at 305 ppm shows a significant *decrease* in relative intensity and a smaller linewidth (fwhm 130 ppm). The upfield resonances corresponding to ⁷¹Ga in oxidic environments, on the other hand, shift markedly to -40 ppm with a shoulder at 120 ppm and exhibit a strong *increase* in relative intensity with sharper peaks compared to the spectrum of the unetched sample. The HF treatment of the unetched particles may result in a slight decrease in the number of surface atoms so that a ⁷¹Ga NMR signal which is weaker than in the unetched particles could be expected. A dramatically stronger ⁷¹Ga signal was, however, observed for the etched InGaP nanocrystals despite the smaller sample size (75 mg for etched vs. 64 mg for unetched). Furthermore, the spectrum for the etched sample has a similar signal-to-noise ratio than that of the unetched sample even though it was recorded with approximately a third of the number of scans (81,088 vs. 216,096 scans). This again points to ⁷¹Ga nuclei sited in more ordered “NMR-visible” environments, as the “invisible” gallium sites, which were broadened beyond detection in the unetched particles, become visible and thereby give a stronger signal detected in a much shorter amount of time. An

annealing of surface defects sites and the increase in order resulting from the etching treatment would also be in accord with the smaller linewidths of both resonances in the etched ^{71}Ga MAS NMR spectrum compared with that of the unetched particles.

Since etching with HF is a surface treatment, only surface or near-surface atoms should be affected by the removal of atoms and the associated reconstruction. The significant change in the peaks in the upfield region of the ^{71}Ga spin-echo spectra with etching therefore confirms that these peaks originate from gallium coordinated to the oxidized surface or near-surface.

It can therefore be concluded that the pronounced differences in the effect of the etching process on the ^{71}Ga and ^{115}In spectra clearly suggest that ^{115}In species are predominantly found in the core of the nanoparticles, while ^{71}Ga species are located near the surface and in the oxide surface layer. The etching process leads to reorganization of the nanoparticle surface resulting in annealing of surface defects and producing a more chemically and electronically ordered environment for the ^{71}Ga species. These changes must therefore be closely connected to the increase in photoluminescence quantum efficiency. This conclusion is further supported by findings that nanoparticles prepared by microwave synthesis, which yields particles with a more ordered structure, exhibit enhanced PL quantum efficiencies even prior to HF etching.⁸⁸ Figure 4-10. summarizes the structural changes upon the etching process.

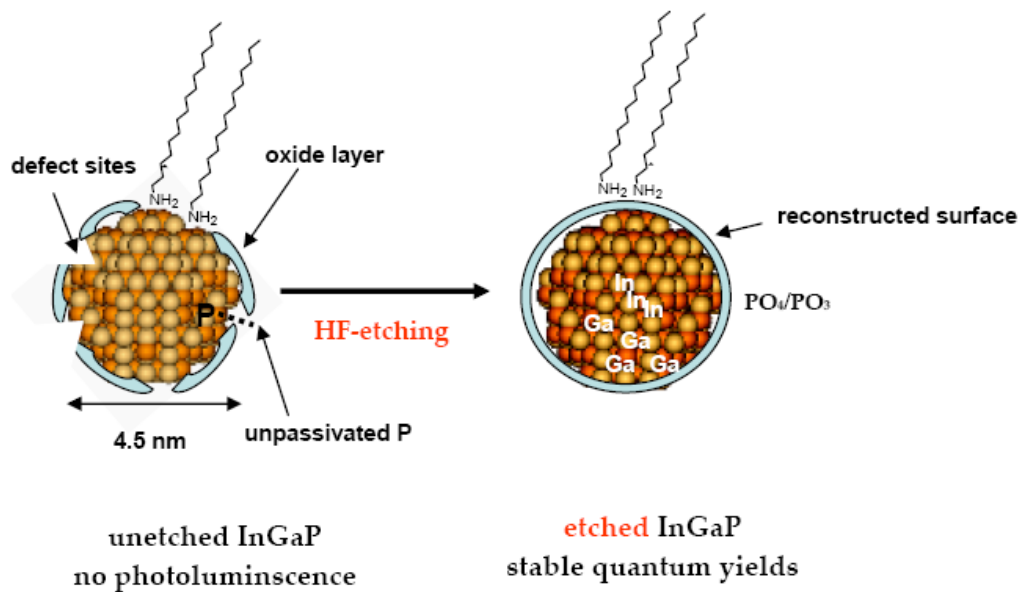


Figure 4-10. Schematic diagram depicting structures and changes produced in 4.5 nm $\text{In}_{0.91}\text{Ga}_{0.09}\text{P}$ nanoparticles by HF surface-etching, which are consistent with the ^{31}P , ^{115}In and ^{71}Ga MAS NMR and optical spectroscopy results.

Chapter 5

Summary and Outlook

This work describes the use of solid state NMR spectroscopy as the primary investigational tool for correlating properties and function to structural features of surfaces and interfaces in two rather different systems of considerable current interest. The first of these concerns a heterogeneous catalyst for olefin metathesis, namely methyltrioxorhenium supported on solid oxide surfaces, and the remarkable property that this inactive organometallic molecule gains catalytic activity upon binding to a particular support, while the second part of this work deals with the correlation of structural aspects of InGaP nanoparticles with their photoluminescent properties.

5.1 Heterogeneous Re catalyst for olefin metathesis

In order for the applications of olefin metathesis to become more widely useful, as well as economically viable, it is essential that new heterogeneous metathesis catalysts are developed with higher activities and stabilities and improved functional-group tolerance. The major challenges to be addressed are to increase the activities of established combinations of metal and support, to prolong the useful lifetimes of working catalyst, to simplify regeneration procedures as well as to modify the active site structures to improve functional-group tolerance as well as resistance to poisoning.

The inspiration for this work came from reports that promoters such as SnR_4 and PbR_4 confer activity on a common low-temperature $\text{Re}_2\text{O}_7\text{-Al}_2\text{O}_3$ catalyst for the metathesis of polar olefins, albeit at the cost of regenerability.³ Calcination of the promoted catalysts results in the formation of an overlayer of SnO_2 or PbO which

prevents reactivation. A molecular-level understanding of the role of the promoter is therefore necessary in order to design activation pathways that do not require the use of Sn or Pb reagents. This may also lead to an extension of the usefulness of these catalysts to substrates such as seed oils, which require mild, liquid phase reaction conditions and tolerance of polar groups. Since this heterogeneous catalyst does not initially possess a carbene ligand, it must spontaneously generate one from the olefin substrate. Herrmann¹⁸ originally speculated that the action of the promoter SnMe₄ on a conventional heterogeneous perrhenate/alumina catalyst involves the formation of *in situ* CH₃ReO₃, which was in fact only recently demonstrated.³⁰

The CH₃ReO₃ molecule, however, is not by itself a catalyst for olefin metathesis, either in solution or in the solid state. It is therefore apparent that it is the interaction between CH₃ReO₃ and the solid oxide surface which conveys activity to the organometallic molecule, and that an understanding of this interaction is the first step towards explaining how heterogeneous rhenium-based catalysts acquire their unique metathesis activity.

Only when CH₃ReO₃ is supported on silica-alumina is this catalyst effective for the metathesis of both simple and functionalized olefins at room temperature, without further thermal or chemical activation.^{18, 19} The identification and structural characterization of the energetically most favored interaction of CH₃ReO₃ with the surface of an amorphous, dehydrated silica-alumina was the first task to be undertaken on samples with low loading of Re (≤1 wt.%) and high Re dispersion. This was accomplished by a synergistic approach which utilized spectroscopic experiments in conjunction with computational modeling. ¹H MAS, ¹³C CPMAS and 2D HETCOR NMR spectra obtained on this system clearly

revealed that the grafted CH_3ReO_3 molecule at this low loading does not interact with the surface silanols, retains the methyl group intact, and that the single species observed has a ^{13}C chemical shift which is intermediate between that of solvated and polycrystalline CH_3ReO_3 . As the spectrum of the grafted CH_3ReO_3 does not exhibit the rather complex shape of the polycrystalline material, it can be concluded that it is indeed molecularly dispersed on the silica-alumina support and thereby not subject to the same quadrupolar interactions. The chemical shift differences between solvated and adsorbed CH_3ReO_3 , on the other hand, clearly reflect an altered electronic environment for the molecule experienced by grafting to the support.

DFT calculations reveal that binding of the CH_3ReO_3 molecule in this favored configuration involves two synergistic Lewis acid-base interactions: one of the oxo ligands of CH_3ReO_3 binds to a Lewis acidic Al site of the silica-alumina surface, while a neighboring framework oxygen (AlOSi) weakly coordinates to Re (Figure 5-1.). An aluminosilsesquioxane monosilanol cube was chosen as a model for the amorphous support and to represent the functional groups (Lewis acid and base, Brønsted acid) present on the surface of amorphous silica-alumina. The aluminum site is capped with a neutral siloxane ligand to model a distorted, four-coordinate Al site, which remains Lewis acidic and binds CH_3ReO_3 , with an energy of -36 kJ/mol, whereby the aluminum becomes 5-coordinate. This finding was also supported by the results of EXAFS experiments. The broad ^{13}C NMR signal at 29 ppm, which is the only one observed at low CH_3ReO_3 loadings, is therefore assigned to the actual surface analog of this species. The Lewis acidity at aluminum depends strongly on the extent of distortion of the four-coordinate aluminum away from its preferred tetrahedral symmetry. Thus, when the siloxane is held at its final position, the

binding energy of CH_3ReO_3 increases to -199 kJ/mol. Since the extent of distortion from tetrahedral symmetry at the Al sites in amorphous silica-alumina is not known, and likely varies from site to site, the experimental binding energy of CH_3ReO_3 should be within this broad range, i.e., $-199 < \Delta E < -36$ kJ/mol.

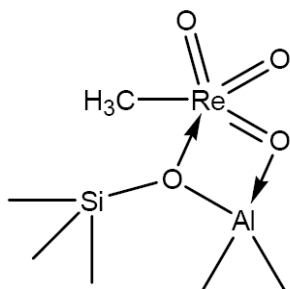


Figure 5-1. Energetically most favorable grafting site:
Two-point interaction of CH_3ReO_3 with the silica-alumina surface.

When the Re loading of this support is increased above 1 wt.% the catalytic activity of the system is not enhanced. NMR spectra in this range of Re loadings (1-10 wt.%) now show two families of chemically and spectroscopically distinct species: the more strongly-bound, active sites ($\delta(^{13}\text{C})$ 29 ppm, fwhm 460 Hz) as observed at low Re loadings (≤ 1 wt.%), but also highly mobile sites ($\delta(^{13}\text{C})$ 20 ppm, fwhm 95 Hz) which are attributed to CH_3ReO_3 molecules interacting with surface silanols. The latter are not catalytically active and are identified by DFT calculations and IR spectroscopy to bind by hydrogen-bonding of a Re oxo to the surface silanol. These H-bonded molecules also resist desorption from silica-alumina at room temperature; but are readily removed at 80°C . Their formation can be prevented by capping the surface hydroxyl groups with hexamethyldisilazane prior to grafting of CH_3ReO_3 . These conclusions were verified for CH_3ReO_3 on silica, which lacks Lewis acidity, by direct observation of the hydrogen-bonding interaction using ^1H MAS NMR. Olefin metathesis activity is thereby unambiguously correlated with the presence of Lewis acid

sites that activate CH_3ReO_3 , Figure 5-2. While the H-bonded CH_3ReO_3 molecules do not contribute to the metathesis activity, they are the likely cause of the severe leaching reported for $\text{CH}_3\text{ReO}_3/\text{SiO}_2\text{-Al}_2\text{O}_3$ metathesis catalysts prepared with high Re loadings.²² For the same reason that CH_3ReO_3 on silica is not active, other supports which possess mainly Brønsted acid sites as zeolite HY, or mesoporous aluminosilicates with very few Lewis acid centers also show little or no catalytic activity for propylene self metathesis. Thus models for CH_3ReO_3 activation based on proposed interactions with silica and, in particular, the surface silanols,¹⁷ or mechanisms without any organometallic-support interactions,²⁰⁹ cannot account for the observed reactivity.

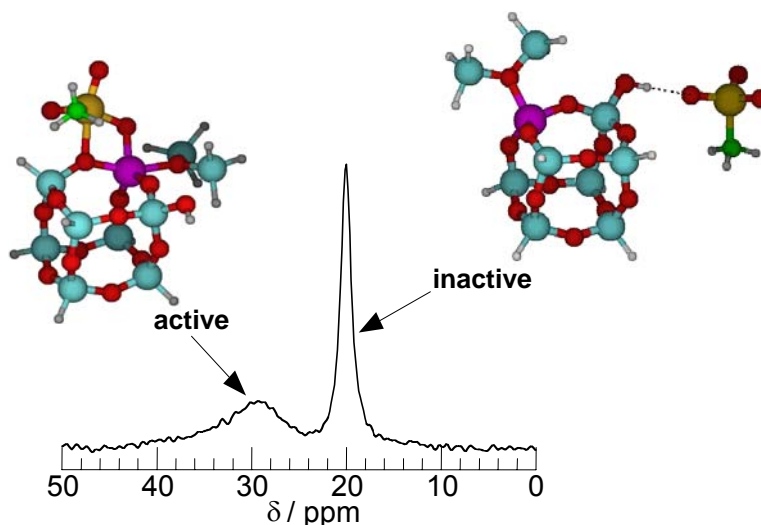


Figure 5-2. ^{13}C MAS NMR spectrum and computational models of CH_3ReO_3 grafted at high loading (10 wt.% Re) onto silica-alumina. The two distinct grafting sites exhibit very different olefin metathesis activities.

Following the identification of the structure of the active site and the mechanism for activation of CH_3ReO_3 by the amorphous silica-alumina support, the determination of the reaction conditions (dehydration of the support, low Re loading) that are necessary to produce uniform active sites, the next critical question to be addressed is that of how this Re-support interaction leads to

activity in olefin metathesis which is generally assumed to require the presence of a carbene ligand. Possible pathways of generating the initiating carbene ligand on the grafted CH_3ReO_3 are currently being explored using various experimental and computational approaches.

Extensive kinetic studies are underway to address the relatively low rate for metathesis activity as well as the selectivity of the metathesis reaction. These experiments use propylene homometathesis (propylene to ethylene and *cis/trans*-2-butene), Equation 5-1., as a convenient standard with which to compare different catalyst formulations.



Capping the surface hydroxyls with hexamethyldisilazane prior to adsorption of the catalyst was observed to leave the metathesis activity unaffected but to lead to an increase in the product selectivity. The capped catalyst also shows no deactivation in subsequent additions of propylene, whereas the uncapped catalyst deactivates strongly between additions of substrate, as does the heterogeneous $\text{Re}_2\text{O}_7/\text{Al}_2\text{O}_3$ system.

Additional multidimensional NMR studies as well as experiments at very high magnetic field strengths (e.g. 800 MHz) are being carried out in an attempt to observe directly nuclei with very large quadrupolar coupling constants such as $^{185}\text{Re}/^{187}\text{Re}$. Promising insights at high magnetic fields are also expected into distorted, penta-coordinated ^{27}Al sites in amorphous silica-alumina which evidently play a significant role to the activating ability of this support.

5.2 Semiconducting InGaP nanoparticles

Correlations between the structural aspects of InGaP nanoparticles and their photoluminescent properties were investigated by NMR methods and this work forms the second part of this thesis. Semiconductor nanoparticles find diverse applications in light-emitting devices²¹⁰ and as fluorescent biomarkers,²¹¹ because their optical and electrical properties depend in subtle and unique ways on particle sizes and compositions.²¹² Most applications have been based on colloidal Group II-VI semiconductor compounds, such as CdSe or CdS, which have been extensively studied.²¹³⁻²¹⁵ Group III-V semiconductors, such as InP, GaP, InN, or GaN, on the other hand, are less toxic, but have received less attention, in part because they have been available only in the form of large, polydisperse particles.^{61, 213} Advances in chemical synthesis protocols, however, have recently made it possible to prepare nanoscale Group III-V semiconductors and their ternary analogs (e.g., InGaP, InAlP) as monodisperse nanoparticles with discrete and tunable sizes.^{84, 88-90, 110, 216-220} The emission wavelengths of Group III-V compounds are dependent on their particle sizes and composition, while photoluminescent quantum efficiencies, on the other hand, are dependent on defect densities and vacancies at the surface of the nanoparticles. It is therefore essential for the utilization of these Group III-V quantum dots to elucidate the molecular and atomic level origins of the surface-dependent photoluminescent properties. These are at present largely unknown because of the difficulty of probing their internal structures, particularly near their surfaces.

The dramatic enhancements in photoluminescence quantum efficiencies are shown with the use solid state NMR methods to correspond directly to molecular

changes in nanoparticle surface structures following etching with HF. More specifically, large and correlated changes are observed in the local chemical and electronic environments of different nanoparticle components for lyothermally-grown, hexadecylamine-coated, nearly-monodisperse $\text{In}_{0.91}\text{Ga}_{0.09}\text{P}$ quantum dots, before and after HF etching. The combination of photoluminescence and solid state ^{31}P , ^{71}Ga and ^{115}In MAS NMR measurements establishes the heterogeneous distributions of different molecular In and Ga environments and their effects on the photoluminescent quantum efficiencies of these materials.

The 1D ^{31}P MAS NMR spectra are nearly identical for the unetched and etched nanoparticles and show ^{31}P signals at 24, 1, -9 and -210 ppm which correspond, respectively, to oxidized phosphorous sites (PO_3 and PO_4) located mostly on or near the surface and to interior, bulk-like ^{31}P sites (-210 ppm) in tetrahedral coordination. 2D ^{31}P MAS NMR measurements show that the PO_4 species are present on the surface, as well as within the quantum dot, while the PO_3 sites are primarily partial oxidation site on the surface.

The ^{115}In spectra of the InGaP nanoparticles show a broad distribution (centered at 780 ppm) of local ^{115}In environments both before and after etching, similar to that in bulk InP. A broad upfield shoulder stretching from 780 ppm to 0 ppm may be attributed to ^{115}In species in environments closer to the nanoparticle surfaces. The fact that these ^{115}In MAS spectra are barely influenced by the etching process further indicates that most ^{115}In species are sufficiently distant from the surface and thus unaffected by any surface modification.

The ^{71}Ga species, on the other hand, exhibit more significant changes in the molecular environments before and after HF treatment in the solid state ^{71}Ga

MAS NMR spectra. The spin-echo ^{71}Ga MAS spectrum of the unetched InGaP nanoparticles shows a signal (305 ppm) similar to that of bulk Ga, as well as a second peak (90 ppm; along with a shoulder at 65 ppm) assigned to Ga in the oxide layer near the surface. Dramatic changes in this spectrum are observed after HF-etching of the InGaP nanoparticles, and these are coincident with the development of strong photoluminescence properties. The same ^{71}Ga signals are present, but in different relative intensities: the upfield resonance assigned to ^{71}Ga in phosphonate-like environments at -65 ppm shows a substantial increase in relative intensity compared with the other MAS two signals. The linewidths of both main resonances in the HF etched InGaP nanoparticles have narrowed, which suggest a narrower distribution of local ^{71}Ga environments as a result of the etching process. These results are summarized in schematic form in Figure 5-3.

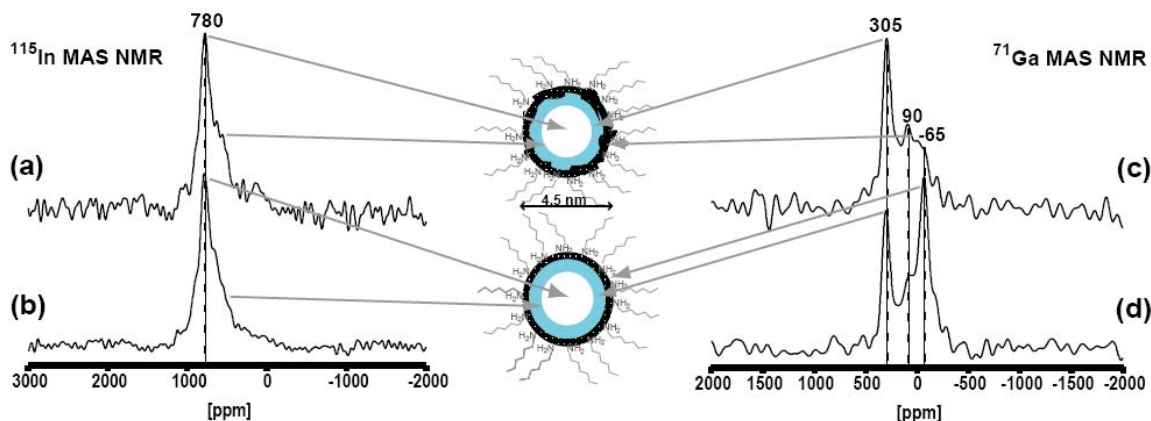


Figure 5-3. Structural changes upon HF-etching lead to enhanced photoluminescence in InGaP nanoparticles.

These series of measurements have provided a clear demonstration of the effects and importance of surface treatments on molecular-level composition, structures, and macroscopic optical properties of $\text{In}_{1-x}\text{Ga}_x\text{P}$ nanoparticles. Such results may be expected to be general for other semiconducting nanoparticle systems,

particularly those based on technologically important ternary Group III-V materials.

Ongoing efforts involve NMR measurements extended to systematic variations of these materials as well as into high magnetic field settings. These results in turn will guide the optimization of the semiconducting and optical properties of InGaP nanoparticles with respect to syntheses routes, particle sizes, particle compositions and choice of passivating ligands.

High-quality, nearly monodisperse nanoscale InGaP particles have since been prepared via direct microwave heating of the molecular precursors rather than convective heating of the solvent. Microwave dielectric heating not only enhances the rate of formation, but also improves the material quality and size distribution. InGaP particles are rapidly formed at 280 °C in minutes in clean reactions and yield monodisperse size distributions, which do not require size-selective precipitation and thereby result in the highest out-of-batch quantum efficiency reported to date at 15% prior to chemical etching. The use of microwave methodology is readily scalable to larger reaction volumes, has faster reaction times and removes the need for high temperature injection. These factors represent an important improvement of potential industrial significance in nanocrystal synthetic practice over current convective methods.

Chapter 6

References

- 1 Kungl. Vetenskapsakademien. The Royal Swedish Academy of Sciences. *Press Release: The Nobel Prize in Chemistry 2005*. **2005**.
- 2 Rouhi, A. M. *C&EN* **2002**, *80*, 29-33.
- 3 Mol, J. C. *Catal. Today* **1999**, *51*, 289-299.
- 4 Astruc, D. *New J. Chem.* **2005**, *29*, 42-59.
- 5 Schuster, M.; Blechert, S. *Chem. in unserer Zeit* **2001**, *35*, 24-29.
- 6 Hérisson, J.-L.; Chauvin, Y. *Makromol. Chem.* **1971**, *141*, 161-176.
- 7 Mol, J. C. *Green Chem.* **2002**, *4*, 5-13.
- 8 Fuerstner, A. *Angew. Chem. Int. Ed.* **2000**, *39*, 3012-3043.
- 9 Katz, T. J. *Angew. Chem. Int. Ed.* **2005**, *44*, 3010-3019.
- 10 Schwab, P.; Grubbs, R. H.; Ziller, J. W. *J. Am. Chem. Soc.* **1996**, *118*, 100-110.
- 11 Jafarpour, L.; Nolan, S. P. *J. Organomet. Chem.* **2001**, 617-618.
- 12 Basset, J. M.; Coperet, C.; Lefort, L.; Maunders, B. M.; Maury, O.; Roux, E. L.; Saggio, G.; Soignier, S.; Soulivong, D.; Sunley, G. J.; Taoufik, M.; Thivolle-Cazat, J. *J. Am. Chem. Soc.* **2005**, *127*, 8604-8605.
- 13 Ajjou, J. A. N.; Scott, S. L. *J. Am. Chem. Soc.* **2000**, *122*, 8968-8976.
- 14 Ivin, K. J.; Mol, J. C., *Olefin Metathesis and Metathesis Polymerization*; Academic: San Diego, 1997.
- 15 Kühn, F.; Scherbaum, A.; Herrmann, W. A. *J. Organomet. Chem.* **2004**, *689*, 4149-4164.
- 16 Morris, L. J.; Downs, A. J.; Greene, T. M.; McGrady, G. S.; Herrmann, W. A.; Sirsch, P.; Gropen, O.; Scherer, W. *Chem. Commun.* **2000**, 67-68.
- 17 Morris, L. J.; Downs, A. J.; Greene, T. M.; McGrady, G. S.; Herrmann, W. A.; Sirsch, P.; Scherer, W.; Gropen, O. *Organometallics* **2001**, *20*, 2344-2352.
- 18 Herrmann, W. A.; Kuchler, J. G.; Felixberger, J. K.; Herdtweck, E.; Wagner, W. *Angew. Chem. Int. Ed.* **1988**, *27*, 394-396.
- 19 Herrmann, W. A.; Wagner, W.; Flessner, U. N.; Volkhardt, U.; Komber, H. *Angew. Chem. Int. Ed.* **1991**, *30*, 1636-1638.
- 20 Bein, T.; Huber, C.; Moller, K.; Wu, C.-G.; Xu, L. *Chem. Mater.* **1997**, *9*, 2252-2254.
- 21 Buffon, R.; Auroux, A.; Lefebvre, F.; Leconte, M.; Choplin, A.; Basset, J. M.; Herrmann, W. A. *J. Mol. Catal.* **1992**, *76*, 287-295.
- 22 Rost, A. M. J.; Schneider, H.; Zoller, J. P.; Herrmann, W. A.; Kuehn, F. E. *J. Organomet. Chem.* **2005**, *690*, 4712-4718.
- 23 Zhang, C.; Guzei, I. A.; Espenson, J. A. *Organometallics* **2000**, *19*, 5257-5259.
- 24 Basset, J. M.; Buffon, R.; Choplin, A.; Leconte, M.; Tourode, R.; Herrmann, W. A. *J. Mol. Catal.* **1992**, *72*, L7-L10.
- 25 Nowak, I.; Ziolk, M. *Chem. Rev.* **1999**, *99*, 3603-3624.
- 26 Herrmann, W. A.; Watzlowik, P.; Kiprof, P. *Chem. Ber.* **1991**, *124*, 1101-1106.

- 27 Takacs, J.; Cook, M. R.; Kiprof, P.; Kuchler, J. G.; Herrmann, W. A. *Organometallics* **1991**, *10*, 316-320.
- 28 Takacs, J.; Kiprof, P.; Riede, J.; Herrmann, W. A. *Organometallics* **1990**, *9*, 782-787.
- 29 Mathew, T. M.; du Plessis, J. A. K.; Prinsloo, J. J. *J. Mol. Catal. A: Chem.* **1999**, *148*, 157-164.
- 30 Moses, A. W.; Leifeste, H. D.; Ramsahye, N.; Eckert, J.; Scott, S. L. *Catal. Org. React.* **2007**, *115*, 13-22.
- 31 Bell, A. T. *Science* **2003**, *299*, 1688-1691.
- 32 Gai, P. L.; Roper, R.; White, M. G. *Current Opinion in Solid State and Materials Science* **2002**, *6*, 401-406.
- 33 Schloegl, R.; Hamid, S. B. A. *Angew. Chem. Int. Ed.* **2004**, *43*, 1628-1637.
- 34 Bowen Katari, J. E.; Colvin, V. L.; Alivisatos, A. P. *J. Phys. Chem.* **1994**, *98*, 4109-4117.
- 35 Cordero, S. R.; Carson, P. J.; Estabrook, R. A.; Strouse, G. F.; Buratto, S. K. *J. Phys. Chem. B* **2000**, *104*, 12137-12142.
- 36 Dai, Y.; Han, S.; D., D.; Zhang, Y.; Qi, Y. *Solid State Commun.* **2003**, *126*, 103-106.
- 37 Ispasoiu, R. G.; Lee, J.; Papadimitrakopoulos, F.; Goodson, T. *Chem. Phys. Lett.* **2001**, *340*, 7-12.
- 38 Koberling, F.; Mews, A.; Basche, T. *Adv. Mater.* **2001**, *13*, 672-676.
- 39 Pellegrino, P.; Garrido, B.; Garcia, C.; Ferre, R.; Moreno, J. A.; Morante, J. R. *Physica E* **2003**, *16*, 424-428.
- 40 Tolbert, S. H.; Alivisatos, A. P. *Science* **1994**, *265*, 373-376.
- 41 Bhargava, R. N.; Chhabra, V.; Som, T.; Ekimov, A.; Taskar, N. *Phys. Stat. Sol. B* **2002**, *229*, 897-901.
- 42 De la Torre, J.; Souifi, A.; Lemiti, M.; Poncet, A.; Busseret, C.; Guillot, G.; Bremond, G.; Gonzalez, O.; Garrido, B.; Morante, J. R. *Physica E* **2003**, *17*, 604-606.
- 43 Irrera, A. P., D.; Miritello, M.; Franzo, G.; Priolo, F.; Iacona, F.; Sanfilippo, D.; Di Stefano, G.; Fallica, P. G. *Physica E* **2003**, *16*, 395-399.
- 44 Michalet, X.; Pinaud, F.; Lacoste, T. D.; Dahan, M.; Bruchez, M. P.; Alivisatos, A. P.; Weiss, S. *Single Mol.* **2001**, *2*, 261-276.
- 45 Milliron, D. J. A., A. P.; Pitois, C.; Edder, C.; Frechet, Jean, M. J. *Adv. Mater.* **2003**, *15*, 58-61.
- 46 Modreanu, M.; Gartner, M.; Aperathitis, E.; Tomozeiu, N.; Androulidaki, M.; Cristea, D.; Hurley, P.; Maltings, L. *Physica E* **2003**, *16*, 461-466.
- 47 Pacifici, D. I., A.; Franzo, G.; Miritello, M.; Iacona, F.; Priolo, F. *Physica E* **2003**, *16*, 331-340.

- 48 Tran, P. T.; Goldman, E. R.; Anderson, G. P.; Mauro, J. M.; Mattoussi, H. *Phys. Status Solidi B* **2002**, 229, 427-432.
- 49 Wang, D.; Rogach, A. L.; Caruso, F. *Nano Lett.* **2002**, 2, 857-861.
- 50 Yang, H. H., P. H.; Ratna, B. B. *J. Appl. Phys.* **2003**, 93, 586-592.
- 51 Becerra, L. R.; Murray, C. B.; Griffin, R. G.; Bawendi, M. G. *J. Chem. Phys.* **1994**, 100, 3297-3300.
- 52 Hostetler, M. J.; Wingate, J. E.; Zhong, C.-J.; Harris, J. E.; Vachet, R. W.; Clark, M. R.; Londono, J. D.; Green, S. J.; Stokes, J. J.; Wignall, G. D.; Glish, G. L.; Porter, M. D.; Evans, N. D.; Murray, R. W. *Langmuir* **1998**, 14, 17-30.
- 53 Luedtke, W. D.; Landman, U. *J. Phys Chem.* **1996**, 100, 13323-13329.
- 54 Meulenberg, R. W.; Bryan, S.; Yun, C. S.; Strouse, G. F. *J. Phys. Chem B* **2002**, 106, 7774-7780.
- 55 Meulenberg, R. W.; Strouse, G. F. *J. Phys. Chem. B* **2001**, 105, 7438-7445.
- 56 Sachleben, J. R.; Colvin, V.; Emsley, L.; Wooten, E. W.; Alivisatos, A. P. *J. Phys. Chem. B* **1998**, 102, 10117-10128.
- 57 Sachleben, J. R.; Wooten, E. W.; Emsley, L.; Pines, A.; Colvin, V.; Alivisatos, A. P. *Chem. Phys. Lett.* **1992**, 198, 431-436.
- 58 Aldana, J.; A., W. Y.; Peng, X. *J. Am. Chem. Soc.* **2001**, 123, 8844-8850.
- 59 Carter, A. C.; Bouldin, C. E.; Kenner, K. M.; Bell, M. I.; Woicik, J. C.; Majetich, S. A. *Phys. Rev. B* **1997**, 55, 13822-13828.
- 60 Micic, O. I.; Sprague, J.; Lu, Z.; Nozik, A. J. *Appl. Phys. Lett.* **1996**, 68, 3150-3152.
- 61 Adam, S.; McGinley, C.; Moeller, T.; Talapin, D. V.; Borchert, H.; Haase, M.; Weller, H. *Eur. Phys. J. D* **2003**, 24, 373-376.
- 62 Fu, H.; Zunger, A. *Phys. Rev. B* **1997**, 56, 1496-1508.
- 63 Langof, L.; Ehrenfreund, E.; Lifshitz, E.; Micic, O. I.; Nozik, A. J. *J. Phys. Chem. B.* **2002**, 106, 1606-1612.
- 64 Micic, O. I.; Nozik, A. J.; Lifshitz, E.; T., R.; Poluektov, O. G.; Thurnauer, M. C. *J. Phys. Chem. B.* **2002**, 106, 4390-4395.
- 65 Talapin, D. V.; Rogach, A. L.; Mekis, I.; Haubold, S.; Kornowski, A.; Haase, M.; Weller, H. *Colloids and Surfaces* **2002**, 202, 145-154.
- 66 Cheon, J.; Kang, N.; Lee, S.; Lee, J.; Yoon, J.; Oh, S. J. *J. Am. Chem. Soc.* **2004**, 126, 1950-1951.
- 67 Cumberland, S. L.; Berrettini, M. G.; Javier, A.; Strouse, G. F. *Chem. Mater.* **2003**, 15, 1047-1056.
- 68 Kubo, T.; Isobe, T.; Senna, M. *J. Lumin.* **2002**, 99, 39-45.
- 69 Pan, C.; Pelzer, K.; Philippot, K.; Chaudret, B.; Dassenoy, F.; Lecante, P.; Casanove, M. *J. Am. Chem. Soc.* **2001**, 123, 7584-7593.
- 70 Pokrant, S.; Whaley, K. B. *Eur. Phys. J. D* **1999**, 6, 255-267.
- 71 Chen, S. W.; Murray, R. W. *J. Phys. Chem. B* **1999**, 103, 9996-10000.

- 72 Harfenist, S.; Wang, Z. L.; Alvarez, M.; Vezmar, I.; Whetten, R. J. *Phys. Chem. B* **1996**, *100*, 13904-13910.
- 73 Polleux, J.; Pinna, N.; Antonietti, M.; Niederberger, M. *Adv. Mater.* **2004**, *16*, 436-439.
- 74 Warner, M. G.; Reed, S. M.; Hutchison, J. E. *Chem. Mater.* **2000**, *12*, 3316-3320.
- 75 Berrettini, M. G.; Braun, G.; Hu, J. G.; Strouse, G. F. *J. Am. Chem. Soc.* **2004**, *126*, 7063-7070.
- 76 Elbaum, R.; Vega, S.; Hodes, G. *Chem. Mater.* **2001**, *13*, 2272-2280.
- 77 Ladizhansky, V.; Hodes, G.; Vega, S. *J. Phys. Chem. B* **1998**, *102*, 8505-8509.
- 78 Ladizhansky, V.; Vega, S. *J. Phys. Chem. B* **2000**, *104*, 5237-5241.
- 79 Mayeri, D.; Phillips, B. L.; Augustine, M.; Kauzlarich, S. M. *Chem. Mater.* **2001**, *13*, 765-770.
- 80 Blackburn, J. L.; Ellingson, R.; Micic, O.; Nozik, A. J. *Phys. Chem. B* **2003**, *107*, 102-109.
- 81 Jang, E.; Jun, S.; Chung, Y.; Pu, L. *J. Phys. Chem. B* **2004**, *108*, 4597-4600.
- 82 Li, R.; Lee, J.; Yang, B.; Horspool, D.; Papadimitrakopoulos, F. *J. Am. Chem. Soc.* **2005**, *127*, 2524-2532.
- 83 Tomaselli, M.; Yarger, J. L.; Bruchez, M.; Havlin, R. H.; D., d.; Pines, A.; Alivisatos, A. P. *J. Chem. Phys.* **1999**, *110*, 8861-8864.
- 84 Battaglia, D.; Peng, X. *Nano. Lett.* **2002**, *2*, 1027-1030.
- 85 Borchert, H.; Haubold, S.; Haase, M.; Weller, H.; McGinley, C.; Riedler, M.; T., M. *Nano. Lett.* **2002**, *2*, 151-154.
- 86 Colvin, V. L. *Nature Biotech.* **2003**, *21*, 1166-1170.
- 87 Derfus, A. M.; Chan, W.; Bhatia, S. *Nano Lett.* **2004**, *4*, 11-18.
- 88 Gerbec, J. A.; Magana, D.; Washington, A.; Strouse, G. F. *J. Am. Chem. Soc.* **2005**, *127*, 15791-15800.
- 89 Guzelian, A. A.; Katari, J. E. B.; Kadavanich, A. V.; Banani, U.; Hmad, E.; Juban, E.; Alivisatos, A. P.; Wolters, R. H.; Arnold, C. C.; Heath, J. R. *J. Phys. Chem.* **1996**, *100*, 7212-7219.
- 90 Micic, O. I.; Sprague, J. R.; Curtis, C. J.; K.M., J.; Machol, J. L.; Nozik, A. J.; Giessen, H.; Fluegel, B.; Mohs, G.; Peyghambarian, N. *J. Phys. Chem.* **1995**, *99*, 7754-7759.
- 91 Talapin, D.; N., G.; Borchert, H.; L., R. A.; Haase, M.; Weller, H. *J. Phys. Chem. B* **2002**, *106*, 12659-12663.
- 92 Meulenberg, R. W.; Strouse, G. F. *Phys. Rev. B* **2002**, *66*, 035317-1-035317-6.
- 93 Puzder, A.; Williamson, A. J.; Gygi, F.; G., G. *Phys.Rev. Lett.* **2004**, *92*, 217401-1-217401-4.
- 94 Raola, O.; Strouse, G. F. *Nano Lett.* **2002**, *2*, 1443-1447.

- 95 Hamad, K. S.; Roth, R.; Rockenberger, J.; van Burren, T.; Alivisatos, A. P. *Phys. Rev. Lett.* **1999**, *83*, 3474-3477.
- 96 Page, K.; Proffen, T.; Terrones, H.; Terrones, M.; Lee, L.; Yang, Y.; Stemmer, S.; Seshadri, R.; Cheetham, A. K. *Chem. Phys. Lett.* **2004**, *393*, 385-388.
- 97 Wei, Z.; Sun, L.; Jiang, X.; Liao, C.; Yan, C.; Tao, Y.; Zhang, J.; Hu, T.; Xie, Y. *Chem. Mater.* **2003**, *15*, 3011-3017.
- 98 Zhang, J.; Wu, Z. Y.; Ibrahim, K.; Abbas, M. I.; Ju, X. *Nucl. Instrum. Methods Phys. Res., Sect. B* **2003**, *199*, 291-294.
- 99 Asami, H.; Abe, Y.; Ohtsu, T.; Kamiya, I.; Hara, M. *J. Phys. Chem. B* **2003**, *107*, 12566-12568.
- 100 Rodriguez-Lopez, J.; Montejano-Carrizales, J.; Pal, U.; Ramirez, J.; Troiani, H.; Garcia, D.; Miki-Yoshida, M.; Jose-Yacaman, M. *Phys. Rev. Lett.* **2004**, *92*, 196102-1-196102-4.
- 101 Mikulec, F. V.; Kuno, M.; Bennati, M.; Hall, D. A.; Griffin, R. G.; Bawendi, M. G. *J. Am. Chem. Soc.* **2000**, *122*, 2532-2540.
- 102 Chen, G.; Visbeck, S. B.; Hicks, R. F. *J. Appl. Phys.* **2002**, *19*, 9362-9367.
- 103 Goehring, L.; Michal, C. A. *J. Chem. Phys.* **2003**, *119*, 10325-10329.
- 104 Guivarch, A.; Haridon, L.; Pelous, G. *J. Appl. Phys.* **1984**, *55*, 1139-1148.
- 105 Hollinger, G.; Bergignat, E.; Robach, Y. *J. Vac. Sci. Technol. A* **1985**, *3*, 2082-2088.
- 106 Kikuchi, D.; Adachi, S. *Mat. Sci. Eng. B* **2000**, *76*, 133-138.
- 107 Simpson, W. C.; Yarmoff, J. A. *Annu. Rev. Phys. Chem.* **1996**, *47*, 527-554.
- 108 Thurgate, S. M.; Erickson, N. E. *J. Vac. Sci. Technol. A* **1990**, *8*, 3669-3675.
- 109 Wilmsen, C. W. *J. Vac. Sci. Technol. A* **1981**, *19*, 279-289.
- 110 Micic, O. I.; Sprague, J.; Lu, Z.; Nozik, A. J. *Appl. Phys. Lett.* **1996**, *68*, 3150-3152.
- 111 Laws, D. D.; Bitter, H.-M. L.; Jerschow, A. *Angew. Chem. Int. Ed.* **2002**, *41*, 3096-3129.
- 112 Harris, R. K.; Mann, B. E., *NMR and the Periodic Table*; Academic Press: London, 1978.
- 113 Jerschow, A. *Montash. Chem.* **2002**, *133*, 1481-1496.
- 114 Bovey, F. A.; Jelinski, L.; Mirau, P. A., *Nuclear Magnetic Resonance Spectroscopy*; Academic Press: California, 1988.
- 115 Brown, S. P.; Wimperis, S. *J. Magn. Reson.* **1997**, *124*, 279-285.
- 116 Brown, S. P.; Wimperis, S. *J. Magn. Reson.* **1997**, *128*, 42-61.
- 117 Goldbourt, A.; Madhu, P. K. *Montash. Chem.* **2002**, *133*, 1497-1534.
- 118 Vega, A. J. *Solid State Nucl. Mag.* **1992**, *1*, 17-32.
- 119 Kohn, W.; Sham, L. J. *Phys. Rev. B* **1965**, *140*, A1133-A1138.
- 120 Hohenberg, P.; Kohn, W. *Phys. Rev. B* **1964**, *136*, B864-B871.

- 121 Fay, M. J.; Proctor, A.; Hoffmann, D. P.; Hercules, D. M. *Analytical Chemistry* **1988**, *60*, 1225-1243.
- 122 Koeningsberger, D. C.; Prins, R., *X-ray Absorption*; Wiley: New York, **1988**.
- 123 Janicke, M. T.; Landry, C. C.; Christiansen, S. C.; Birtalan, S.; Stucky, G. D.; Chmelka, B. F. *Chem. Mater.* **1999**, *11*, 1342-1351.
- 124 Janicke, M. T.; Landry, C. C.; Christiansen, S. C.; Kumar, D.; Stucky, G. D.; Chmelka, B. F. *J. Am. Chem. Soc.* **1998**, *120*, 6940-6951.
- 125 Vinu, A.; Murugesan, V.; Boehlmann, W.; Hartmann, M. *J. Phys. Chem. B* **2004**, *108*, 11496-11505.
- 126 Hunger, M.; Freude, D.; Pfeifer, H. *Chem. Soc., Faraday Trans.* **1991**, *87*, 657-662.
- 127 Bronnimann, C. E.; Chuang, I. S.; Hawkins, B. L.; Maciel, G. E. *J. Am. Chem. Soc.* **1987**, *109*, 1562-1564.
- 128 Herrmann, W. A.; Kuehn, F. E.; Fischer, R. W.; Thiel, W. R.; Romao, C. C. *Inorg. Chem.* **1992**, *31*, 4431-4432.
- 129 Liu, C. C.; Maciel, G. E. *Anal. Chem.* **1996**, *68*, 1401-1407.
- 130 Massiot, D.; Fayon, F.; Capron, M.; King, I.; Calvé, S. L.; Alonso, B.; Durand, J.-O.; Bujoli, B.; Gan, Z.; Hoatson, G. *Mag. Res. Chem.* **2002**, *40*, 70-76.
- 131 Haase, J.; Freude, D.; Frölich, T.; Himpel, G.; Kerbe, F.; Lippmaa, E.; Pfeifer, H.; Sarv, P.; Schäfer, H.; Seiffert, B. *Chem. Phys. Lett.* **1989**, *156*, 328-332.
- 132 Frisch, M. J., et.al, *Gaussian 03, Revision C.02.*; Gaussian, Inc: Wallingford, CT, **2004**.
- 133 Pietsch, M. A.; Russo, T. V.; Murphy, R. B.; Martin, R. L.; Rappe, A. K. *Organometallics* **1998**, *17*, 2716-2719.
- 134 Nedelec, J. M.; Hench, L. L. *J. Non-Cryst. Solids* **2000**, *277*, 106-113.
- 135 Deguns, E. W.; Taha, Z.; Meitzner, G. D.; Scott, S. L. *J. Phys. Chem. B* **2005**, *109*, 5005-5011.
- 136 Meitzner, G. *Catal. Today* **1998**, *39*, 281-291.
- 137 Ressler, T. *J. Synchrotron Rad.* **1998**, *5*, 118-122.
- 138 Sayers, D. E.; Stern, E. A.; Lytle, F. W. *Phys. Rev. Lett.* **1971**, *27*, 1204-1207.
- 139 Ankudinov, A. L.; Bouldin, C.; Rehr, J. J.; Sims, J.; Hung, H. *Phys. Rev. B* **2002**, *65*, 104-107.
- 140 Hashain, S. S., *X-Ray Absorption Fine Structure*; Ellis Horwood: New York, 1991.
- 141 Rehr, J. J.; Albers, R. C. *Rev. Mod. Phys.* **2000**, *72*, 621-654.
- 142 Groot, F. d. *Chem. Rev.* **2001**, *101*, 1779-1808.
- 143 van Rossum, B. J.; Foerster, H.; de Groot, H. J. M. *J. Magn. Reson.* **1997**, *124*, 516-519.

- 144 Feike, M.; Graf, R.; Schnell, I.; Jäger, C.; Spiess, H. W. *J. Am. Chem. Soc.* **1996**, *118*, 9631-9634.
- 145 Herrmann, W. A.; Weichselbaumer, G.; Herdtweck, E. *J. Organomet. Chem.* **1989**, *372*, 371-389.
- 146 Malek, A.; Ozin, G. A. *Adv. Mater.* **1995**, *7*, 160-163.
- 147 Herrmann, W. A.; Kiprof, P.; Rypdal, K.; Tremmel, J.; Blom, R.; Alberto, R.; Behm, J.; Albach, R. W.; Bock, H.; Solouki, Mink, J.; Lichtenberger, D.; Gruhn, N. E. *J. Am. Chem. Soc.* **1991**, *113*, 6527-6537.
- 148 Dimakis, N.; Bunker, G. *Phys. Rev. B* **2002**, *65*, 201103.
- 149 Poiarkova, A. V.; Rehr, J. J. *Phys. Rev. B* **1999**, *59*, 948-957.
- 150 Herrmann, W. A.; Scherer, W.; Fischer, R. W.; Blümel, J.; Kleine, M.; Mertin, W.; Gruehn, R.; Mink, J.; Boysen, H.; Wilson, C. C.; Ibberson, R. M.; Bachmann, L.; Mattner, M. *J. Am. Chem. Soc.* **1995**, *117*, 3231-3243.
- 151 Mink, J.; Keresztury, G.; Stirling, A.; Herrmann, W. A. *Spectrochim. Acta A: Mol. Spec.* **1994**, *50*, 2039-2057.
- 152 Gun'ko, V. M.; Turov, V. V. *Langmuir* **1999**, *15*, 6405-6415.
- 153 Fleischer, U.; Kutzelnigg, W.; Bleiber, A.; Sauer, J. J. *J. Am. Chem. Soc.* **1993**, *115*, 7833-7838.
- 154 Hunger, M. *Solid State Nucl. Mag. Res.* **1996**, *6*, 1-29.
- 155 Schreiber, L. B.; Vaughan, R. W. *J. Catal.* **1975**, *40*, 226-235.
- 156 McManus, J.; Ashbrook, S. E.; MacKenzie, K. J. D.; Wimperis, S. J. *Non-Cryst. Solids* **2001**, *282*, 278-290.
- 157 Fyfe, C. A.; Bretherton, J. L.; Lam, L. Y. *J. Am. Chem. Soc.* **2001**, *123*, 5285-5291.
- 158 Bare, S. R.; Kelley, S. D.; Sinkler, W.; Low, J. J.; Modica, F. S.; Valencia, S.; Corma, A.; Nemeth, L. T. *J. Am. Chem. Soc.* **2005**, *127*, 12924-12932.
- 159 Moses, A. W.; Ramsahye, N. A.; Raab, C.; Leifeste, H. D.; Chattopadhyay, S.; Chmelka, B. F.; Eckert, J.; Scott, S. L. *Organometallics* **2006**, *25*, 2157-2165.
- 160 Herrmann, W. A.; Fischer, R. W. *J. Am. Chem. Soc.* **1995**, *117*, 3223-3230.
- 161 Ma, Q.; Klier, K.; Cheng, H.; Mitchell, J. W.; Hayes, K. S. *J. Phys. Chem. B* **2000**, *104*, 10618-10626.
- 162 Zhu, Z.; Espenson, J. H. *J. Mol. Cat. A: Chem.* **1997**, *121*, 139-143.
- 163 Tucker, M. G.; Keen, D. A.; Dove, M. T.; Trachenko, K. *J. Phys. Chem. Condens. Matter* **2005**, *17*, S67-S75.
- 164 Oldfield, E.; Haase, J.; Schmitt, K. D.; Schramm, S. E. *Zeolites* **1994**, *14*, 101-109.
- 165 McMillan, M.; Brinen, J. S.; Carruthers, J. D.; Haller, G. L. *Coll. Surf.* **1989**, *38*, 133-148.
- 166 Doremieux-Morin, C.; Martin, C.; Brégault, J.-M.; Fraissard, J. *Appl. Catal.* **1991**, *77*, 149-161.

- 167 Kato, Y.; Shimizu, K.; Matsushita, N.; Yoshida, T.; Satsuma, A.; Hattori, T. *Phys. Chem. Chem. Phys.* **2001**, *3*, 1925-1929.
- 168 Omegna, A.; Van Bokhoven, J. A.; Prins, R. *J. Phys. Chem. B* **2005**, *109*, 9280-9283.
- 169 Hunger, M.; Freude, D.; Pfeifer, H.; Bremer, H.; Jank, M.; Wendlandt, K.-P. *Chem. Phys. Lett.* **1983**, *100*, 29-33.
- 170 Omegna, A.; Van Bokhoven, J. A.; Prins, R. *J. Phys. Chem. B* **2003**, *107*, 8854-8860.
- 171 Van Bokhoven, J. A.; Van der Eerden, A. M. J.; Koningsberger, D. C. *J. Am. Chem. Soc.* **2003**, *125*, 7435-7442.
- 172 Schwartz, J. A. *J. Vac. Sci. Technol.* **1975**, *12*, 321-323.
- 173 Feher, F. J.; Budzichowski, T. A. *Polyhedron* **1995**, *14*, 3239-3253.
- 174 Civalleri, B.; Garrone, E.; Ugliengo, P. *Chem. Phys. Lett.* **1999**, *299*, 443-450.
- 175 Sauer, J.; Hill, J.-R. *Chem. Phys. Lett.* **1994**, *218*, 333-337.
- 176 Duchateau, R.; Harmsen, R. J.; Abbenhuis, H. C. L.; van Santen, R. A.; Meetsma, A.; Thiele, S. K.-H.; Kranenburg, M. *Chem. Eur. J.* **1999**, *5*, 3130-3135.
- 177 Feher, F. J.; Budzichowski, T. A.; Weller, K. J. *J. Am. Chem. Soc.* **1989**, *111*, 7288-7289.
- 178 Nabavizadeh, S. M. *Inorg. Chem.* **2003**, *42*, 4204-4208.
- 179 Nabavizadeh, S. M.; Akbari, A.; Rashidi, M. *Eur. J. Inorg. Chem.* **2005**, *12*, 2368-2375.
- 180 Wang, W.-D.; Espenson, J. H. *J. Am. Chem. Soc.* **1998**, *120*, 11335-11341.
- 181 Fischer, H. E.; King, S. A.; Bronnimann, C. E.; Schwartz, J. *Langmuir* **1993**, *9*, 391-393.
- 182 Pan, V. H.; Tao, T.; Zhou, J.-W.; Maciel, G. E. *J. Phys. Chem. B* **1999**, *103*, 6930-6943.
- 183 Scott, S. L.; Dufour, P.; Santini, C. C.; Basset, J.-M. *J. Chem. Soc., Chem. Commun.* **1994**, 2011-2012.
- 184 Scott, S. L.; Spakowicz, M.; Mills, A.; Santini, C. C. *J. Am. Chem. Soc.* **1998**, *120*, 1883-1890.
- 185 Crépeau, G.; Montouillet, V.; Vimont, A.; Mariey, L.; Cseri, T.; Maugé, F. *J. Phys. Chem. B* **2006**, *110*, 15172-15185.
- 186 Trombetta, M.; Busca, G.; Rossini, S.; Piccoli, V.; Cornaro, U.; Guercio, A.; Catani, R.; Willey, R. J. *J. Catal.* **1998**, *179*, 581-596.
- 187 Rosenthal, D. J.; White, M. G.; Park, G. D. *AIChE J.* **1987**, *33*, 336-340.
- 188 Hu, J.; Kwak, J. H.; Herrera, J. E.; Wang, Y.; Peden, C. H. F. *Solid State Nucl. Mag. Res.* **2005**, *27*, 200-205.
- 189 Grünberg, B.; Emmler, T.; Gedat, E.; Shenderovich, I.; Findenegg, G. H.; Limbach, H.-H.; Buntkowsky, G. *Chem. Eur. J.* **2004**, *10*, 5689-5696.

- 190 Pater, J. P. G.; Jacobs, P. A.; Martens, J. A. J. *Catal.* **1999**, *184*, 262-267.
- 191 Bouh, A. O.; Espenson, J. H. *J. Mol. Catal. A: Chem.* **2003**, *200*, 43-47.
- 192 Li, M.; Espenson, J. H. *J. Mol. Catal. A: Chem.* **2004**, *208*, 123-128.
- 193 Oikawa, T.; Masui, Y.; Tanaka, T.; Chujo, Y.; Onaka, M. *J. Organomet. Chem.* **2007**, *692*, 554-561.
- 194 Herrmann, W. A.; Wojtczak, W. A.; Artus, G. R. J.; Kuehn, F. E.; Mattner, M. R. *Inorg. Chem.* **1997**, *36*, 465-471.
- 195 Wang, W.; Buchholz, A.; Arnold, A.; Zu, M.; Hunger, M. *Chem. Phys. Lett.* **2003**, *370*, 88-93.
- 196 Leifeste, H. D. *Kinetic Studies of Metathesis Reactions Catalyzed by Supported Methyltrioxorhenium*; Master thesis, University of California, Santa Barbara, **2005**.
- 197 Clarke, P. G.; Gosling, K.; Harris, R. K.; Smith, E. G. *Zeolites* **1993**, *13*, 388-393.
- 198 Gora-Marek, K.; Derewinski, M.; Sarv, P.; Datka, J. *Catal. Today* **2005**, *101*, 131-138.
- 199 Sears, R. E. *Phys. Rev. B.* **1978**, *18*, 3054-3058.
- 200 Tomaselli, M.; deGraw, D.; Yarger, J. L.; Augustine, M. P.; Pines, A. *Phys. Rev. B.* **1998**, *58*, 8627-8633.
- 201 Thayer, A. M.; Steigerwald, M. L.; Duncan, T. M.; Douglass, D. C. **1988**, *60*, 2673-2676.
- 202 Mooney, R. C. L. *Acta Cryst.* **1956**, *9*, 113-17.
- 203 Bujoli-Doeuff, M.; Evain, M.; Fayon, F.; Alonso, B.; Massiot, D.; Bujoli, B. *Eur. J. Inorg. Chem.* **2000**, 2497-2499.
- 204 Kulshreshtha, S. K.; Jayakumar, O. D.; Sudarsan, V. J. *Phys. Chem. Sol.* **2004**, *65*, 1141-1146.
- 205 Klein Douwel, C. H.; Maas, W. E. J. R.; Veeman, W. S.; Werumeus Buning, G. H.; Vankan, J. M. J. *Macromolecules* **1990**, *23*, 406-412.
- 206 Mehring, M., *High-Resolution NMR Spectroscopy in Solids*; Springer-Verlag: New York, 1976.
- 207 Voelkel, R. *Angew. Chem. Int. Ed.* **1988**, *27*, 1468-1483.
- 208 Massiot, D.; Farnan, I.; Gautier, N.; Trumeau, D.; Trokiner, A.; Coutures, J. *P. Sol. St. Nucl. Mag. Reson.* **1995**, *4*, 241-248.
- 209 Zhang, X.; Narancic, S.; Chen, P. *Organometallics* **2005**, *24*, 3040-3042.
- 210 Colvin, V. L.; Schlamp, M. C.; Alivisatos, A. P. *Nature* **1994**, *370*, 354-357.
- 211 Bruchez, M.; Moronne, M.; Gin, P.; Weiss, S.; Alivisatos, A. P. *Science* **1998**, *281*, 2013-2016.
- 212 Murray, C. B.; Kagan, C. R.; Bawendi, M. G. *Ann. Rev. Mater. Sci.* **2000**, *30*, 545-610.

-
- 213 Grieve, K.; Mulvaney, P.; Grieser, F. *Curr. Opin. Coll. Interf. Sci.* **2000**, *5*, 168-172.
- 214 Gubin, S. P.; Kataeva, N. A.; Khomutov, G. B. *Russ. Chem. Bull.* **2005**, *54*, 827-852.
- 215 Ratcliffe, C. I.; Yu, K.; Ripmeester, J. A.; Zaman, M. B.; Badarau, C.; Singh, S. *Phys. Chem. Chem. Phys.* **2006**, *8*, 3510-3519.
- 216 Butler, L.; Redmond, G.; Fitzmaurice, D. J. *Phys. Chem.* **1993**, *97*, 10750-10755.
- 217 Dvorak, M. D.; Justus, B. L.; Gaskill, D. K.; Hendershot, D. G. *Appl. Phys. Lett.* **1995**, *66*, 804-806.
- 218 Mičić, O. I.; Nozik, A. J. *J. Luminescence* **1996**, *70*, 95-107.
- 219 Olshavsky, M. A.; Goldstein, A. N.; Alivisatos, A. P. *J. Am. Chem. Soc.* **1990**, *112*, 9438-9439.
- 220 Uchida, H.; Curtis, C. J.; Kamat, P. V.; Jones, K.; Nozik, A. J. *J. Phys. Chem.* **1992**, *96*, 1156-1160.

Appendix

Curriculum Vitæ

CHRISTINA RAAB

Email: christina.raab@gmail.com

Date of birth: March 12th, 1979

Education and training

- 04/2003- 06/2007
AUSTRIA **VIENNA UNIVERSITY OF TECHNOLOGY**
Doctoral studies at the Institute of Materials Chemistry;
Advisor: Prof. Dr. Ulrich Schubert, Prof. Dr. Nicola Hüsing
- 04/2003 - 05/2006
U.S.A. **UNIVERSITY OF CALIFORNIA, SANTA BARBARA**
Doctoral research; visiting scholar at the Department of
Chemical Engineering; Advisor: Prof. Dr. Bradley Chmelka
- 10/1997 - 03/2003
AUSTRIA **VIENNA UNIVERSITY OF TECHNOLOGY**
Diploma in Chemistry/Chemical Engineering, *with distinction*
Major: Inorganic Chemistry, Materials Chemistry
Diploma thesis: "A novel ethylene glycol based silica
precursor in the synthesis of mesostructured silica monoliths"
- 04/2002 - 03/2003
AUSTRIA **VIENNA UNIVERSITY OF TECHNOLOGY**
Teaching assistant, inorganic chemistry laboratory
- 07/2002
SPAIN **INSTITUT DE CIÈNCIA DE MATERIALS DE BARCELONA**
Research for diploma thesis
- 09/2000 - 02/2001
FRANCE **ECOLE DE CHIMIE, POLYMÈRES, MATÉRIAUX DE STRASBOURG**
Erasmus exchange program
- 09/1989 - 06/1997
AUSTRIA **BRG LERCHENFELDSTRASSE KLAGENFURT**
High school diploma, *with distinction*

Publications and presentations related to this thesis

C. Raab, A. W. Moses, R. C. Nelson, H. D. Leifeste, N. A. Ramsahye, S. Chattopadhyay, J. Eckert, B. F. Chmelka, S. L. Scott, "Spectroscopically Distinct Sites Present in Methyltrioxorhenium Grafted onto Silica-Alumina, and their Abilities to Initiate Olefin Metathesis", *J. Am. Chem. Soc.* **2007**, submitted.

M. G. Berrettini, C. Raab, J. D. Epping, J. Gerbec, G. F. Strouse, B. F. Chmelka, "Enhanced Optical Properties of Surface-Modified Monodisperse InGaP Nanoparticles", *J. Am. Chem. Soc.* **2007**, submitted.

A. W. Moses, N. A. Ramsahye, C. Raab, H. D. Leifeste, S. Chattopadhyay, B. F. Chmelka, J. Eckert, S. L. Scott, "Methyltrioxorhenium Interactions with Lewis Acid Sites of an Amorphous Silica-Alumina", *Organometallics* **2006**, *25*, 2157-2165.

C. Raab, A. W. Moses, N. A. Ramsahye, S. Chattopadhyay, H. D. Leifeste, J. Eckert, S. L. Scott, B. F. Chmelka, "Site-Specific Characterization of CH₃ReO₃ on Silica-Alumina for Olefin Metathesis", 4th Annual University of California Symposium on Surface Science and Its Applications, Berkeley, CA, USA, **2006**.

M. Berrettini, C. Raab, J. A. Gerbec, B. F. Chmelka, G. F. Strouse, "Structural Characterization of InGaP Nanocrystals by Solid State NMR Techniques", Abstract of Papers, 228th ACS National Meeting, Philadelphia, PA, USA, **2004**.